2018

Ice versus Liquid Water Saturation in Regional Climate Simulations of the Indian Summer Monsoon

Russell Henderson Glazer

FLORIDA STATE UNIVERSITY

COLLEGE OF ARTS AND SCIENCES

ICE VERSUS LIQUID WATER SATURATION IN REGIONAL CLIMATE SIMULATIONS OF THE INDIAN SUMMER MONSOON

By

RUSSELL HENDERSON GLAZER

A Dissertation submitted to the
Department of Earth, Ocean and Atmospheric Science
in partial fulfillment of the
requirements for the degree of
Doctor of Philosophy

2018

Russell Henderson Glazer defended this dissertation on April 9, 2018.
The members of the supervisory committee were:

Vasubandhu Misra
Professor Directing Dissertation

Sachin Shanbhag
University Representative

Mark Bourassa
Committee Member

Robert Hart
Committee Member

Guosheng Liu
Committee Member

The Graduate School has verified and approved the above-named committee members, and certifies that the dissertation has been approved in accordance with university requirements.

ACKNOWLEDGMENTS

First and foremost I would like to recognize my parents and family for their support and advice throughout the last three years. Their contributions at crucial moments through advice and support were invaluable to making these past years a success. Next I would like to recognize friends and colleagues, in and outside the program, at or not at COAPS who have lent their assistance, adivce and technical experience over the years and have contributed to the success of this work as well as the development of myself as a scientist. Without the interactions and friendships that were developed over the years this process would clearly not have gone as smoothly or as successfully. I would also like to recognize COAPS, and the EOAS department at FSU who made this opportunity possible in the first place. I would especially like to thank the COAPS organization in this regard for offering me my first research position and for providing an amazing amount of resources and access to experiences like conference presentations which have been important to my growth as a scientist and as an individual. I would like to gratefully acknowledge my PhD adviser Dr. Vasubandhu Misra first for the opportunity offered to me three years ago to continue my graduate study and make this possible but also for his support, scientific discussion, and advise which he always made available. In addition I would like to thank the members of my PhD committee who have volunteered their time to contribute to this work: Dr. Robert Hart, Dr. Mark Bourassa, Dr. Guosheng Liu, and Dr. Sachin Shanbhag. I would also gratefully acknowledge the financial support given by the Earth System Science Organization, Ministry of Earth Sciences, Government of India (Grant number MM/SERP/FSU/2014/SSC-02/002) to conduct this research under Monsoon Mission. I thank the Indian Meteorological Department for the availability of the daily rain analysis over India. Computing resources were provided by the Texas Advanced Computing Center at the University of Texas and XSEDE under grant number ATM10010 and Florida State University's High Performance Computer. I would also like to acknowledge Dr. Akhilesh Mishra at FSU COAPS for his advice and assistance in this work.

TABLE OF CONTENTS

LIST OF TABLES

LIST OF FIGURES

ABSTRACT

At the same temperature, below 0^{o}C, the saturation vapor pressure (SVP) over ice is slightly less than the SVP over liquid water. Numerical models use the Clausius-Clapeyron relation to calculate the SVP and relative humidity, but there is not a consistent method for the treatment of saturation above the freezing level where ice and mixed-phase clouds may be present. In the context of current challenges presented by cloud microphysics in climate models, we argue that a better understanding of the impact that this treatment has on saturation-related processes like cloud formation and precipitation, is needed. This study explores the importance of the SVP calculation through model simulations of the Indian Summer Monsoon (ISM) using atmosphere-only simulations with the Regional Spectral Model (RSM) and RSM coupled to the Regional Ocean Modeling System (RSM-ROMS). Atmosphere-only simulations are conducted with two saturation parameterizations. In one, the SVP over liquid water is prescribed through the entire atmospheric column (woIce), and in another the SVP over ice is used above the freezing level (wIce). When SVP over ice is prescribed, a thermodynamic drying of the middle and upper troposphere above the freezing level occurs due to increased condensation. In the wIce runs, the model responds to the slight decrease in the saturation condition by increasing, relative to the SVP over liquid water only run, grid-scale condensation of water. Changes in the cloud layer amounts in the wIce simulation cause in increase in the net heat flux (NHF) at the surface of 2-3 W/m^2 over the Arabian Sea (AS) and a decrease of similar magnitude over the eastern equatorial Indian Ocean (EEIO). Motivated by these NHF changes the wIce and woIce experiments were repeated in the coupled simulations. With coupling added, the ocean is allowed to respond to any NHF changes; however we find that the NHF difference between wIce-woIce over the AS is near zero. It is proposed that with the inclusion of air-sea coupling the

atmospheric and oceanic response to changes in the SVP is damped relative to the forced RSM integrations.

The importance of air-sea interaction for the northward propagation and evolution of the Indian monsoon intraseasonal oscillation (ISO) is examined through a comparison between the uncoupled and coupled simulations, and the observed ISO. It was found that the observed ISO contains a robust air-sea interaction during its evolution which would suggest that coupling is required to simulate the observed relationship between the ocean and atmosphere during the ISO. However, the uncoupled simulations show the ability to simulate realistic amplitude ISOs without coupling to the ocean, suggesting that there is an internal atmospheric component that is important for simulating the observed ISO period and amplitude.

CHAPTER 1

INTRODUCTION

1.1 The Saturation Vapor Pressure in Numerical Models and Observations

In numerical models, the calculation of saturation vapor pressure (SVP) in the atmosphere is most typically done through iterations of the Clausius-Clapeyron equation with the input of the local temperature. This is then used to calculate other moisture variables, such as the relative humidity, which are used throughout the model for the specified time step. The SVP calculation is essential because cloud formation is observed at relative humidities at or very close to saturation (Rogers and Yau 1989). Below the freezing point (0^{o}C), formation of ice is possible and saturation over ice occurs at a slightly lower vapor pressure than over water. This means that cloud formation will differ depending on whether ice or water is present. However, above the freezing level, clouds are often mixed-phase depending on whether or not ice nuclei are present. Because of the necessity for ice to form a lattice shape, only a subset of atmospheric aerosols can serve as a surface for ice formation. Thus, ice nuclei are much less common in the atmosphere compared to condensation nuclei with typical concentrations ranging from 10^{-4} cm^{-3} to 10^{-1} cm^{-3} compared to 100 cm^{-3} for condensation nuclei (Murray et al. 2012). This leads to the observation that it is quite common to find supercooled water drops above the freezing level up to nearly -40^{o}C.

The general convention for radiosonde observations is to report the relative humidity with respect to liquid water throughout the atmospheric column (WMO 1988; 2015a). In a recent World Meteorological Organization (WMO) report (WMO 2015b), it was acknowledged that national practices often differ in the method used to calculate dewpoint and frost point. Observational and theoretical studies of relative humidity by Korolev and Isaac (2006) and

Korolev and Mazin (2003) concluded that in mixed-phase clouds the relative humidity is close to the saturation over water, whereas in ice-phase clouds the relative humidity can be lower than the saturation over ice or supersaturated over ice but is always lower than the saturation over water. A review study by Murphy and Koop (2005) recommended reporting the relative humidity with respect to ice below 0^{o}C because of the uncertainty in measurements of the vapor pressure of supercooled water. Considering these studies and recommendations, it is apparent that a consistent method for calculating moisture and humidity variables does not yet exist.

Because a substantial portion of the troposphere holds temperatures below the freezing point, the potential impact on a numerical model due to the treatment of saturation in this region should not be ignored. The assumptions made about saturation in the freezing region will affect the water vapor distribution, the cloud amount, the precipitation, and the radiative flux through the atmosphere, regardless of whether the cloud scheme is prognostic or diagnostic. Currently, there is not a consistent treatment of ice and liquid-phase moisture variables in numerical models. Some have specified saturation over water for mixed-phase clouds (e.g., Rotstyan et al. 2000; Tremblay and Glazer 2000) , but most use separate temperature conditions to divide the regions where liquid, mixed and ice phase clouds are assumed to form (e.g., Fowler et al. 1996; Moorthi et al. 2001; Slingo 1980; Lohmann and Roeckner 1996). Table 1 compiles a list of the saturation conditions used in five Coupled Model Intercomparison Project Phase 5 (CMIP5) models. Note that the way moisture variables (e.g. relative humidity) are represented in model output may not reflect how they are treated internally within the model. Table 1 is meant to reflect how the moisture and saturation is treated internally, as it relates to cloud formation for each model. Several models including the National Center for Environmental Prediction (NCEP) Climate Forecast System version 2 (CFSv2), the Geophysical Fluid Dynamics Laboratory

(GFDL) AM3, and the National Center for Atmospheric Research (NCAR) CCSM4 treat the region between 0^{o}C and -20^{o}C as the mixed phase region, and linearly interpolate the SVP from saturation over liquid at 0^{o}C, to saturation over ice at -20^{o}C. The NASA GISS ModelE calculates the saturation over water for all layers below -4^{o}C over the ocean and -10^{o}C over land, and all layers above -35^{o}C are saturation over ice. In between a probability exists for either phase but not both (either liquid or ice but not mixed). The reasoning for each temperature condition is tied directly to what cloud phase is assumed to be formed at those temperatures. Note that large differences exist in the assumptions made between the group of models which designate 0^{o}C to -20^{o}C for mixed saturation, and the NASA and Max Planck Institute (MPI) models (see Table 1). While numerous formulations exist to address the basic principle of saturation, relatively little attention has been paid to the potential sensitivity that the treatment of saturation has within a numerical model.

1.2 The Cloud-Radiative Feedback and the Importance of Microphysics

On the other hand, the role that clouds play in climate has received an enormous amount of attention since the satellite era began. Relative to a cloud-free Earth-atmosphere, clouds cool the mean global climate by increasing Earth's albedo and reflecting incoming solar radiation back to space, and warm the mean global climate by absorbing and trapping longwave radiation emitted from Earth (Ramanathan 1987). Ramanathan et al. (1989) demonstrated that in our current climate, albedo and solar effects are larger than the heat trapping longwave effects, thus clouds have a net cooling effect on the global climate. How these effects change with a warmer climate is referred to as the "cloud radiation feedback." Many authors have identified the cloud radiation feedback as one of the most important remaining questions in understanding and

modeling future climate change (Dessler 2010; Stephens 2005; Bony et al. 2015; Randall et al. 2007). Additionally, the relative composition of hydrometeors and liquid versus ice content within clouds has a strong impact on radiative fluxes through the atmosphere (Matus and L'Ecuyer 2017). The representation of cloud ice and its thermodynamic and radiative properties in climate models could be a cause for remaining uncertainties in modeling future climate change (Waliser et al. 2009, 2011; Su et al. 2011). A recent study by Tan et al. (2016) reported a major source of uncertainty in CMIP5 climate projections that is attributed to inaccuracies in the production of ice in mixed-phase clouds from the CMIP5 model schemes. A major source of ice crystal growth within mixed-phase clouds is the Wegener-Bergeron-Findeisen (WBF) process (Pruppacher and Klett 1978) whereby ice grows at the expense of liquid water in a mixed phase cloud. SVP between that over ice and that over liquid water is a necessary but not sufficient condition for ice crystal growth by WBF in mixed-phase clouds.

1.3 The Indian Summer Monsoon

The Indian summer monsoon (ISM) is one of the dominant yearly tropical circulations and has far-ranging teleconnections to regions from the equatorial east Pacific to east Africa and the Arabian Deserts (Webster et al. 1998). The ISM provides upwards of 80% of the annual rainfall for the Indian subcontinent and thus India’s agricultural and economic well-being are closely tied to the ISM (Parthasarathy et al. 1994). With nearly a quarter of the world’s population living within this monsoon region, the importance of studying the ISM cannot be overstated, especially in light of longstanding difficulties with modeling the ISM (Waliser et al. 2003; Sperber et al. 2012; Sabeerali et al. 2014). However, significant progress has been made recently to improve the resolution and parameterization of clouds and their microphysics in the

CFSv2 (Abhik et al. 2017; Ramu et al. 2016; Goswami et al. 2015), which is currently used operationally at the India Meteorological Department (IMD) for seasonal ISM forecasting. As a result of improvements to the cloud representation in the CFS, Abhik et al. (2017) and Goswami et al. (2015) found improved propagation of the ISM intraseasonal oscillation and its associated rainfall signature. In addition, several recent studies have documented the importance of the ISM's cloud characteristics for understanding the observed rainfall patterns (Kumar et al. 2014) and the propagation (Jiang et al. 2011; Abhik et al. 2013; Wang et al. 2015) and identification of intraseasonal oscillations (Rajeevan et al. 2013). In a study related to the present one, Hazra et al. (2017) conducted two global simulations with a focus on the Indian summer monsoon using the CFSv2. One simulation included both warm and cold rain microphysical production processes and the other was run without cold rain processes, essentially testing the impact that ice microphysical processes have on global tropical circulations through the vertical distribution of latent heating, radiative heating, and the production of grid-scale rainfall. The study found that the inclusion of ice microphysical processes which produce rainfall leads to an increase in upper troposphere latent heating and cloud amount, and leads to an overall increase in grid-scale rainfall.

1.3.1 ISM Precipitation and Cloud Characteristics

The seasonal mean precipitation and cloud characteristics of the ISM feature high spatio-temporal complexity. In time, relatively high frequency intraseasonal oscillations (ISO) dominate the variability observed on the weekly to monthly timescale, while forcing on an interannual and multiyear timescale can originate from multiple external sources such as El Nino Southern Oscillation (Webster et al. 1998), interannual SST variability in the Indian Ocean (Ashok et al.

2001; Saji et al. 1999), and Eurasian snow pack and soil moisture (Hahn and Shukla 1976). Spatially, two local maxima appear in the seasonal mean rainfall over land: one over the western coast of India along the high terrain of the Western Ghats, and the other along the western coast of Myanmar (Romatschke and Houze 2011, Kumar et al. 2014). The seasonal mean rainfall in these two regions is similar. However, Kumar et al. (2014) found that these regions differ in the variability of rainfall and this owes to the different cloud types and cloud microphysical properties in each region. A schematic of the differing cloud types and characteristics of these two regions is provided in Fig. 1 (following Kumar et al. 2014). Over the Western Ghats, cloud liquid water content is plentiful at low levels, while ice water content is generally sparse in the upper troposphere. This contributes to the development of generally shallower convection with a shallower diabatic latent heating profile. However, Kumar et al. (2014) finds that this region receives much of its rainfall from heavy precipitation. The production of heavy convective rainfall is aided by the addition of sea salt condensation nuclei which can be transported from the Arabian Sea by the low-level monsoon flow. Over the Myanmar Coast clouds contain plentiful amounts of both liquid water and ice content in the vertical indicating deeper convective clouds. These deep convective clouds contain a greater mixture of hydrometeors and associated mixed phase processes allow for a more diverse rainfall distribution. The rainfall characteristics of the Myanmar Coast are thus defined by steadier stratiform type rainfall in addition to heavy convective rain, in contrast to the rainfall distribution over the Western Ghats. Deep convective clouds with cold cloud tops over a large area is also an explanation for why a minimum in outgoing longwave radiation (OLR) is observed in the seasonal mean over the Myanmar Coast (Kumar et al. 2014). Considering the diversity of clouds types and microphysics as well as

complex terrain interaction in the region, it is clear that forecasting and climate projection of the ISM from a modeling prospective would be a challenge.

1.3.2 External Vs. Internal Variability

The interannual variability of ISM mean rainfall can generally be described by two components. One component is an externally 'forced' variability from sources like El Nino Southern Oscillation (ENSO; Rasmusson and Carpenter 1983; Webster et al. 1998), Indian Ocean Dipole (IOD; Ashok et al. 2001; Saji et al. 1999), and Himalayan mountain snow pack (Hahn and Shukla 1976). These external forcings can be forecast and observed sometimes several months ahead of time and thus their forcing on the ISM has a relatively higher predictability. The other component is a more unpredictable internal variability that has its origins in the active and break periods of the monsoon ISO. The internally forced variability is a result of highly unpredictable mesoscale and synoptic scale convective feedbacks originating in the Indian Ocean ITCZ. Goswami (1998) and Goswami et al. (2006) proposed that the ISM region may have a uniquely low intrinsic predictability compared to other monsoon regions due to a high amount internal variability which accounts for a substantial portion of the seasonal mean rainfall. In fact, Goswami and Ajaya Mohan (2001) concluded that this internal contribution to the interannual variability can be large as the externally forced component.

1.3.3 Intraseasonal Oscillations and the Role of Air-sea Interaction

The Indian monsoon intraseasonal oscillation (ISO) is defined as the northward propagating mode of precipitation and convection variability observed on timescales of 10-90 days during the June-Sept. ISM season (Krishnamurthy and Shukla 2000). The 10- to 90-day

variability can be separated further into two main modes of intraseasonal variability, a 30-60 day oscillation and a weaker quasi-biweekly 10-20 day oscillation (Krishnamurty and Shukla 2007). Observations of the ISO were first noted in satellite derived cloudiness by Yasunari (1979,1980) and by Krishnamurty and Subrahmayam (1982) using wind observations. Because of its integral importance for Indian monsoon rainfall variability on both interannual and intrasesaonal timescales, the ISO it has been the subject of numerous scientific studies on its origins, how it propagates, and predicting its occurrence using atmospheric and coupled ocean models. The ISO has its origins in eastward propagating Rossby-Kelvin wave packets associated with Madden-Julian Oscillations (MJOs) that travel along the equator from East Africa into the Indian Ocean (Wang and Xie 1997; Lawrence and Webster 2002; Schott et al. 2009). Lawrence and Webster (2002) describe the summer monsoon ISO events as having both an eastward propagating component, associated with the equatorial wave and a northward propagating component associated with the interaction with summer monsoon background state. In response to the heating generated by the eastward moving convective center, cyclonic circulations to the north and south of the equator form in the central and eastern Indian Ocean (IO) similar to the Gill-type atmospheric response to isolated heating on the equator (Rui and Wang 1990; see Fig. 1). Both the northern and the southern cyclonic circulation propagate poleward, but the northward component is much stronger.

There have been numerous studies which have attempted to explain the northward propagation of the ISO. Webster (1983) and Srinivasan et al. (1993) suggested that land surface heat flux interaction with the PBL resulted in destabilization of the PBL to the north of the convection center which would propagate it north. Rowell (1997) hypothesized that dry spells can be induced by the advection of dry, high negative potential vorticity air from the southern

hemisphere. In past studies there have been two general groups of theories that explain the northward propagation of ISOs. In one group, the occurrence of northward propagating ISOs in the IO is explained as a result of "internal" atmospheric dynamics (Wang and Xie 1997; Jiang et al. 2004). If northward propagating ISOs were indeed a result of the mean atmospheric state in the IO during boreal summer, then one would expect that an atmosphere only model with prescribed sea surface temperature (SST) would have the ability to fully simulate the observed northward propagation. Waliser et al. (2003) investigated the predictability of the ISO using atmosphere only and prescribed SST simulations. The model used by Waliser et al. (2003) was able to reproduce the observed northward propagation and phase speed, suggesting that the ISO may indeed be the result of internal atmospheric dynamics.

However, a second group of studies regard the northward propagation of summer ISOs as the result of interaction between air-sea interface. These studies postulate that the atmospheric convection associated with the ISO interacts with the ocean through modulation of the solar heat flux and latent heat flux in what is called the Wind-Evaporation-SST (WES) feedback (Kemball-Cook and Wang 2001; Vecchi and Harrison 2002; Fu et al. 2003; Rajendran and Kitoh 2006; Seo et al. 2007; Schott et al. 2009; Li et al. 2017). There is some consensus that air-sea interaction in the IO plays a pivotal role in the northward propagation, but to what degree is still under debate.

The WES feedback involves the following processes: an anomalous cyclonic circulation associated with convection from an eastward propagating MJO is located to the north (and south) of the equator (Fig. 1). To the north of the equator this cyclonic circulation produces anomalous easterly winds superimposed upon the mean westerlies during the monsoon. The total wind is then weakened resulting in a decrease in overall latent heat flux to the north of the convection. Near and to the north of the convection center however, anomalous westerlies increase the mean

monsoon circulation and result in increased evaporation and latent heat flux. At the same time, the downward solar flux is increased to the north of the convection due to decreased cloudiness. The combined contribution from the latent and solar heat flux result in a warming of the SST to the north of the convection, and a cooling of the SSTs near the convection center. The warming of the SSTs to the north of the convection along with the anomalous increase in latent heat fluxes near and to the north of the convection center allows for the perpetual destabilization of the boundary layer north of the convection. In this way, convection associated with MJOs along the equator can result in northward propagation in the presence of the ISM mean westerlies.

Of particular importance to the northward propagation of the ISO and the WES feedback is the apparent sensitivity of the upper ocean in the Bay of Bengal (BoB). Several studies have noted large intraseasonal SST variability in BoB associated with the ISO from satellite and bouy observations on the order of 2-3 ^{o}C from peak-to-trough (Premkumar et al. 2000; Sengupta et al. 2001; Sengupta and Ravichandran 2001). The processes which control the upper ocean temperature and stratification in the BoB are complex. A large year-round freshwater flux is present in the BoB due to river runoff and precipitation during the ISM season. This can create a thick barrier layer which can limit depth of the mixed layer even in the presence of a deep thermocline. When the mixed layer is shallow, the SST is more sensitive to changes in the net surface heat flux from the atmosphere. During the ISM substantial changes in the solar and latent heat flux occur on intraseasonal timescales associated with ISO (Schiller and Godfrey 2003). Recent studies by Li et al. (2017) and Girishkumar et al. (2017) have linked the depth of the barrier layer and mixed layer to the sensitivity of BoB SSTs during ISO events. In essence, the WES feedback is amplified in the BoB because of unique upper ocean conditions present during the ISM. This may further shed light on why the northward propagation in the IO is so strong

during the ISM compared with, for instance, the IO winter monsoon or the summer ISOs which occur in the West Pacific and South China Sea.

1.3.4 Cloud Characteristics Associated with ISO Propagation

In analyzing the mechanisms that control the propagation of the ISO, some studies have identified northward tilted cloud structures which enhance moisture advection and dynamical convergence leading to destabilization ahead of the cloud cluster (Jiang et al. 2011; Abhik et al. 2013; Wang et al 2015; Rajeevan et al 2013). Abhik et al. (2013) proposed that the composition of ice and mixed-phase hydrometeors within the deep convective clouds that characterize ISO contribute to the maintenance of the ISO by enhancing upper-level divergence and lower-level convergence within convective cloud clusters. To the north of these cloud clusters, moisture advection at low levels is enhanced and this allows convective instability to develop and facilitate formation of new convection to the north. In this way, the convective clusters propagate northwards into central India until this moisture advection and instability feedback is reduced by the arid Himalayan highlands in northern India. Active and break periods of the ISO can be clearly detected in retrievals of cloud water and ice content (Rajeevan et al. 2013). In the BoB during active phases, cloud ice can increase by nearly 200% in association with a large amount of deep convection (Rajeevan et al. 2013). Wang et al. (2015) noted transitions between cloud regimes that accompanied shifts from active to break periods of the ISO. Active periods characterized by deep convection and cirrostratus, transition to shallow cumulus, marking the beginning of the break phase. This concept of transition periods between active and break phases or phases of "recharge" and "discharge" is very closely related to air-sea interaction theories for the ISO's northward propagation.

1.4 Indian Ocean Net Heat Flux-SST Relationship

1.4.1 Interannual and Intraseasonal Net Heat Flux Variability

The Indian Ocean (IO) is unique in comparison with other global oceans like the Pacific and Atlantic in two very important ways, which are crucial to understanding its importance to global climate. First, the IO is completely bounded to the north at around 25^{o} N meaning that the majority of the basin sits in the tropical region of solar heating year-round. This is important because it means that a huge amount of heating will go into the IO with very little opportunity to ventilate and mix with cooler ocean water in the mid-latitudes. Accordingly, ship-based observations of the mean annual heat flux indicate that there is a large net heating going into the North IO (Oberhuber 1988; da Silva et al. 1994; Josey et al. 1999). Secondly, during the summer monsoon months (JJAS) this excess heat is transported southward via Ekman transport which is caused by the mean monsoon westerlies across the basin. In the winter the circulation reverses, and mean winds across the equator import heat from the Southern IO. Because of its distinctive climate, the role that ocean processes and the surface net heat flux (NHF) play in regulating the SST and mixed layer depth is uniquely important in the IO (Godfrey et al. 1995; Garternicht and Schott 1997).

The NHF (Q_{net}) is made up of four components: latent heat flux (Q_{lh}), sensible heat flux (Q_{sh}), incoming solar flux (Q_{sw}), and outgoing terrestrial longwave radiation (Q_{lw}). The latent heat flux acts to cool the ocean surface through evaporation and is a function of both the air-sea humidity gradient and surface wind speed. As previously noted, incoming solar fluxes can be very large in the North IO because it is completely bounded in the tropical region. The incoming

solar radiation generally is larger than outgoing longwave radiation and thus solar radiation acts to warm the SSTs.

On intraseasonal timescales Q_{lh} and Q_{sw} have the largest variability and thus contribute the most to the variability of Q_{net} (Sengupta and Ravichandran 2001; Parampil et al. 2016). Parampil et al. (2016) using satellite observations and ship-based fluxes from 2003-2007 concluded that, during the ISM, Q_{net} accounts for the majority of the SST variability associated with the ISO. They noted that areas with the largest SST and Q_{net} intraseasonal variability were associated with areas of active convection indicating the importance of the relationship between SST and Q_{net} on intraseasonal timescales. Using ocean general circulation model (OGCM) experiments, Han et al. (2006) found particular importance for the wind speed and wind stress in regulating SST intraseasonal variability in the North IO. Halkides et al. (2015) examined the importance of the NHF on the intraseasonal mixed layer temperature in the IO and confirmed that, in agreement with other studies, Q_{net} has a larger impact on the intraseasonal SST and upper ocean than ocean related dynamics like vertical mixing, Ekman currents, and entrainment. However, they noted that this was not true near the equator, and found that the SST was regulated more by horizontal advection by the wind than by the NHF. The SST in the IO also exhibits strong internal basin-wide interannual variability through the Indian Ocean Dipole (IOD; Saji et al. 1999) and by remote forcing through the El Nino Southern Oscillation (ENSO; Webster et al. 1998). A study by Murtugudde and Busalacchi (1999) attempted to parse the separate influences of ENSO induced SST variability from non-ENSO SST variability and found that interannual IO SSTs have a correlation of only -0.51 suggesting that non-ENSO related variability may be important. They suggested that interannual variability of the wind speed associated with latent heat fluxes as well as variability in the cloudiness and solar radiation are

possible mechanisms through which non-ENSO related SST interannual variability could be achieved. In an OGCM experiment, de Boyer Montegut et al. (2007) analyzed the interannual variability of IO mixed layer temperature and found that the BoB and eastern Arabian Sea (AS) are mostly control by the latent heat flux through the winds, whereas the western AS is controlled mostly by vertical mixing and ocean processes.

1.4.2 The Heat Flux Dilemma

Observational estimates of the long term NHF in the IO vary considerably (see Fig. 3 from Yu et al. 2007) and demonstrate large remaining uncertainties regarding the NHF over some parts of the IO. Ocean model simulations also indicate similar uncertainties in the long-term NHF (Godfrey et al. 2007). Meanwhile, the IO has shown a steady increase in SST over the 20th Century in relation to increased greenhouse gas concentrations. The observed trend indicates that an increase in SST of 0.5^{o}C has taken place during the past century. Coupled GCM simulations of the 20th Century climate forced with observed greenhouse gas concentrations from the Intergovernmental Panel on Climate Change Fourth Assessment Report (IPCC AR4) also simulate a basin-wide warming trend over the North IO (Pierce et al. 2006; Knutson et al. 2006; Alory et al. 2007). The cause of this trend however has proved difficult as Yu et al. (2007) showed that not only is there very little trend at all in the long term mean NHF from observations, but the variability in the long term mean between different products (Fig. 3) is greater than what would be detectable in a trend. Interestingly, when attempting to investigate the mechanisms for the warming trend in the AR4 simulations, Du et al. (2008) point out that the mean NHF over the period is virtually 0. This leads to the question of how the IO could be warming over the past century while the mean NHF over the same period indicates neutral net

heat into the ocean. Attempting to explain the causes for this, Du et al. (2008) decomposed the NHF into the greenhouse gas response, atmospheric feedback and the cooling response by the ocean, and showed that warming occurs due to the increased longwave forcing by greenhouse gases, and atmospheric feedbacks through the latent heat flux. However, this warming is nearly canceled by a large ocean cooling response.. Du et al. (2008) proposes that the IO ocean climate adjusts to the increased greenhouse gas forcing by warming the SST and increasing the latent heat flux such that the NHF is nearly 0 when averaged over a long enough period of time. The significance of this quasi-equilibrium climate theory for the ocean response to global warming is that, analysis of the SST warming trend through the long term NHF will be difficult because the warming trend is so small and may not even be detectable. Greater insight is found by decomposing the NHF into its components and analyzing these components in terms of the relevant feedback processes.

1.5 Experimental Layout and Objectives

For this study, we conducted seasonal and multiyear simulations of the ISM using the Regional Spectral Model (RSM; Juang and Kanamitsu 1994; Kanamitsu et al. 2010) in order to understand how the representation of ice and liquid water saturation within a climate model reflects upon the mean seasonal ISM. The authors believe the ISM region to be ideal for a study such as this because of the enormous amount of rainfall, convection and water vapor that is present during the monsoon, especially in the upper atmosphere (Gettelman et al. 2006). The focus of this model experiment is based on a comparison of simulations where SVP over ice above the freezing level is calculated (wIce), with an identical set of simulations where SVP over liquid water is calculated throughout the atmospheric column (woIce). The calculation of SVP

filters down to all other moisture variables such that we anticipate the first order effect from the difference in SVP in the two sets of simulations to be seen in the moisture field. We expect that an important second order effect will be observed in cloud distributions of model layers that lie above the freezing level. Here, we emphasize that the scope of this study is limited to an evaluation of the impact that the SVP calculation has on the seasonal mean ISM representation in the model. In some cases, vastly different assumptions are made regarding SVP in numerical models currently used, including the climate models shown in Table 1. To date, there has not been an attempt to understand the implications of different saturation assumptions above the freezing level and the effect this may have on a model's humidity distribution, precipitation, cloud amount, and radiative flux.

Motivated partially by results found in the uncoupled simulation described above and also by a desire to match with current and state-of-the-art studies, we repeated the uncoupled multiyear simulations with coupling to the Regional Ocean Modeling System (ROMS), adding interactivity between the ocean and atmosphere. In addition to the wIce and woIce experiments we introduced a third experiment where we allow the SVP to be linearly interpolated between SVP over liquid water and SVP over ice for the region between 0^{o}C and -20^{o}C (MIX). This same type of formulation is used in the CFSv2, GFDL-AM3, and CCSM4 climate models (Table 1). What this additional experiment essentially does is roughly take into account the presence of supercooled water above the freezing level.

As we will show, the difference in the NHF between wIce and woIce in the uncoupled simulations showed an imbalance, with net heating in the Arabian Sea and net cooling in the eastern equatorial Indian Ocean (EEIO). We would hypothesize that if this same forcing was applied with an interactive ocean, as we propose to do with RSM coupled to ROMS (RSM-

ROMS), the SSTs over the IO during ISM will respond to the changes in the net heat flux and result in larger interannual and possibly intraseasonal variability during the monsoon.

The RSM-ROMS simulations also serve the added purpose of providing a means to analyze the importance of air-sea interactions during the monsoon ISO. To date there have been a host of studies which have utilized prescribed SST simulations along with fully coupled simulations to understand the relative importance of internal atmospheric dynamics versus air-sea coupling, to the northward propagation of ISOs (Rajendran and Kitoh 2006; Seo et al. 2007; Klingman et al. 2008; Wang et al. 2009). However, most of these past experiments were conducted from a forecasting perspective, focusing on a handful of ISO events, and at a relatively coarse horizontal resolution. With this study, we aim to analyze this importance in a similar way to previous studies, but with multiyear, high-resolution regional climate simulations.

1.6 Climatological wIce and woIce difference from Reanalysis

If we assume that above the freezing level, ice will be present, then given the relative humidity calculated with respect to liquid water, we can calculate the mixing ratio of water but with the SVP over ice used instead of liquid water. Given a reanalysis it is then possible to estimate what the climatological "loss" in water would be if SVP over ice was used to calculate the mixing ratio above the freezing level. Essentially, how much potential overestimation is made in the amount of moisture by assuming SVP over liquid water throughout? To answer this we have used the National Center for Environmental Prediction (NCEP) R2 reanalysis (Kanamitsu et al. 2002) and calculated this potential overestimation. An eight year time period from 2000-2007 is used in this calculation. We note also that R2 reanalysis was built assuming saturation over liquid water throughout the atmosphere. Fig. 2 shows the seasonal climatology of

this overestimation in terms of integrated moisture or precipitable water. The overestimation field follows several recognizable seasonal mean features of the climate. For example, the minimum in overestimation coincides with the seasonal subtropical highs and deserts of the world generally between 30 and 10 degrees latitude north and south of the equator. We notice too that a year-round maximum in overestimation occurs in the southern hemisphere at around 60 degrees south. This is associated with two climate features: 1) the southern hemisphere polar jet or Antarctic circumpolar current which is located slightly north of this maximum and 2) the freezing level at the surface. At around 60 degrees south the mean temperature year-round stays near freezing meaning, starting at this latitude, the calculation of SVP over ice is applied to the entire atmospheric column resulting in the largest departures from SVP over liquid water. Lastly, we notice local maxima in overestimation in equatorial convectively active regions that follow the seasonal movement of the ITCZ. During JJA we see the clear signature of the Indian summer monsoon (ISM) in the equatorial Indian Ocean and Bay of Bengal. Note here that the ISM along with the west African monsoon hold the largest departures from SVP over liquid water anywhere in the tropics. During JJA a large portion of south Asia shows a departure of at least 0.5 kg/m^2. The departures from SVP over liquid water found here highlight the need for investigation in these convectively active regions of the tropics namely the ISM region.

Table 1. Climate Model SVP Parameterizations

Model	Liquid	Mixed	Ice
CFSv2 Saha et al. (2014)	T > 0ºC	Linearly interpolate between liquid and ice for 0ºC > T > -20ºC	T < -20ºC
GFDL-AM3 Donner et al. (2011)	T > 0ºC	Linearly interpolate between liquid and ice for 0ºC > T > -20ºC	T < -20ºC
NASA-GISS ModelE Schmidt et al. (2014)	If over ocean, T > -4ºC, if over land, T > -10ºC	Probability exists for either phase if over ocean and, -4ºC > T > -35ºC, or over land if -10ºC > T > -35ºC	T < -35ºC
CCSM4 Meehl et al. (2012)	T > 0ºC	Linearly interpolate between liquid and ice for 0ºC > T > -20ºC	T < -20ºC
MPI-ESM Giorgetta et al. (2013)	T > -35ºC	Saturation over liquid water assumed	T < -35ºC

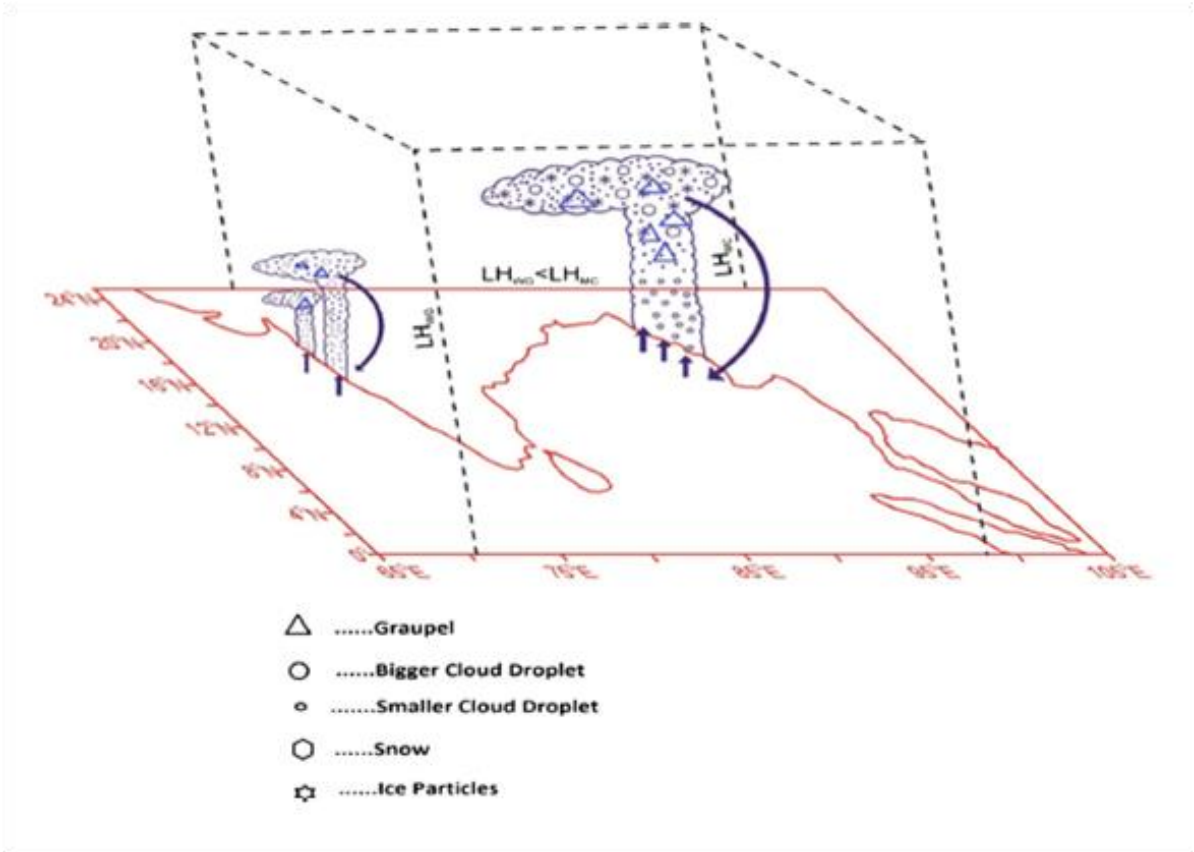

Figure 1. Conceptual model of the processes leading to differences in cloud organization and precipitation over the Myanmar Coast (MC) and Western Ghats (WG). [From Kumar et al. 2014]

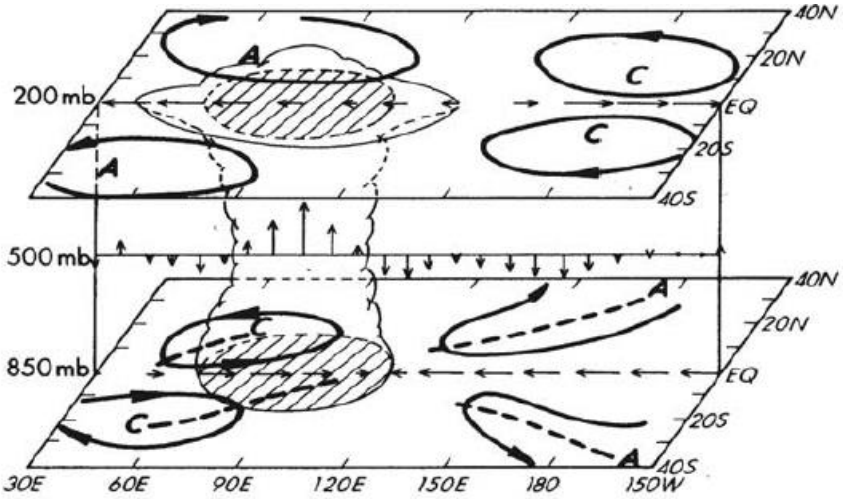

Figure 2. A schematic illustration of the formation of cyclonic (C) and anticyclonic (A) circulations associated with MJOs in the equatorial Indian Ocean (IO). [from Rui and Wang, 1990]

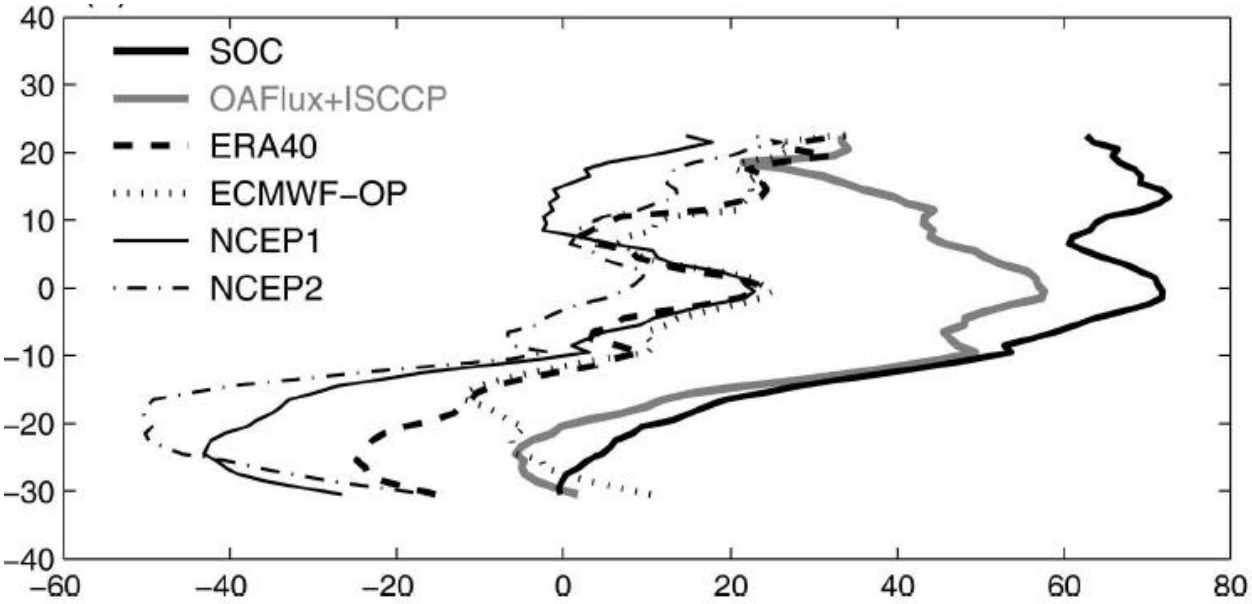

Figure 3. The long-term zonal mean of Q_{net} calculated from six heat flux products. SOC is the Southamption Oceanography Centre (Josey et al. 1999), NCEP 1 and 2 are the National Centers for Environmental Prediction reanalysis version 1 and 2 respectively, ECMWF-OP is the European Center for Medium Range Weather Forecasting (ECMWF) operational forecast analyses, ERA-40 is the ECMWF Reanalysis-40, and OAFlux+ISCCP is the flux product described in Yu et al. 2007. [from Yu et al., 2007]

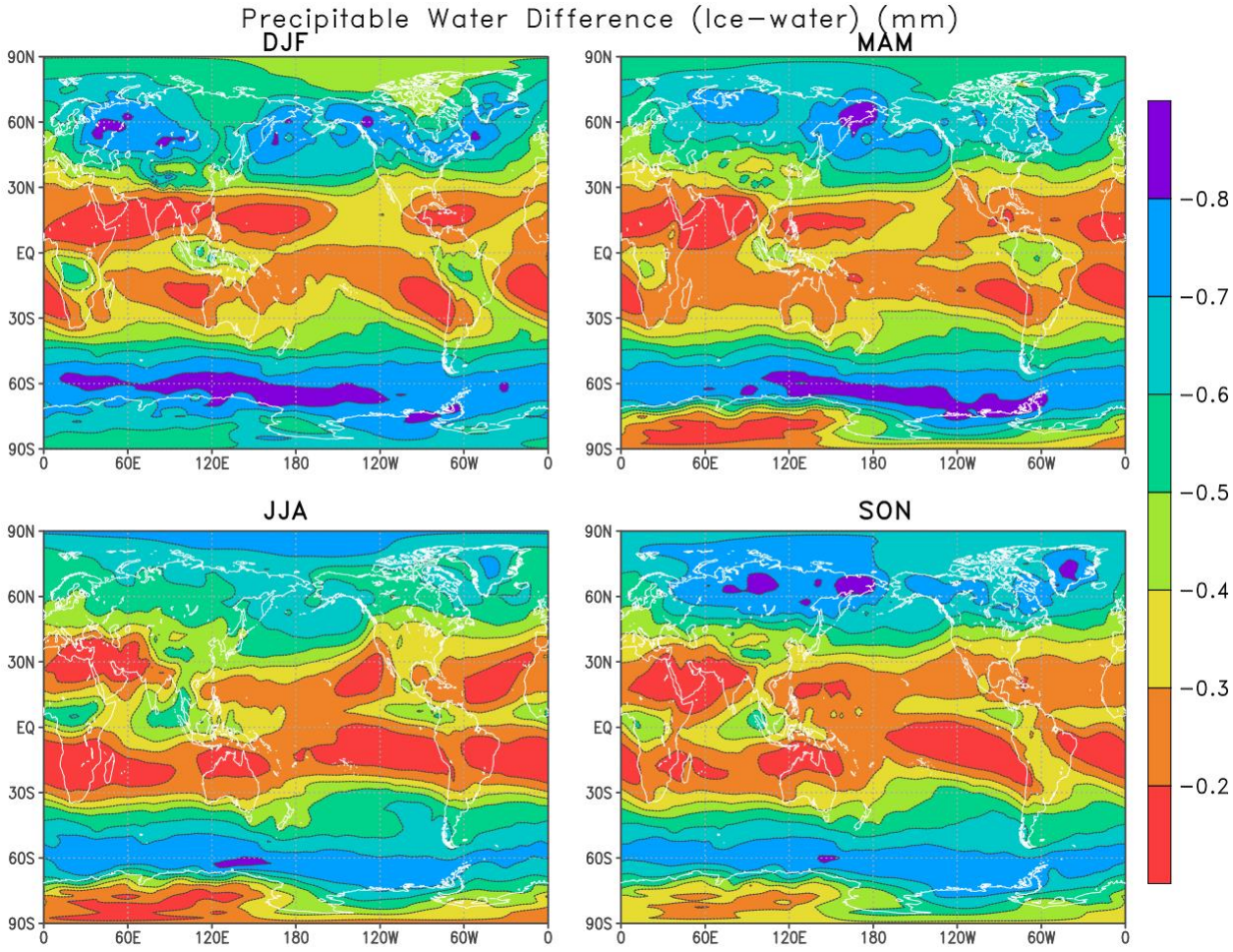

Figure 4. The seasonal mean difference in precipitable water (mm) calculated with SVP over ice minus precipitable water calculated with SVP over liquid water, from R2 reanalysis. R2 moisture variables originally assume SVP over liquid water.

CHAPTER 2

DATA, MODEL DESCRIPTION, AND EXPERIMENTAL DESIGN

2.1 Atmosphere-only Experiments

2.1.1 Model and experimental setup

The Regional Spectral Model (RSM; Juang and Kanamitsu 1994; Kanamitsu et al. 2010), originally developed at the National Center for Environmental Prediction (NCEP), is used in all model simulations for this study. The RSM uses a spectral method to evaluate the primitive equations. Previously it has been used in a host of regional climate studies (Stefanova et al. 2012; Li et al. 2013a, b; Li and Misra 2014). This study focuses strictly on the impact in the RSM simulation with prescribed SST and includes no coupling to an ocean model.

For this study, seasonal simulations were conducted for the period May 1 – October 15 for five separate years (2001, 2003, 2005, 2012 and 2013). These years were selected because neutral El Niño Southern Oscillation (ENSO) conditions were present in the Niño 3.4 region (5^oS-5^oN and 170-120^oW) and it was desirable to avoid possible influence on the ISM from an ENSO event (Rasmusson and Carpenter 1983; Webster et al. 1998). It is, however, recognized that the ISM exhibits interannual variability from other sources such as Indian Ocean Dipole (IOD) (Ashok et al. 2001; Saji et al. 1999), Himalayan mountain snow pack (Hahn and Shukla 1976) and internal variations of the ISM itself (Krishnamurthy and Shukla 2000, 2007; Goswami 1998). Influence from these conditions on our model results cannot be ruled out, however we have mitigated the influence of ENSO on the ISM through the selection of these five neutral years.

For each season we conducted two simulations, each with a different SVP parameterization. In one, the SVP was calculated with respect to liquid water in all model layers where the temperature is greater than 0^{o}C, and then for all layers above the freezing level (below 0 ^{o}C), calculated with respect to ice. These simulations are referred to as wIce ("with ice"). In a second set, the SVP was calculated with respect to liquid water throughout the atmospheric column. These simulations are referred to as woIce ("without ice"). A total of ten seasonal simulations were carried out. The method used to calculate the SVP follows Marx (2002). This method offers high accuracy outside the observed atmospheric temperature domain while maintaining a high level of computational efficiency. It was noted in Shimpo et al. (2008) that there are discrepancies between parameterizations in the RSM and the method used for calculating relative humidity and SVP. For this study, the method used for calculating SVP (and relative humidity) was implemented throughout the model and all of its parameterizations so that it is consistent. In addition to seasonal runs, two 13-year simulations were conducted from 2001 through 2013 using the same domain configuration and boundary conditions as the seasonal runs. One of these multiyear runs used the wIce parameterization and the other used the woIce parameterization.

The model domain chosen for this study (Fig. 5) encompasses the major features of the ISM region and provides a sufficient area over which to simulate the ISM. Atmospheric boundary conditions were provided by NCEP R2 reanalysis (Kanamitsu et al. 2002) along with daily updated Optimum Interpolation Sea Surface Temperature (SST; Reynolds et al. 2007) data for the ocean boundary conditions. The horizontal grid spacing is 15km with 28 terrain following sigma-coordinate vertical levels that are identical to those used by the NCEP-DOE Reanalysis (R2; Kanamitsu et al. 2002) which facilitates the integration of the atmospheric boundary

conditions during model simulation. It is recognized that other higher-resolution, state-of-the-art reanalyses datasets exist that would provide greater accuracy for the atmosphere's boundary conditions, however because of the advantage regarding the matching vertical resolution and because of it's common use in climate simulation studies, we chose to use the R2 Reanalysis for atmospheric boundary conditions. The shortwave and longwave radiation schemes used are Chou (1992) and Chou and Suarez (1994) respectively. For the convection scheme, the RSM uses a Relaxed Arakawa-Schubert scheme (Moorthi and Suarez 1992). The RSM utilizes a Scale Selective Bias Correction (SSBC; Kanamaru and Kanamitsu 2007), which prevents the model on the largest spatial scales resolved within the regional model, from deviating from the large-scale lateral boundary conditions (in this case R2 reanalysis).

2.1.2 Observational datasets

In addition to the ocean and atmospheric datasets used for boundary conditions in these model simulations, we also utilized several observational datasets for comparison and validation of the model results. The Global Precipitation Climate Project (GPCP) version 1.2 (Huffman et al. 2012) monthly mean (2.5^o by 2.5^o) rainfall data, for the period 1997-2006, were used for comparison with the model's seasonal mean rainfall. It is recognized that caution should be taken when comparing GPCP to our simulations because of the significant difference in horizontal resolutions and in this study a limited comparison of the long-term seasonal mean rainfall is made. For the same period, daily outgoing longwave radiation (OLR) (Liebmann and Smith 1996) retrievals from the Advanced Very High Resolution Radiometer (AVHRR) were used for comparison with modeled seasonal OLR. NCEP R2 reanalysis winds and specific humidity were also used for comparison and analysis of model results.

Because of the direct relevance of cloud distribution and statistics to this study, it was important to evaluate the modeled cloud statistics against an observational dataset and to understand what the observed mean cloud distribution should look like during the ISM. For this purpose, two widely used satellite datasets of cloud statistics: the International Satellite Cloud Climatology Project (ISCCP; Rossow and Schiffer 1991, 1999) and the Moderate Resolution Imaging Spectroradiometer (MODIS) are available. While both datasets are reliable choices for resolving the column-integrated cloud field (total cloud), it was pointed out by Chang and Li (2005) that ISCCP has difficulty detecting the cloud tops of layered or overlapped clouds when, for instance, thin high cirrus clouds overlay thicker low clouds. MODIS attempts to improve upon the detection of these thin cirrus clouds by using CO_2 slicing (Platnick et al. 2003). For these reasons, we chose to use the layered-cloud and column integrated cloud amounts provided by MODIS level 3 daily data (Platnick et al. 2015) for comparison with modeled clouds.

2.1.3 Cloud Scheme

For this study, the RSM uses a cloud scheme based on Slingo (1987, 1991) in which cloud fraction is diagnosed at each grid cell based on atmospheric conditions that are physically relevant to cloud formation such as, relative humidity, vertical velocity, and inversion strength in the case of low level clouds. Slingo (1987) groups clouds into four categories, three of which are based on height (i.e., low, medium, high) and a fourth for convective clouds. For low, middle, and high clouds diagnostic equations for the cloud amount as a function of the mean background relative humidity of a grid cell are in the form:

$$C = \left(\frac{RH - RHc}{1 - RHc}\right)^2 \text{, for RH} > \text{RH}_c \quad (1)$$

$$C = 0, \text{ for } RH \leq RH_c$$

Where C is the cloud amount, RH is the mean relative humidity in the grid cell, and RH_c is the critical relative humidity. RH_c is set to 0.85 for high clouds over land and ocean, 0.65 for middle clouds over land, 0.85 for middle clouds over ocean, 0.9 for low clouds over land, and 0.7 for low clouds over ocean. For low clouds, there are two additional parameterizations to account for the possible presence of boundary layer inversion type clouds or low level clouds associated with synoptic scale disturbances, but these will not be discussed in detail here. Convective clouds can occupy any of the three other levels and the amount comes directly from the convection scheme.

It is recognized that the use of a diagnostic cloud scheme in this case may have disadvantages. For one, the absence of prediction of cloud water or ice is limiting in the detail by which the cloud amount is calculated as well as the representation of precipitation that is not convective in nature. Further, the large-scale precipitation in RSM is produced from the instant removal of supersaturation. We argue, however, that the advantages to using a more detailed prognostic cloud water scheme are small here. In a study of four cloud schemes (one of which was Slingo) in the G-RSM (Global-RSM), Shimpo et al. (2008) found little benefit to using a prognostic cloud scheme. They concluded that no single cloud scheme could be distinguished from the others as clearly better performing. Shimpo et al. (2008) recommended improvements to several common cloud water prediction schemes on account of their poor representation of cloud water relative to observations. Furthermore, in a study of three cloud prediction schemes, one being the Slingo scheme, and another being the Xu and Randall (1996) prognostic cloud water scheme, Wood and Field (2000) found that the Slingo scheme performs relatively well in terms of cloud amount when compared to observations and the Xu and Randall scheme. While a prognostic cloud scheme with additional parameterizations for cloud microphysical processes

that are not included in a diagnostic scheme like Slingo is preferable, we argue that these additional processes may not have direct relevance to the SVP calculation. Relative humidity on the other hand, is clearly and quite directly affected by the SVP. We would then argue that a cloud scheme that determines cloud amount mainly as a function of relative humidity is the most direct way of testing the impact of SVP on cloud distribution qualitatively. Essentially, we offer this experiment using the Slingo scheme as an initial step toward understanding the affect that SVP has on a numerical simulation. Still, we recognize that the benefits of a more detailed representation of cloud microphysical processes would offer a more complete test, and we are exploring additional experiments with more complex cloud schemes that will be reported in a future study.

2.1.4 Verification of Ice vs. liquid water relation

Before entering into an analysis of the model results, it is important to first understand the theory behind the changes that have been made to the model and to verify that the model is indeed producing what we expected from the changes made to the calculation of SVP. The theoretical difference between the wIce and woIce simulations were how SVP was calculated above the freezing level. This is understood through the Clausius-Clapeyron relation which is used to calculate SVP in the model.

$$e_s = \varepsilon e^{\frac{l_v}{r_v}(\frac{1}{T_0}-\frac{1}{T})} \quad (2)$$

$$e_{si} = \varepsilon e^{\frac{l_s}{r_v}(\frac{1}{T_0}-\frac{1}{T})} \quad (3)$$

Equations (2) and (3) are Clausius-Clapeyron relations for calculating SVP over water and ice, respectively, where e_s is the SVP over water, e_{si} is the SVP over ice, T_o is the freezing point (273.15 K), T is the environmental temperature, r_v is the gas constant for moist air, and ε is the vapor pressure at temperature T_o. l_v and l_s are the latent heat of vaporization and sublimation respectively. Equation (2) is then representative of SVP calculation in the woIce runs and equation (3) is representative of SVP calculation in the wIce runs, above the freezing level. We can verify this by plotting the model derived SVP and corresponding temperature in the wIce and woIce runs along with the theoretical Clausius-Clapeyron relation for ice and liquid water (Fig. 6a). We expect that the SVP derived in the wIce runs should follow the theoretical curve for SVP over ice and that the SVP derived in the woIce runs should follow the theoretical curve for SVP over liquid water. In general, this was the case as shown in Figure2a. Taking the hourly model derived SVP and temperature from grid points along an equatorial cross section, we found that the points from wIce and woIce were very closely clustered around their respective Clausius-Clapeyron relation. The SVP from the model shown here will not exactly follow the Clausius-Clapeyron relation for a few reasons: 1) the SVP is inferred from the specific humidity (q) and relative humidity, so it is not the exact SVP from the model at that timestep and 2) the output from the model is interpolated to pressure levels from the native sigma levels.

We are also interested in the difference in SVP between wIce and woIce on hourly timescales because this will have direct implications for differences in cloud formation between wIce and woIce. The difference in SVP will also be important for beginning to understand how sensitive the model is to the SVP calculation. Fig. 6b shows the difference in SVP (for a given temperature) between wIce and woIce from model levels at the same locations as in Fig. 6a. The theoretical difference in SVP from Clausius-Clapeyron is also shown for comparison. Notice that

the greatest theoretical difference in SVP for ice and liquid water is at -12.5 ^{o}C. Notice also that the data in Fig. 6b (and Fig. 6a) are clustered according to the model level that they are taken from and that, in this case, there are three clusters for this temperature range that correspond to 500mb, 400mb and 300mb. The greatest difference in SVP is then theoretically between 400mb and 500mb in the atmosphere for this equatorial region. The data from the 300mb level generally follows the theoretical relation closely while grid points near the max SVP difference at -12.5 ^{o}C shows greater variability. In general, it seems that the departure of the model from the theoretical SVP difference increases near the maximum difference at -12.5 ^{o}C.

2.2 Coupled Model Experiments

In another set of SVP experiments, an interactive ocean component is added by coupling RSM to the Regional Ocean Modeling System (ROMS; Haidvogel et al. 2000). The ROMS component is run on the same domain and at the same horizontal grid spacing as the previous RSM-only experiments. With respect to ROMS, there are 30 sigma coordinate vertical levels with vertical stretching such that more levels are packed near the ocean surface (the first sigma level is typically between 10 and 50m depth). Environmental variables at the ocean-atmosphere interface are exchanged between RSM and ROMS at 3 hour intervals. This is important for resolving diurnal cycles in air-sea interaction. This version of the model with RSM coupled to ROMS is referred to as RSM-ROMS.

For these experiments, the wIce and woIce setups from the RSM-only experiments are used along with a third configuration called "MIX" in which the SVP between temperatures of 0^{o}C to -20^{o}C is linearly interpolated to be between over liquid water and over ice or,

$$e_s = e_{si}\left(1 - \frac{T - T_{-20}}{T_0 - T_{-20}}\right) + e_{sw}\left(\frac{T - T_{-20}}{T_0 - T_{-20}}\right) \quad (4)$$

where T is the given temperature, T_0 is the freezing temperature, T_{-20} is -20^{o}C, e_{si} is the SVP over ice at the given temperature, e_{sw} is the SVP over liquid water at the given temperature, and e_s is the interpolated SVP. This type of SVP formula is used in the GFDL-AM3, CCSM4, and CFSv2 climate models (Table 1). In total there are three RSM-ROMS simulations, wIce, woIce, and MIX. Each simulations is run for the period 1997-2010 using NCEP-R2 as boundary conditions for RSM and the Simple Ocean Data Assimilation version 2 (SODAv2; Carton et al. 2000; Carton and Giese 2008) as boundary conditions for ROMS. The entirety of 1997 is not used for the analysis to allow the ocean to sufficiently gain kinetic energy from the coupled winds and "spin-up".

2.3 Intraseasonal Analysis

In order to analyze the evolution of monsoon ISO peaks and troughs, relevant variables from the model simulations and observations are filtered using a 4th order, bandpass, recursive Butterworth time filter (Guillemin 1957). A filtering scheme such as this has been used to isolate intraseasonal signals in several passed studies of the ISO (Misra et al. 2018; Goswami et al. 1998; Krishnamurti and Subrahmanyam 1982). The bandpass we use isolates variability on scales of 30-60 days, thus we are focusing our analysis on the more prominent 30-60 day oscillation associated with MJO and not on the less prominent 10-20 biweekly oscillations. ISO peaks are then defined as the day on which the maximum 30-60 day rainfall anomaly, averaged over 10^{o}N-25^{o}N and 70^{o}E-90^{o}E, is found over a slice of days exceeding 1 standard deviation of the rainfall anomaly timeseries for that monsoon year. Using this definition we can construct a

composite of ISO peaks from which we may observe the mean evolution of associated atmospheric and ocean anomalies.

Satellite derived precipitation from the Tropical Rainfall Measurement Mission (TRMM; Huffman et al. 2007) 3B42 and SST from the NOAA Optimum Interpolation SST (OI-SST) blended satellite, ship track, and buoy dataset (Reynolds et al. 2007) are filtered and used to construct an observed ISO composite for comparison with our model simulations. OI-SST data are mainly composed of data from two satellites, the Advanced Very High-Resolution Radiometer (AVHRR) and the Advanced Microwave Scanning Radiometer (AMSR-E). Both TRMM and OI-SST data have a horizontal spacing of 0.25^{o} x 0.25^{o} with a daily time increment. The TRMM and OI-SST data used for this analysis is from the period 2003-2010.

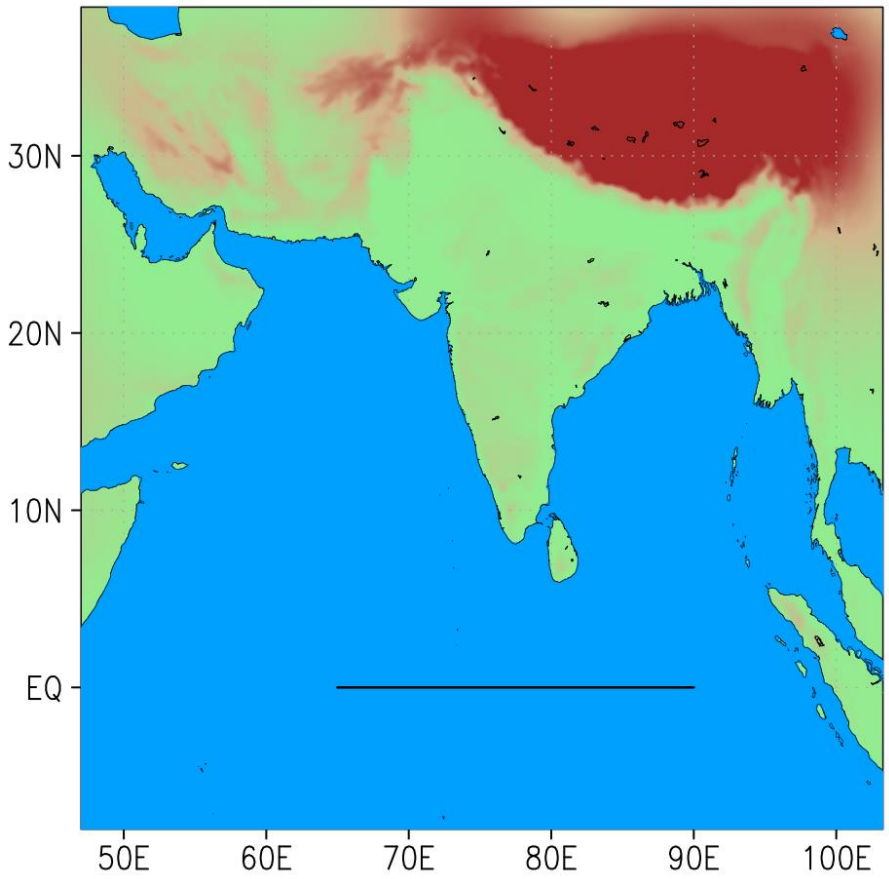

Figure 5. Model domain used for all simulations in this study. Darker shades of brown indicate increasing height of topography. The solid black line along 65E-90E indicates the grid points used to construct Fig. 6.

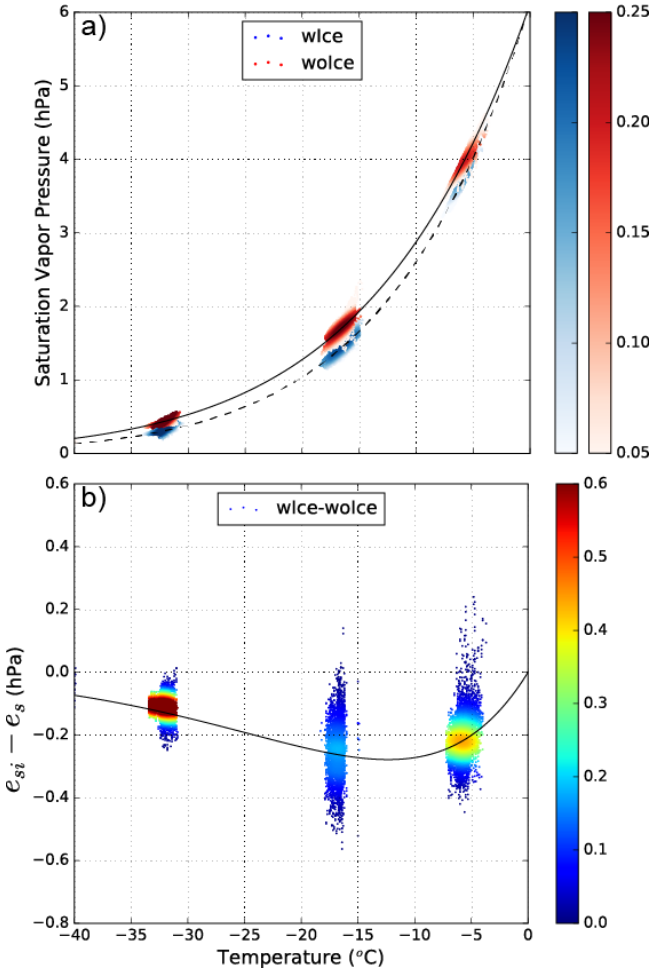

Figure 6. (a) The SVP (hPa) plotted with the temperature of grid points taken from the region indicated in Fig.1. Red dots indicate data from grid points in the woIce simulation while blue dots indicate data from the wIce simulation. The dotted black line indicates the SVP calculated with respect to ice using the Clausius-Clapeyron relation and the solid black line indicates the SVP calculated with respect to water using the Clasius-Clapeyron relation. (b) The difference in SVP (hPa) (e_{sice}-e_{swater}) plotted with the corresponding temperature at grid points taken from model simulations at the same locations as in (a). The solid black line in (b) indicates the difference of SVP calculated with respect to ice minus the SVP calculated with respect to water using the Clausius-Clapeyron relation. The shading of the points in (a) and (b) indicate the probability density function of the data using a Gaussian kernel density estimation. Higher probability density values indicate greater clustering of the data. All data are gathered in both simulations from 00z May 29 to 00z May 31 2001 at hourly intervals. Note that model output is in pressure levels and data are clustered into three groups which correspond to 500mb, 400mb, and 300mb.

CHAPTER 3

SVP MODEL EXPERIMENTS

3.1 Comparison with Observations

We expect that, because of changes made to the calculation of SVP in the model experiments and by association the moisture and relative humidity, the model cloud-layer fields will differ between wIce and woIce, especially in the middle and high cloud regime where most the atmosphere is below 0^{o}C. To start, we evaluated the modeled high, middle, low and total cloud fields against the satellite derived fields from MODIS. It is important to note, however, that the cloud layer and total cloud amounts from RSM are calculated using a maximum-random overlap assumption while MODIS cloud fields were derived from the satellite's top-down view from space with no assumptions about cloud overlap. Therefore, to facilitate comparison with MODIS, the model cloud layer fields were transformed to mimic a top-down view of the cloud layers following the method of Weare (2004) and Shimpo et al. (2008). For modeled high clouds, the amount is theoretically the same as that seen from space by MODIS. For middle clouds, the amount "as seen from space" is equal to the model derived middle cloud amount minus the high cloud amount that obscures the middle clouds using a "random overlap assumption." This can be expressed in the following relation:

$$mid\_asfs\_cf = mid\_cf * (1 - high\_cf) \quad (5)$$

where high_cf is the model-derived high cloud amount, mid_cf is the model-derived middle cloud amount and mid_asfs_cf is the middle cloud amount as seen from space in the model. The low cloud amount that is as seen from space is then the model derived low cloud amount that is not obscured by middle or high clouds, or

$$low\_asfs\_cf = low\_cf * (1 - mid\_cf) * (1 - high\_cf) \quad (6)$$

where low_cf is the model-derived low cloud amount and low_asfs_cf is the low cloud amount as seen from space in the model.

Utilizing the relations above, we compared the mean monthly May-September cloud layer and total cloud amounts from the seasonal simulations with MODIS in Fig. 7. Both the modeled clouds and MODIS follow the monsoon seasonal cycle with a steady increase in cloud amount from May-June in the lead up to onset, and a peak in cloud amount occurring in July that coincides with the peak of the monsoon season before a decrease in clouds and convection from August-September. The model simulations generally showed more monthly variability than MODIS, especially with respect to high cloud amount. The model overestimated the high cloud amount during the peak of the monsoon season with respect to MODIS. This may be a symptom of the high cloud amount being sensitive to the activity of the convective parameterization. The middle cloud amount was also overestimated in the model, and showed greater seasonality than MODIS, while the low cloud amount was the only layer underestimated. Li and Misra (2014) also noted a bias for underestimation of low clouds in the RSM. With respect to total cloud amount, again we found strong seasonality in the model clouds which leads to underestimation outside of the peak monsoon months.

In comparing the wIce and woIce mean cloud amounts, we found the largest difference in the middle and high clouds where the high cloud amount in wIce was consistently larger by 5-7%. Middle clouds, however, were fewer in the wIce simulations by 1-3%. The total column cloud layer amount increased in wIce due mainly to the significant increase in high clouds. It is

worth noting that the mean cloud differences between wIce and woIce were nearly uniform across the monsoon season and did not change sign.

To evaluate the mean monsoon in the model simulations, we compared the model's June, July, August, September (JJAS) mean rainfall, OLR, and 850 hPa circulation with observations during the 10-year period 1997-2006 in Fig. 8. The model simulations tended to precipitate more in the Inter-Tropical Convergence Zone (ITCZ) region over the Equatorial Indian Ocean than in the GPCP observations. Over land, the model simulations and GPCP rainfall were in better agreement and the two main precipitating regions over the Western Ghats and Myanmar coast were easily identifiable in the model. It is clear from Fig. 8 that the mean seasonal rainfall in wIce and woIce appears very similar and that a closer analysis is needed (addressed in Section 3.4).

3.2 Moisture and Thermodynamics

The distinction between wIce and woIce is in the calculation of SVP above the freezing level. Therefore, it is important to first locate the freezing level and determine its spatial variability in the ISM region. Fig. 9a shows the JJAS mean freezing level across the model domain for the wIce simulations. We found that there was little difference in the height of the freezing level between wIce and woIce (not shown), and thus Fig. 9a can be taken as representative of both simulations. In general, the freezing pressure level decreases (increases in height) from south to north across the domain but remains between 600 to 500 hPa. Coincident with this rise in the freezing level was an increase in seasonal mean specific humidity (q) between the 600 to 500 hPa layer in the R2 reanalysis forcing (Fig. 9b). It follows then that the potential change in saturation is greater over India and the Bay of Bengal (BoB), where there is a

maximum in q, when saturation over ice is calculated instead of over liquid water. To consider whether this was indeed the case, Fig. 10 shows a zonally-averaged cross-section of the difference (wIce-woIce) in mean relative humidity, q and temperature with height for the JJAS period during the model simulations. A clear relative drying at the freezing level was apparent in the wIce simulations from the RH and q profiles (Fig. 10a and 10b). The maximum in relative drying from 10N to 20N between 500 and 600 hPa is a consequence of a coincident maximum in available moisture over India and the BoB. The amount of drying with respect to q decreased with height (Fig. 10b) because there is generally less water vapor with increasing height. A portion of the drying is also observed in q and RH below the mean freezing level. The reasons for this relative drying are related to two processes which involve convection. First, when vigorous convection occurs, condensation and rainfall will be increased above the freezing level in wIce relative to woIce. Precipitation will fall into the layers below the freezing level which will then trigger those layers, which are already close to saturation, to consequently condense and precipitate as well, thereby removing moisture from the column below the freezing level. A second process which can lead to drying below the freezing level is large-scale subsidence in association with convection. In the wake of convection, large-scale subsidence may bring relatively dryer air above the freezing level down to the layers adjacent to the convection below the freezing level. This is the result of condensation and rainfall occurring in the model levels above, precipitating into the layers below the freezing level, which then triggers those layers to saturate from evaporation of falling precipitation and consequently condense, serving as a moisture sink. For these layers below the freezing level, the seasonal mean water vapor removed as a result of condensation, and precipitation, and large-scale subsidence is greater than the addition of water vapor from evaporation into unsaturated layers.

As soon as the freezing level is crossed in wIce simulations, the saturation-specific humidity is dropped to be over ice. This means that the air will immediately be closer to saturation and, in some cases, may be supersaturated in the layers near the freezing level. With little change in the moisture advection and overall mean circulation between the wIce and woIce runs, the changes in the tendency of q between the two model simulations is then a function of precipitation and condensational processes. Any water vapor that condenses in the model is assumed to fall out as precipitation, leading to a decrease in q. In addition, any supersaturation is immediately removed in the model and converted to precipitation. It seems apparent then that the response of the wIce simulations to the slight decrease in SVP is to increase the grid-scale condensation and in doing so adds to a preexisting moisture sink in the model.

The difference in temperature (Fig. 10c) shows slight warming in the mid to upper troposphere which is located slightly above the freezing level and the region where maximum drying is occurring in wIce. The warming appears significant because it is consistent from south to north between 400 and 500 hPa. Diabatic latent heat released due to increased condensation may be the cause of warming in the mid and upper troposphere but this cannot be confirmed without a profile of diabatic heating and cooling, which was not accessible from the model simulations in this study. Also note that for this study modifications are only made to the SVP calculation. The latent heat of condensation for warm and cold rain processes continue to be included in both (wIce and woIce) runs.

Recognizing that the SSBC in the model may affect the results described here, the model simulations wIce were repeated without the SSBC and similar qualitative results were found (not shown).

3.3 Clouds and Radiation

Fig. 11 shows the spatial variability of the difference in the mean seasonal low, middle, high and total cloud amount between wIce and woIce. A decrease in middle cloud fraction can be seen (Fig. 11b) over most of the domain in wIce, which coincides well with the decrease in RH near the freezing level seen in Fig. 10a. Conversely, Fig. 11c shows an increase in high cloud amount over most of the ISM region with a maximum in the eastern equatorial Indian Ocean (EEIO) and BoB. The total cloud amount (Fig. 11d) is calculated as the maximum cloud coverage found out of the three cloud level categories, or total = max(low, middle, high). Since the high cloud amount is often the largest out of the three layers, any increase in the high cloud amount will generally lead to an increase in the total cloud amount. In Fig. 11d we observed an increase in total clouds over most of the region where the high clouds increased but over India where middle clouds are significantly decreased, the change to total clouds is negligible.

In the mean seasonal cloud field two distinct regimes emerge: one over the EEIO and southern BoB where an increase in high clouds occurs in the wIce runs, and another over India and the Arabian Sea where high clouds also increase but middle clouds decrease by a similar or greater amount in the wIce runs. Because of the strong coupling between clouds and radiation we see these regimes manifesting in the mean radiation fluxes shown in Fig. 12. For example, we observe that in the wIce run, at the surface, shortwave (SW) radiation is decreased over the EEIO as a result of increased high clouds, which adds to Earth's albedo relative to the woIce run. To understand the increase in SW radiation over the Arabian Sea and India in Fig. 12a it is important to know that stratiform clouds are parameterized to be more optically thick than cirrus clouds. In this case the middle clouds are mostly stratiform to the model and high clouds are cirrus type. This means that the SW radiation flux will be more sensitive to changes to the

middle cloud amount. Because the middle cloud amount decreases over the Arabian Sea and India in the wIce run, less SW radiation is absorbed in the atmosphere despite a similar magnitude increase in high clouds and thus an increase in surface SW flux is observed there. In terrestrial longwave (LW) radiation, clouds both absorb LW radiation from Earth's surface and emit LW to space and downward toward Earth. Because of the increase in SW radiation over the Arabian Sea and India in the wIce runs, the mean land surface temperature over India is slightly increased (not shown) and thus a net increase in outgoing LW radiation leaving the surface is observed (Fig. 12). Due to emission by clouds, the increase in clouds over EEIO in the wIce runs resulted in a gain in LW radiation at the surface. At top of the atmosphere (TOA; Fig. 12c and 12d) a loss can again be seen in SW over the EEIO as more SW is reflected back to space, while a gain in SW radiation is felt over the Arabian Sea and India, consistent with the relative changes in cloudiness in the wIce runs.

3.4 Seasonal Rainfall Characteristics

In section 3.2 it was found that the switch to saturation over ice above the freezing level in the wIce simulations caused a removal of moisture in the mid and upper troposphere. This removal of moisture suggests increased grid-scale condensation and conversion to rain within the model when saturation over ice is applied. It then follows that we should, in a seasonal mean sense, observe an increase in the amount of rainfall coming from the model's cloud scheme and not by the sub-grid-scale convective parameterization. This was investigated in Fig. 13 where the percentage contribution to the total mean seasonal rainfall from the grid-scale precipitation in wIce and woIce is shown. Since the total precipitation is made up of two components: grid-scale (explicit) precipitation and convective precipitation, we can analyze the impact on grid-scale

precipitation through its contribution to the total precipitation. Note that grid-scale precipitation is generally dominant over land whereas over the Indian Ocean it contributes less (Fig. 13). Over central India, where grid-scale precipitation makes up at least 70% of the seasonal rainfall in many places, it was found that the contribution of the grid-scale precipitation increased further by 3-4% in wIce (Fig. 13c). Indeed, we observed an increase of 2-3% in grid-scale precipitation for the wIce simulations over most of the domain (Fig. 13c).

Exactly how much grid-scale rainfall was added relative to the convective rainfall and did this amount vary over India vs. the Indian Ocean, recalling that grid-scale precipitation contributes less to the total over the ocean and ITCZ? One way to answer this would be to calculate the amount of rain that falls during JJAS in terms of volume to obtain a tangible understanding of how much seasonal rain the model produces. As shown in Fig. 14, the JJAS convective and grid-scale cumulative "rain volume" was calculated for India and equatorial Indian Ocean ITCZ (5^oN - 5^oS and 65^oE - 95^o E) . Again, the convective rainfall plus the grid-scale rainfall make up the total model precipitation. In total precipitation, an increase in rain volume in the ITCZ was observed from woIce to wIce, whereas the rain volume was nearly unchanged over India. Notice that the grid-scale rain volume increased in both regions, as expected from Fig. 13, but that this does not translate to an increase in total rain volume over India and does so over the ITCZ. Over India the increase in grid-scale precipitation is compensated by a similar magnitude decrease in convective rainfall. Based on what is shown here, it is clear that at least a portion of the moisture removed from the model in the wIce runs is converted to grid-scale rainfall production through the cloud scheme and that it is observable from a mean seasonal perspective.

3.5 Multiyear Simulations

It was desirable to conduct the wIce and woIce experiments a second time but letting the simulation progress for consecutive years instead of reintializing every season because of the possibility that the results found in the seasonal runs are influenced by the selected simulation years and related spin-up issues. From Fig. 15 we see that the model mean seasonal rainfall cycle over All India is slightly increased in the wIce relative to woIce multiyear simulations. The peak difference in All India rainfall also coincides with the seasonal peak in rainfall in late July. Fig. 16 shows the mean JJAS column integrated moisture or precipitable water, above the freezing level. Previously, in the seasonal runs we found a drying in the mid troposphere that was maximum near the freezing level in the wIce simulations. A similar result was found in the multi-year integrations where the precipitable water was consistently less by ~0.5 kg/m^2 in wIce compared to woIce (Fig. 16). Because the region over India contains greater integrated moisture above the freezing level than the ITCZ, the change in precipitable water, between wIce and woIce, over India was greater than over the ITCZ (Fig. 16). The difference in moisture content above the freezing level between wIce and woIce was generally constant throughout the multiyear simulations. Based on the results of the multiyear wIce and woIce experiments we find that the precipitation and moisture field differences as a result of SVP are largely unchanged when compared to the seasonal experiments.

To compliment the results from Section 3.4, Table 2 catalogs the mean and standard deviation statistics of the monsoon seasonal rainfall over All India and the ITCZ in the multiyear simulations compared with observations. The ITCZ rainfall was widely overestimated in both the wIce and woIce runs and the All India rainfall was underestimated, compared to GPCP and IMD observations. The standard deviation of the seasonal rainfall over All India was in better

agreement with observations. Note that over India the wIce simulation adds to the mean seasonal rainfall variability slightly whereas over the ITCZ it dampens the variability. In agreement with Fig. 16, the mean seasonal rainfall difference between wIce and woIce indicated a slight increase in rainfall in wIce. Comparing the mean seasonal All India rainfall difference to the observed standard deviation in the seasonal rainfall, we see that the mean difference between wIce and woIce (1.17 cm) is about 10% of the observed mean interannual variability of monsoon rainfall over India (8.08 cm in GPCP, 9.15 cm in IMD).

Table 2. ITCZ and All India Seasonal Cumulative Rainfall[a]

	IMD	GPCP	wIce	woIce	wIce-woIce
Mean	84.03	87.45 (76.95)	68.11 (150.5)	66.94 (148.74)	+1.17* (+1.76*)
SD	9.15	8.08 (7.63)	13.48 (31.53)	13.10 (32.50)	1.78 (1.96)

[a]Cumulative JJAS rainfall in cm. The wIce, woIce, and difference statistics were calculated from the multiyear simulation (2001-2013). IMD, India Meteorology Department rain gauge data from 1998-2003 (Rahman et al. 2009). GPCP, Global Precipiation Climate Project data from 1997-2011. Parenthesis indicate cumulative rainfall or standard deviation from the ITCZ (5^{o}N to 5^{o}S and 65^{o}E to 95^{o} E).

*Indicates statistical significance at the 99% confidence level

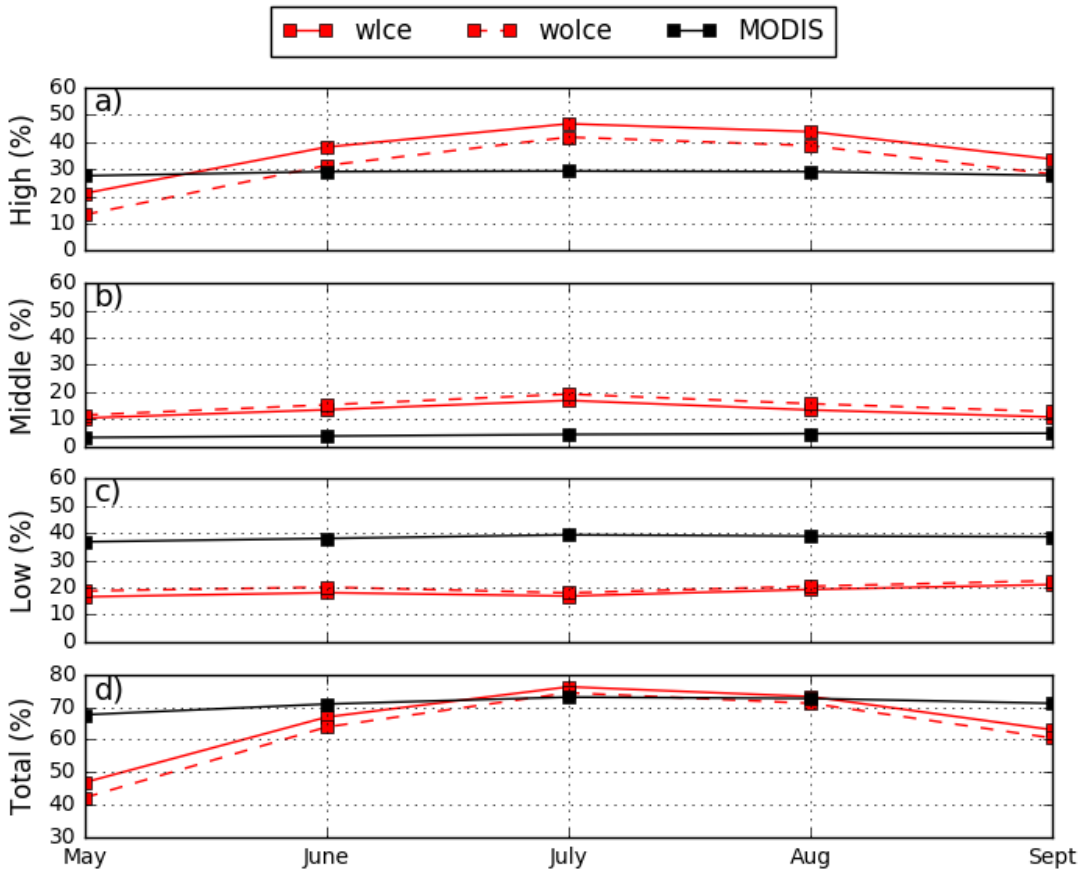

Figure 7. Monthly area averaged (a) high, (b) middle, (c) low, and (d) total cloud fraction (%) during ISM months over the ISM region, 5ºS - 25ºN and 60ºE - 95ºE. The mean of the five seasonal wIce and woIce simulations are represented in the red solid and red dashed lines respectively. MODIS monthly cloud fraction data averaged over a 13-year period (2002-2015) are represented with a solid black line. The middle and low cloud amounts from the model are transformed to be "as seen from space" to facilitate comparison with MODIS.

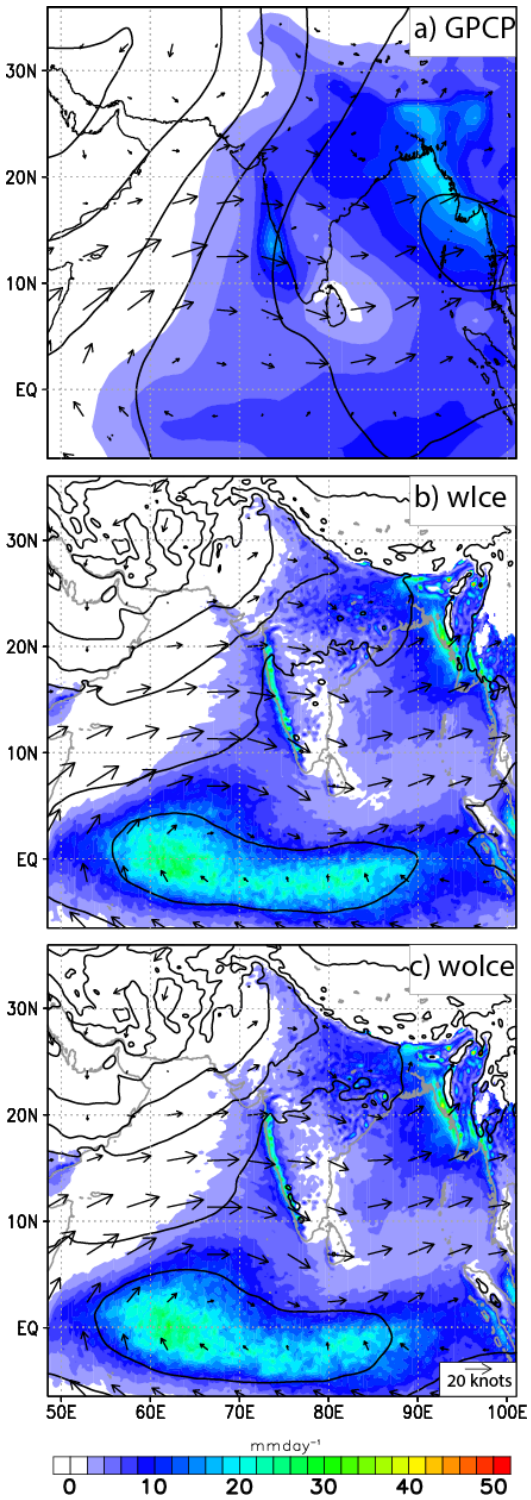

Figure 8. (a)GPCP daily rain rate (mmday^{-1}) shaded, R2 850hPa wind vectors (knots), and AVHRR satellite derived OLR (W/m^2) averaged over JJAS for the 10-year period 1997-2006. And JJAS mean rain rate, OLR, and 850hPa wind vectors for the 5 seasonal model simulations (b) wIce and (c) woIce; the contour interval for the OLR is 20 W/m^2. Precipitation over high terrain (the Himalayan mountains) is removed.

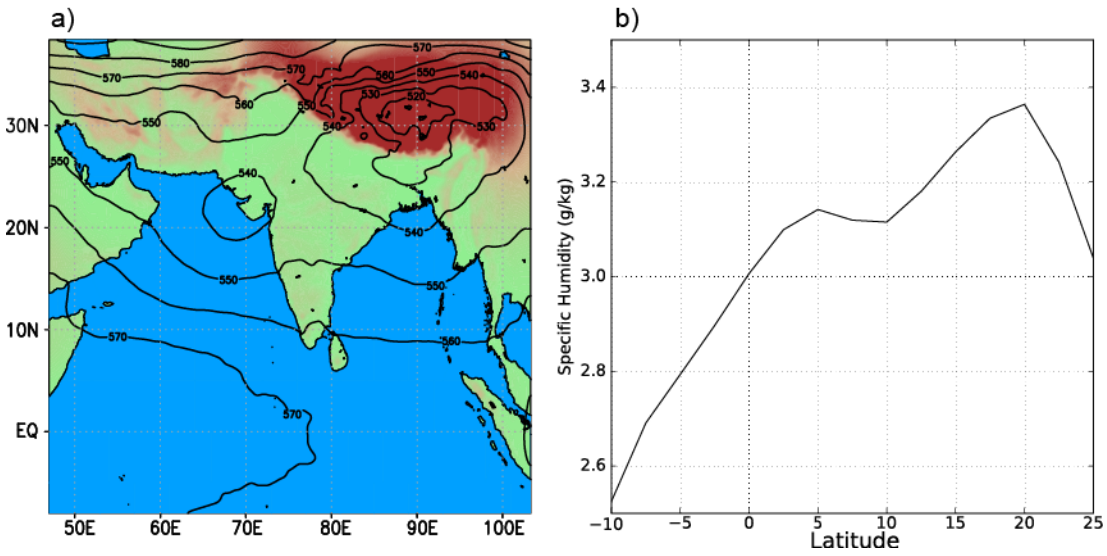

Figure 9. (a) JJAS mean height of the freezing level (0°C) in pressure (hPa) from the 5 wIce simulations. (b) Zonally averaged (50°E - 100°E) 500 - 600hPa mean specific humidity (g/kg) during JJAS for the years 2000-2007 in R2 reanalysis

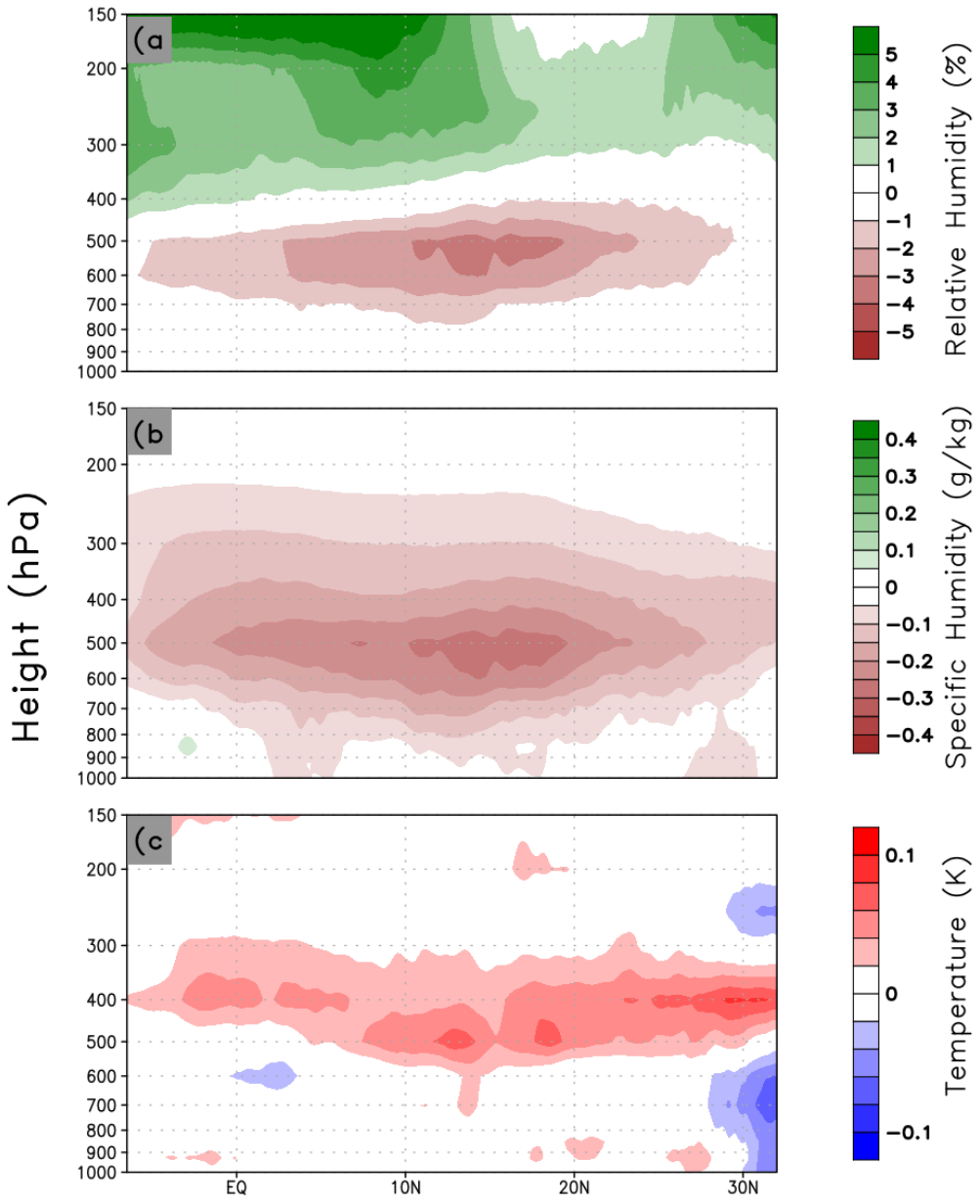

Figure 10. Zonally averaged (50ºE - 100ºE) cross-section of (a) relative humidity (%),(b) specific humidity (g/kg) and (c) temperature (K) difference relative to woIce (wIce-woIce) averaged over all model years during JJAS. Temperature contour interval is 0.02 ºC

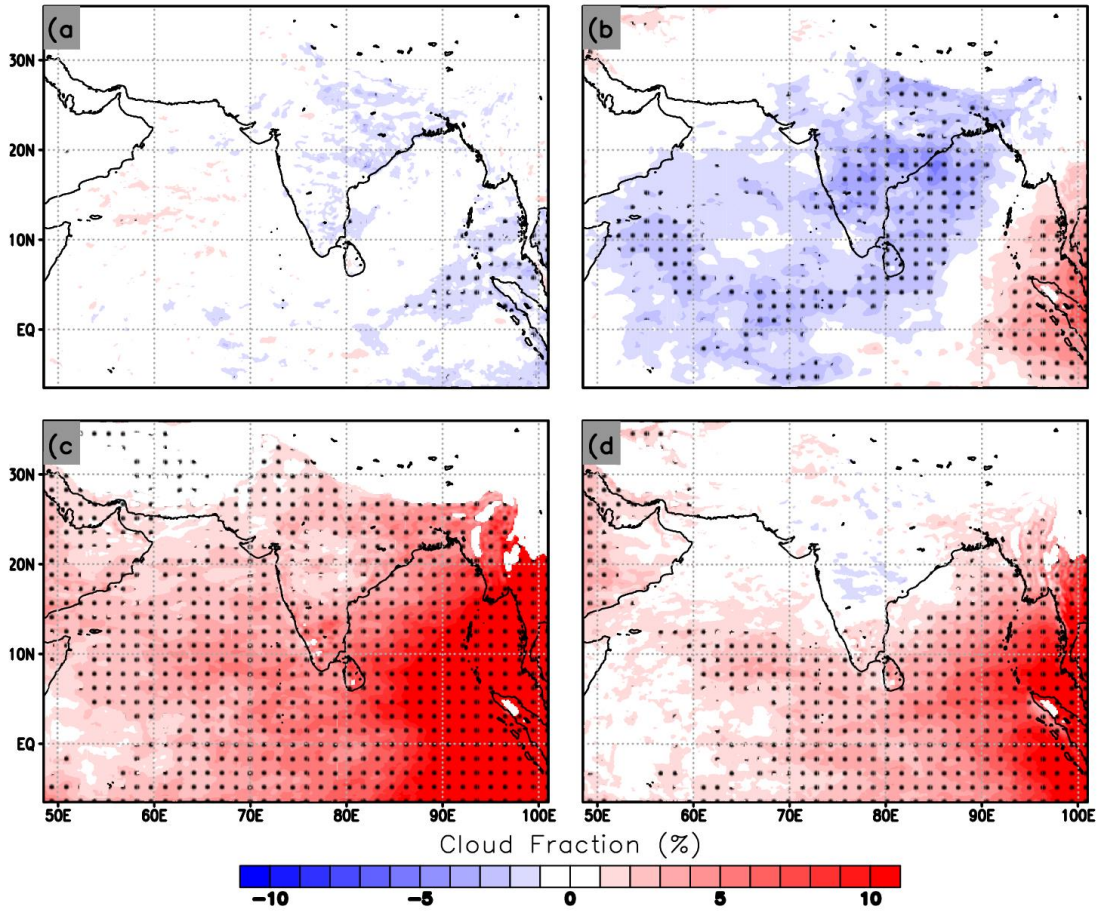

Figure 11. Shaded (a) low, (b) middle, (c) high and (d) total cloud fraction (%) difference relative to woIce (wIce-woIce) averaged over all model years during JJAS. Red indicates an increase in cloud fraction over JJAS, whereas blue indicates a decrease. Statistically significant values at the 90% confidence interval are dotted. Data over high terrain is not shown.

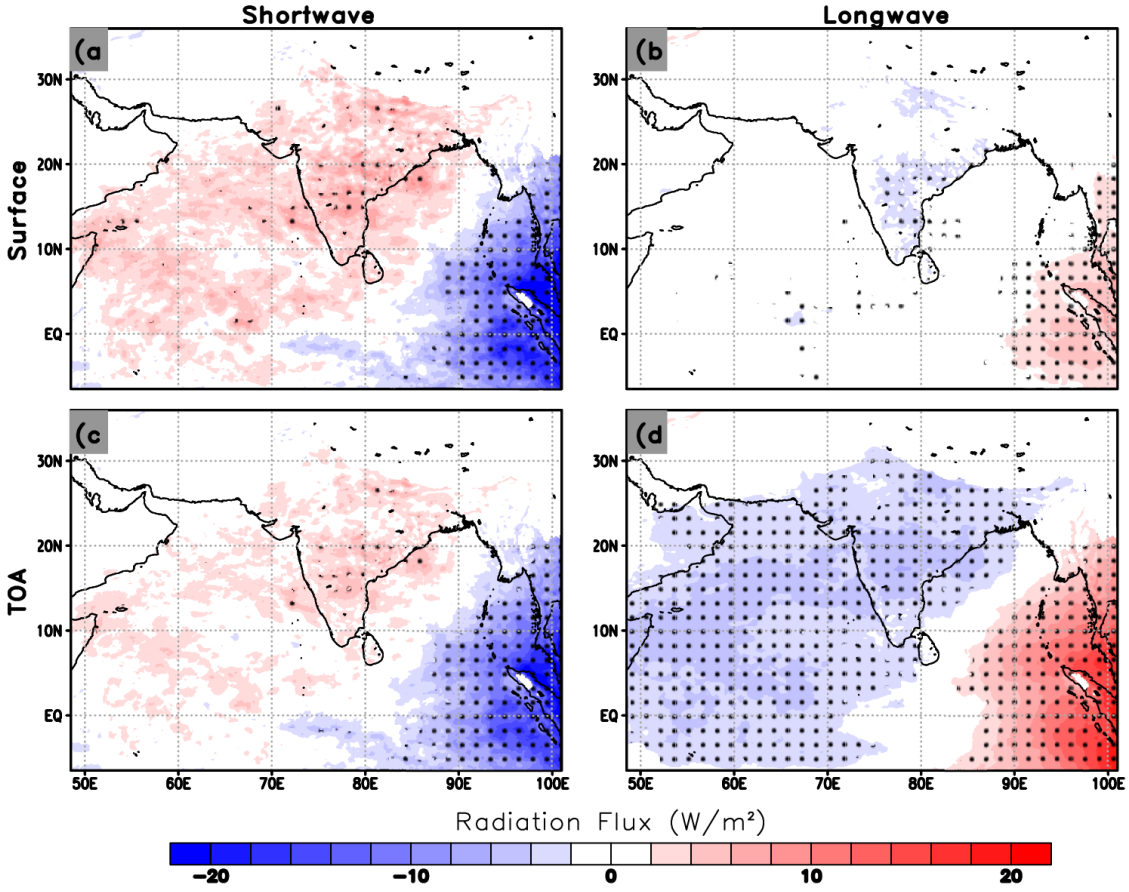

Figure 12. Model mean JJAS difference (wIce-woIce) for (a) shortwave radiation flux at the surface and (c) top of the atmosphere (W/m^{-2}) and (b) the longwave radiation flux at the surface and (d) top of the atmosphere (W/m^{-2}). Here positive values indicate that the change in flux is downwards (gain) and negative values indicate that the change in flux is upward (loss). The calculation of the flux before differencing is also done with the same convention: upwards is negative (loss), downwards is positive (gain). Statistically significant values at the 90% confidence interval are dotted.

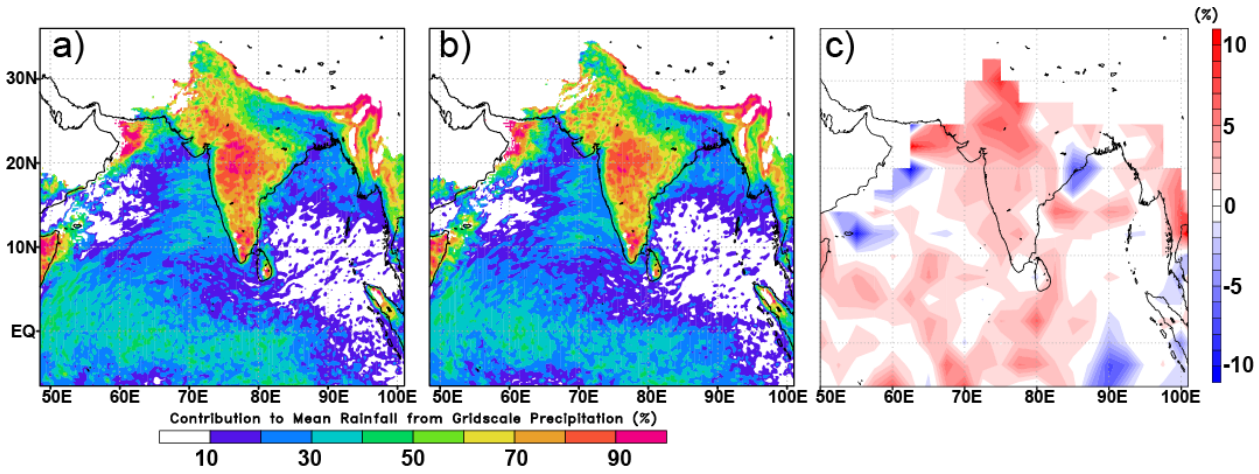

Figure 13. The contribution to the total mean JJAS rainfall from grid-scale precipitation (%) in the (a) wIce and (b) woIce simulations. (c) The difference in grid-scale precipitation contribution between (a) and (b) (wIce-woIce). The difference field was interpolated using area average with latitude weighting down to a 2.5^{o} x 2.5^{o} grid.

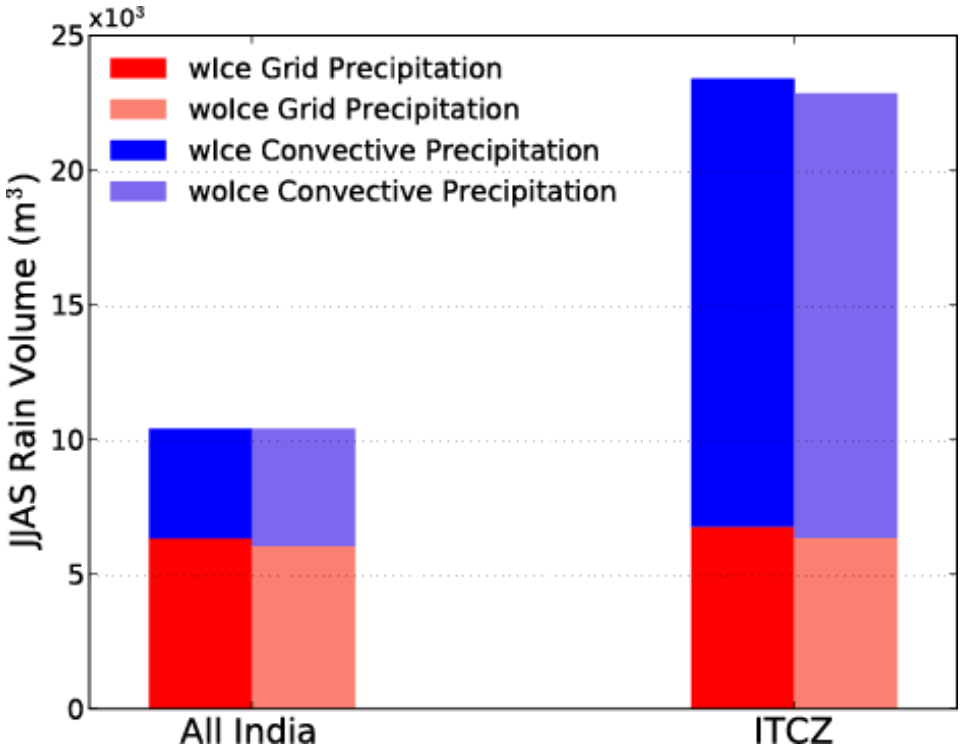

Figure 14. The total amount of rainfall, delineated by the convective and grid-scale rain components, during the JJAS period measured in cubic meters of water ($x10^3$) over all India (land) and the ITCZ (defined here as 5°N to 5°S and 65°E to 95° E). Blue shading indicates the convective precipitation rain volume mean from the wIce simulations and the light blue shading indicates the same but from the woIce simulations. Red shading indicates the grid-scale precipitation rain volume mean from the wIce simulations and the light red indicates the same but from the woIce simulations. The total amount of rainfall equals the convective plus the grid-scale rainfall components.

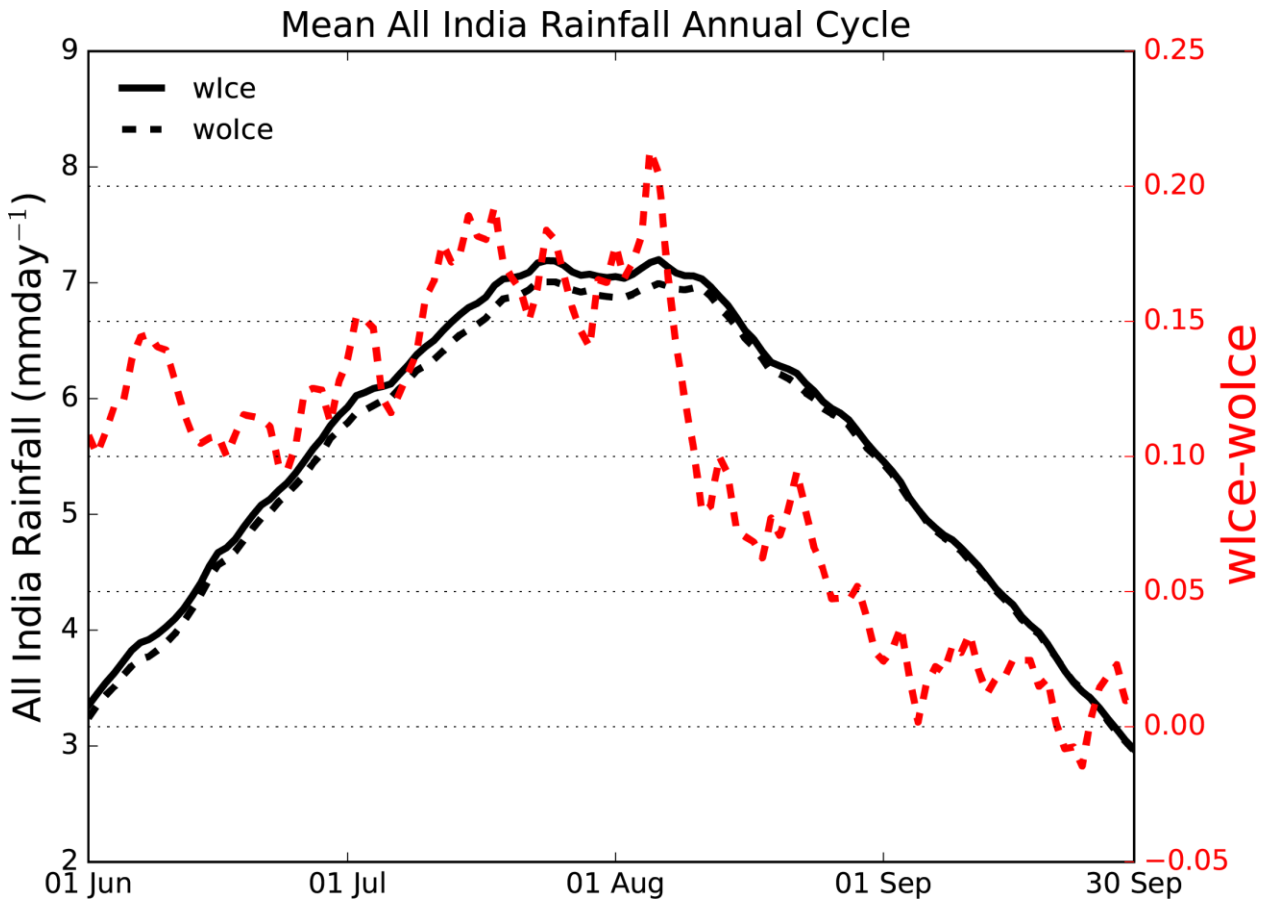

Figure 15. The 30-day running mean daily rainfall averaged over All India during the summer monsoon in the wIce (solid black line) and woIce (dashed black line) multiyear simulations. The difference between the wIce and woIce rainfall seasonal cycle is shown with the dashed red line.

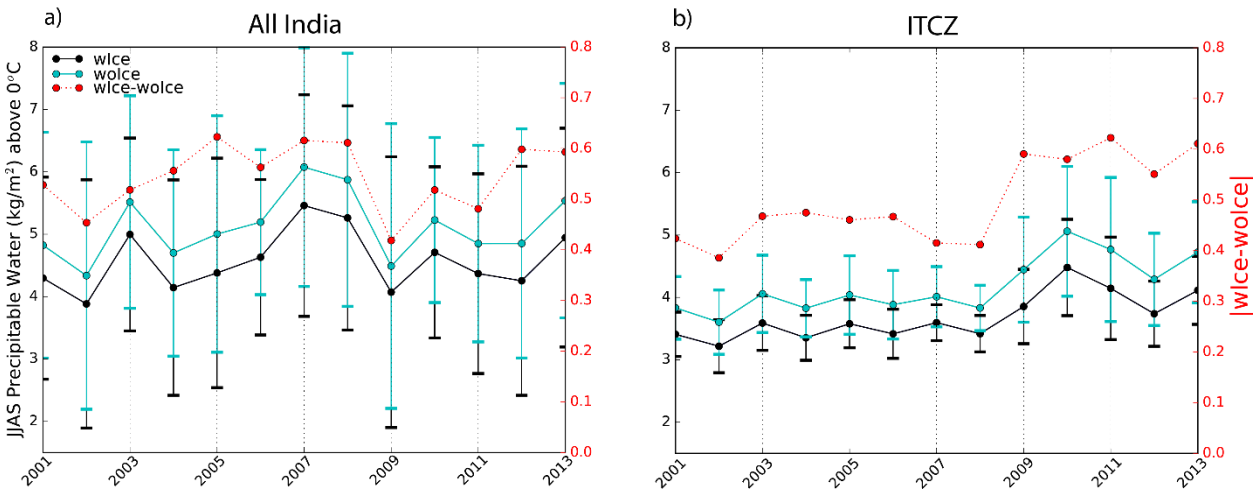

Figure 16. The mean JJAS precipitable water found above the freezing level in the wIce and woIce multiyear simulations over All India (a) and the ITCZ (b). The absolute difference in precipitable water between the wIce and woIce simulations is denoted by the dotted red lines for All India and the ITCZ. The solid black lines indicate the wIce multiyear simulation and the cyan lines indicate the woIce multiyear simulation. Error bars indicate the 95% confidence levels in wIce and woIce.

CHAPTER 4

COUPLED MODEL SVP EXPERIMENTS

4.1 Motivation for Coupled Experiments

In Chapter 3 the uncoupled model experiments showed us that allowing the SVP to be over ice above the freezing level results in increased mean seasonal grid-scale condensation of water vapor relative to the woIce run. This increases the grid-scale rain production and accordingly an increase in mean seasonal rainfall is noted in the wIce runs. The process of condensing a larger amount of water vapor above the freezing level dries the mid and upper-troposphere and we noted a decrease in specific humidity and relative humidity (RH; although an increase in RH is found in the upper-troposphere) in the wIce runs. Because the cloud amount is directly tied to the relative humidity in a grid cell in the model, this drying of the middle troposphere results in decreased middle cloud amount. This decrease of the middle clouds increases the amount of solar radiation flux at the surface and contributes to a positive net heat flux going into the Arabian Sea (AS) in the wIce simulation. In the eastern equatorial Indian Ocean (EEIO) near Sumatra, increased middle and high clouds contribute to less solar radiation at the surface and a negative net heat flux (see Fig. 20a). Because these uncoupled model experiments used prescribed SSTs, the Indian Ocean in this case is not able to respond to the changes in the net heat flux that result from the SVP experiment. It is possible then that, in relation to the atmosphere-only SVP simulations of Chapter 3, there are climate sensitivities and impacts from the calculation of SVP that are not captured from uncoupled experiments. It was then proposed that a repeat of the SVP experiments be conducted with an interactive ocean component so that the ocean and atmosphere can exchange fluxes through the model integration period. The results from these experiments are compiled in this chapter. Assuming that the

atmosphere responds in a similar way to the uncoupled experiments, the ocean will now respond to the changes to the net heat fluxes resulting from the changes to SVP. A positive net flux into the AS will allow the SST and upper ocean to warm, while a negative net flux in the EEIO will cool the SSTs there. Given that the ISM is very sensitive to SST changes in these regions and that it already exhibits SST dipole variability on interannual timescales, we would speculate that the ISM intraseasonal and interannual variability will be impacted far greater than in the uncoupled simulations. The addition of full air-sea coupling will allow the variability of the monsoon to be affected through the ocean and we estimate that this will induce larger variability into the ISM than what the atmosphere alone would induce, as in the uncoupled simulations.

4.2 Moisture and Thermodynamics

To begin, we will first examine the atmospheric response to SVP changes in the coupled simulations. Like Fig. 10 of the uncoupled simulations, Fig. 17 shows the zonal mean JJAS difference in moisture and temperature between wIce, woIce and MIX. As in the uncoupled simulations, the differences are taken relative to the woIce run. Notice first the similarities between Fig. 10 and Fig. 17: indicated drying of the mid and upper-troposphere with respect to the amount of water vapor. The RH changes again indicate relative moistening of the upper-troposphere due to the small amount vapor left at these levels resulting in a larger relative humidity change from SVP over water to SVP over ice. Interestingly the amount of drying in wIce relative to woIce is slightly reduced compared to Fig. 10 of the uncoupled runs. This is a point which we will revisit throughout the chapter. Another important point here is that the MIX run is behaving similarly to wIce as before but that the amount of drying appears to have reduced further. This should be expected considering that the MIX run is allowing SVP over water

partially throughout the middle troposphere and thus we should expect the difference to be closer to woIce. However, the upper-level RH increase is essentially identical and despite there being decreased drying in the mid-troposphere the MIX run is still showing significant drying there. The temperature response in Fig. 17e and 1f is again indicating warming in the mid-troposphere like Fig. 10. Interestingly we see that in the MIX simulation the warming is reduced compared to wIce. It is possible that this is the result of relatively less condensation occurring in the MIX simulation compared to wIce because of the fact that the SVP will not be exactly over ice but slightly increased in the mid-troposphere from the contribution of SVP over liquid water.

From Fig. 17 we see that the mean atmospheric response to the SVP changes in the coupled model simulations, similar to the uncoupled simulations, is to increase condensation of liquid water when SVP over ice is allowed above the freezing level. The resulting increase in condensation removes water vapor from the column resulting in drying above the freezing level. Like the uncoupled simulations, associated with this drying we noted an increase in grid-scale seasonal rainfall in the wIce and MIX simulations (not shown).

4.3 Clouds and Radiation

As we saw in Chapter 3 with the uncoupled simulations, changes to the RH throughout the column in the wIce simulations impacts the cloud layer amounts relative to the woIce run. Because of the similarities between Fig. 10 and Fig. 17 we would expect the cloud layer amounts to respond similarly in the wIce and MIX coupled simulations. In Fig. 18 we see that indeed the coupled wIce and MIX cloud layer amount differences are nearly the same as in the uncoupled simulations (see Fig. 11). The middle cloud layer amount is reduced across most of India and the AS while the cloud amount over the EEIO increases in the middle and upper levels in the wIce

and MIX run. High clouds on the other hand are increased significantly across the Indian Ocean in agreement with the increase in RH there. The spatial patterns of the cloud amount changes are very similar between Fig. 11 and Fig. 18 and between wIce and MIX in Fig. 18, however we will highlight a few observations which we believe are significant. In addition, it is noted that the regions which contain differences that satisfy 90% confidence appear to be larger in the coupled runs (Fig. 18) compared with the uncoupled runs (Fig. 11). This may be an indication that the variance in the daily cloud amount in the coupled simulations is smaller than in the uncoupled simulations, which would allow smaller differences in the coupled simulation between wIce and woIce to satisfy the 90% confidence level. Lastly, in comparing the differences in the middle cloud amount between Fig. 11b and Fig. 18b we see that in the coupled runs the magnitude of the differences between wIce and woIce is reduced. Thus, similar to what was found in the moisture and thermodynamic variables, we find that the cloud amount changes as a result of SVP seem to be reduced with a coupled simulation.

As was pointed out in Section 3.3 any changes to the middle cloud amount will have a greater impact on the radiation flux than changes to the high clouds because the middle clouds are parameterized to have a larger optical depth than high clouds. Middle clouds are assumed to be thicker stratiform cumulus clouds whereas high clouds are thinner cirrus type. Therefore, over the AS where there is a decrease in middle clouds we find in Fig. 19 that there is an increase in shortwave radiation (SW) coming to the surface and at TOA, while over the EEIO it is reduced. This is directly related to the changes in the middle clouds. The changes to the terrestrial longwave radiation has an opposite sign to the changes in the SW radiation. The MIX simulation (Fig. 19e-h) generally has weaker changes to the radiation fluxes compared to the wIce simulation. Consistent with Fig. 17 and Fig. 18 when comparing to the uncoupled simulations

(Fig. 12), the changes to the radiation flux in the coupled model between wIce and woIce (and MIX and woIce) are reduced. Thus, we are beginning to see that the coupled simulations appear to have more climate stability, not less, in response to changes in SVP compared to the uncoupled simulations.

4.4 Net Heat Flux

In the uncoupled simulations the implication of increased (decreased) SW radiation at the surface over the AS (EEIO) is that this leads to increased (decreased) Net Heat Flux (NHF) at the surface (Fig. 20a). In the absence of coupling these changes to the heat flux are not transferred to the ocean and it is possible that there is upper ocean heat variability that we are not resolving with the uncoupled simulations. Of additional concern is the potential feedback of SST and upper ocean heating and cooling to the atmosphere and its effect on the ISM, which is not captured.

Over the AS in Fig. 20a the seasonal added NHF during JJAS in the wIce run is around 2-3 W/m^2. One question that arises then is, how much will the ocean warm in response to the added heating and should we expect significant realized warming of the SSTs given the magnitude of the changes to the NHF? We can estimate the heating rate or time tendency of the temperature in a 1 meter thick ocean surface layer over a model grid cell and assume that ocean processes such as upwelling and advection are small or,

$$\frac{dT_m}{dt} = \frac{Q_{net}}{\rho_w C_{pw} h_m} \tag{7}$$

where Q_{net} is the total NHF (precipitation flux is ignored), ρ_w is the density of sea water, C_{pw} is the specific heat of liquid water, h_m is the depth of the surface layer where the heating is

absorbed, and T_m is the average temperature of the surface layer. In this case we use a value of 1030 kg/m^3 for the density of sea water and the C_{pw} is 3850 J/Kg^{o}C. If we assume that 90% of the incoming NHF is absorbed in this 1 meter surface layer and Q_{net} is between 2-3 W/m^2 the heating rate over the AS would be 0.06 ^{o}C/day or about 8^{o}C integrated heating over the whole June-September monsoon season. For the EEIO a similar magnitude cooling could be assumed there from Fig. 20a. This amount of heating is enormous but assumes that 1) the coupled model has a realistic and perfect SST-NHF relationship and 2) that no oceanic process or diffusion occur to reduce the heating at the surface. Still, even if a large amount of the heating is dissipated through the full ocean mixed layer, the amount of heating over a monsoon season is significant.

The fact that Fig. 12 and Fig. 19 are showing a very similar radiative flux response in the wIce run, would lead to the expectation that the NHF in the coupled simulation would have a similar pattern like in Fig. 20a. In Fig. 20b however, we see that over the AS the seasonal NHF response in the wIce coupled simulation is significantly different than in the uncoupled simulation. It is difficult to discern what the sign of the mean NHF is in the AS because there appears to be a stationary coastal Kelvin wave which is present during the monsoon season and is resulting in opposing sign NHFs. We believe that the existence of this coastally trapped Kelvin wave is related to discontinuous wind stress along the lateral boundary caused by a small amount of "shock" when the R2 reanalysis moisture and temperature advect into the model domain where the SVP is calculated slightly differently. This is a consequence of the SVP being calculated differently between the model and the lateral boundary conditions (R2). On the other hand, in the EEIO the relative reduction in the NHF in Fig. 20a is much the same in Fig. 20b. It is important to note though that it is possible for warming to be observed in the upper ocean

without a detectible change in the NHF if averaged over a significant period of time as pointed out in Du et al. (2008). We will revisit this point again in this section.

To understand whether there is any upper ocean warming/cooling to the changes in the NHF seen in Fig. 20b, we plotted the JJAS mean SST (Fig. 21a) and ocean mean temperature (OMT; Fig. 21b) for the wIce and woIce coupled simulations averaged over the AS (defined as 55^{o}E-77^{o}E and 5^{o}N-23^{o}N) and the EEIO (defined as 80^{o}E-100^{o}E and 5^{o}N-5^{o}S). The OMT is calculated as the mean temperature of the first five model levels below the surface and the SST. At grid points over the deep ocean the fifth model level is a depth of about 300 meters. The SST over the AS (red solid line) appears to have very little if any warming at all in the wIce run. The OMT also shows very little detectable change in warming between wIce and woIce over the AS. The SST over the EEIO (blue solid line) however, is indicating cooling on the order of 0.1^{o}C in wIce throughout the simulation. The OMT in the EEIO in Fig. 21b on the other hand, is not showing a clear cooling signal. It is important to point out that the area over the EEIO encompasses the equator and thus the thermocline depth can vary quite a lot on an interannual timescale. This is why the OMT over the EEIO shows a large amount of interannual variability in Fig. 21b.

In order to better understand the relationship between the NHF and the upper ocean in the AS and EEIO, we will examine the zonal mean seasonal heat fluxes averaged over the AS and the EEIO in both the coupled and uncoupled wIce and woIce simulations. In Fig. 22a we see that the NHF is increasing at all latitudes in the AS in the wIce uncoupled simulation, but in the coupled simulation it is only increasing at a few latitude bands and it is very difficult to tell whether there is an increase or not in wIce. In the EEIO (Fig. 22b) the NHF is clearly decreasing by about 5 W/m^2 across the equator in both the coupled and uncoupled simulations with the wIce

setup. Clearly over the EEIO there is an indication of cooling at the ocean surface. It is also worth noting that in both regions in the coupled simulation, the NHF has a larger positive component than in the uncoupled simulation. Essentially in the coupled simulation the NHF is higher overall. This is due to the latent heat flux, (LHF; Fig. 24) which in the coupled simulation is less negative (less cooling). This is due to the fact that in a ocean-atmosphere coupled simulation unlike an atmosphere-only simulation, the LHF actually cools the SST and this cooling will decrease the efficiency of the transfer of moisture to the atmosphere, which eventually leads to a decreased LHF.

Over the AS (Fig. 23a), the coupled SW flux difference is smaller than the uncoupled wIce-woIce difference by around 2-3 W/m^2. In addition, the overall seasonal SW flux is smaller in the coupled run than the uncoupled run. It seems possible that the smaller difference in the coupled run is related to the smaller overall flux there. Interestingly, the EEIO in Fig. 23b seems to have the opposite response and the SW radiation is further reduced in the coupled model wIce simulation compared to the uncoupled wIce simulation.

In Fig. 24a over the AS, the LHF wIce-woIce difference is small in both coupled and uncoupled simulations even near the equatorial latitudes where it is only 1-2 W/m^2 difference. In both the coupled and uncoupled simulations, the LHF is increasing in the wIce simulation possibly indicating a warmer SST or that moisture is decreasing near the surface. In the EEIO (Fig. 24b) however the LHF seems more sensitive to the wIce-woIce changes and LHF in the wIce coupled simulation is decreasing by almost 5 W/m^2 over the whole region. We investigated further why the LHF is decreasing by this large amount over the EEIO in the coupled simulation and found it is not due to a change to the wind component but due to an increase in near surface q in the wIce run.

The coupled simulation is decreasing the seasonal SW flux in the AS, and the LHF in the AS and EEIO compared to the uncoupled simulation. The reason for the decreased LHF in the coupled simulation has been discussed. The decreased SW flux at the surface over the AS in the coupled model is a consequence of increased overall cloudiness in the coupled model (not shown) relative to the uncoupled simulation. If it is assumed that the change to SW flux in the AS in the wIce simulation is a function of the mean SW flux, as Fig. 23a suggests, then the realized effect of adding coupling decreases the impact of SVP changes that are made for the simulation. The effect of coupling actually increases the model's ability to adjust to atmospheric forcings such as that imposed by our changes to SVP. This finding has similarities to the "quasi-equilibrium" theory proposed by Du. et al. (2008) to explain why there is no detectible trend in the NHF over the past 50 years over the Indian Ocean despite significant SST warming. In our simulations the NHF over the EEIO does indicate cooling and we find a slightly decreased SST there, however there is no long-term trend.

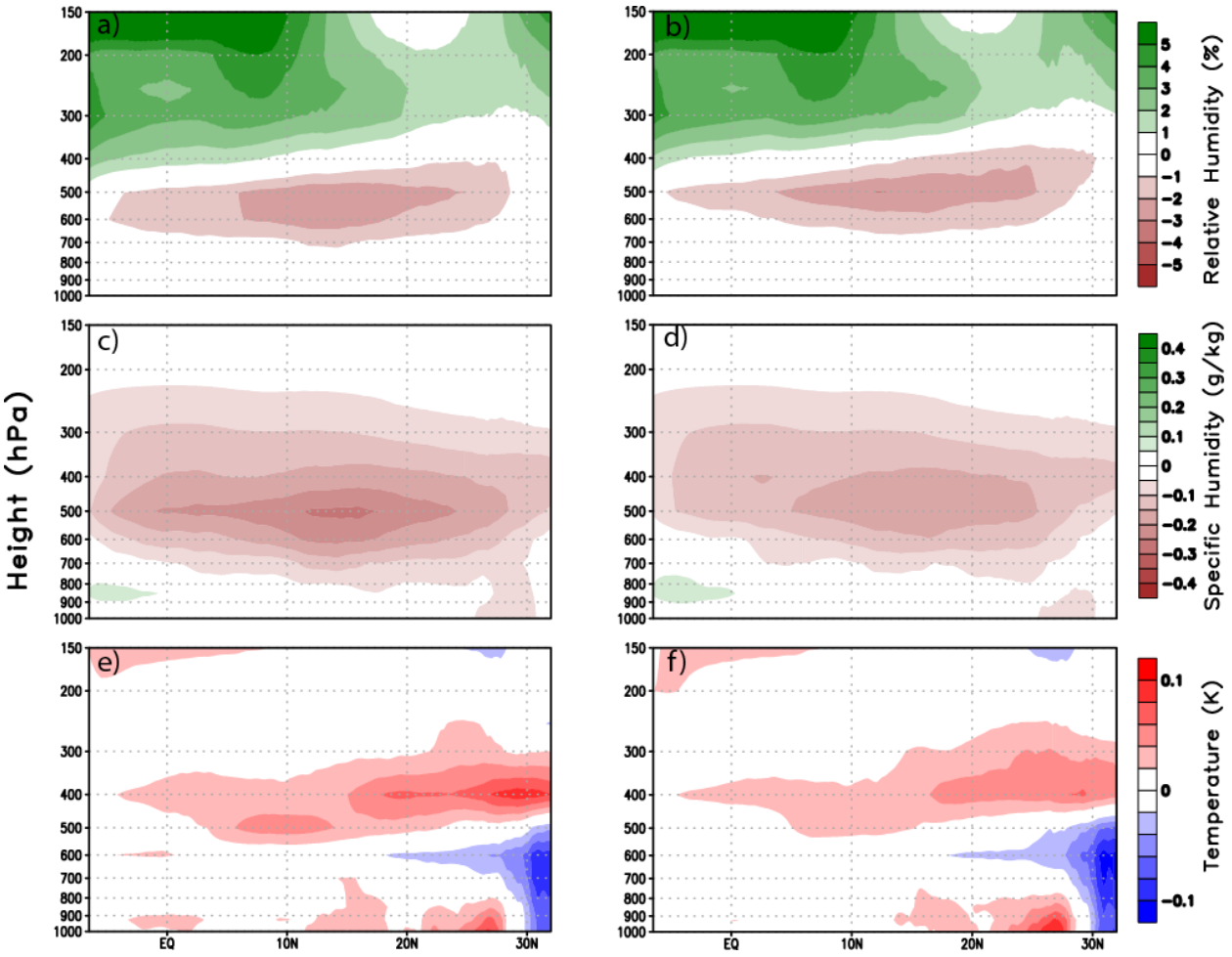

Figure 17. As in Fig. 10 but in the coupled model simulations. The differences relative to woIce in the wIce simulation are a), c) and e). The differences relative to woIce in the MIX simulation are b), d) and f).

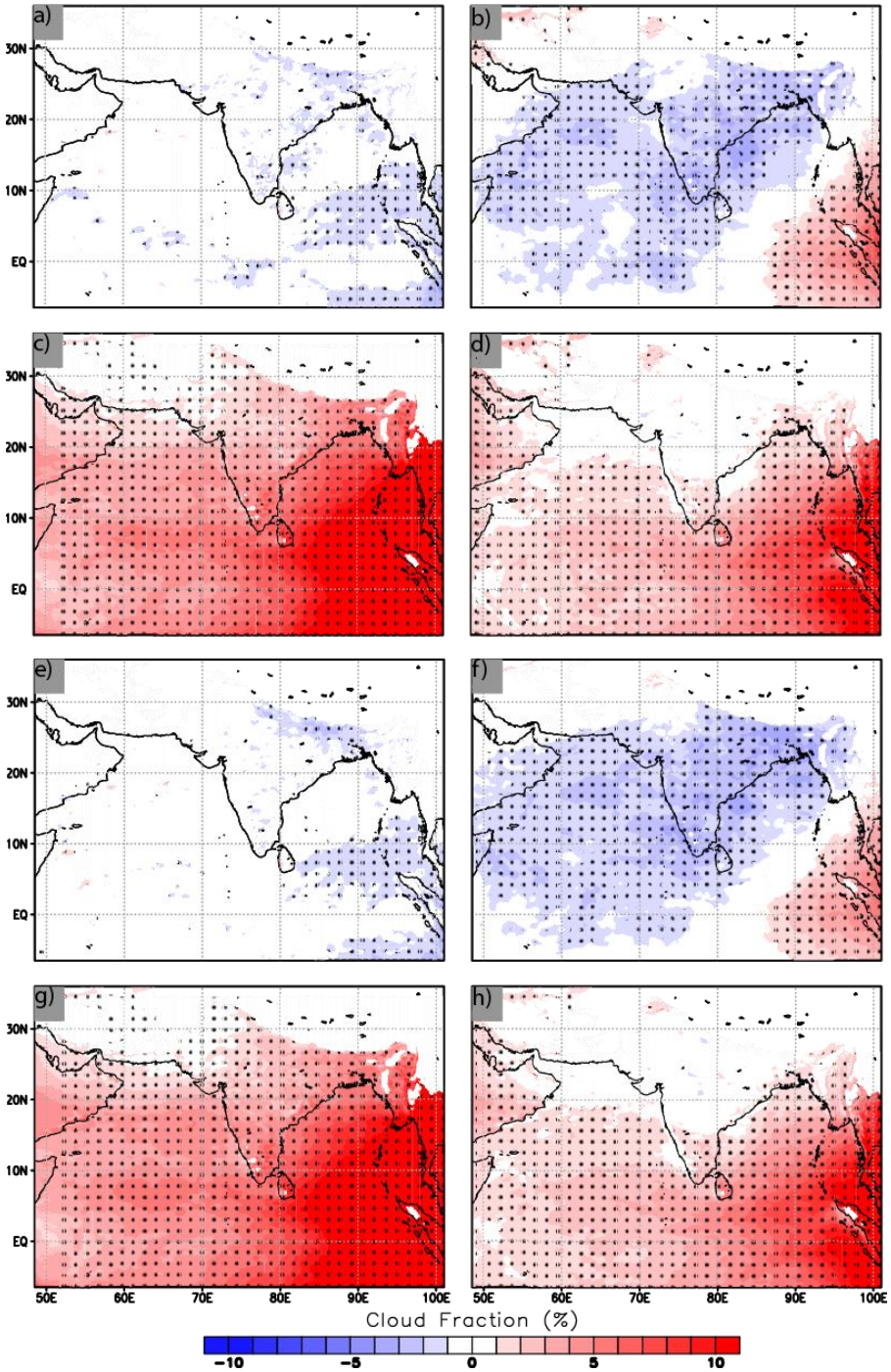

Figure 18. As in Fig. 11 but for the coupled simulations. The cloud amount differences relative to woIce in the wIce simulation are Figs. a-d. The differences relative to woIce in the MIX simulation are Figs. e-h.

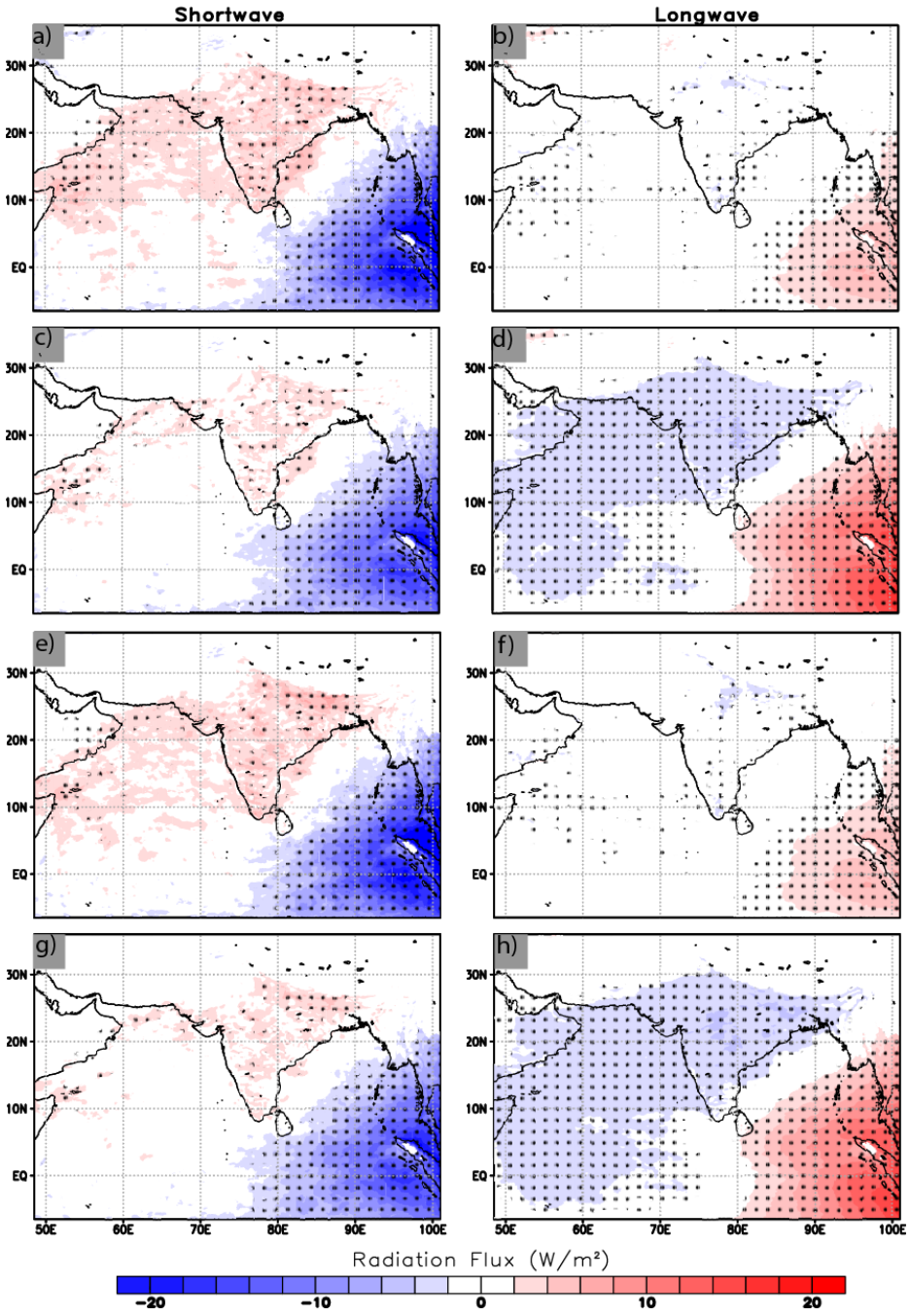

Figure 19. As in Fig. 12 but for the coupled simulations. The radiation flux differences relative to woIce in the wIce simulation are Figs. a-d. The differences relative to woIce in the MIX simulation are Figs. e-h.

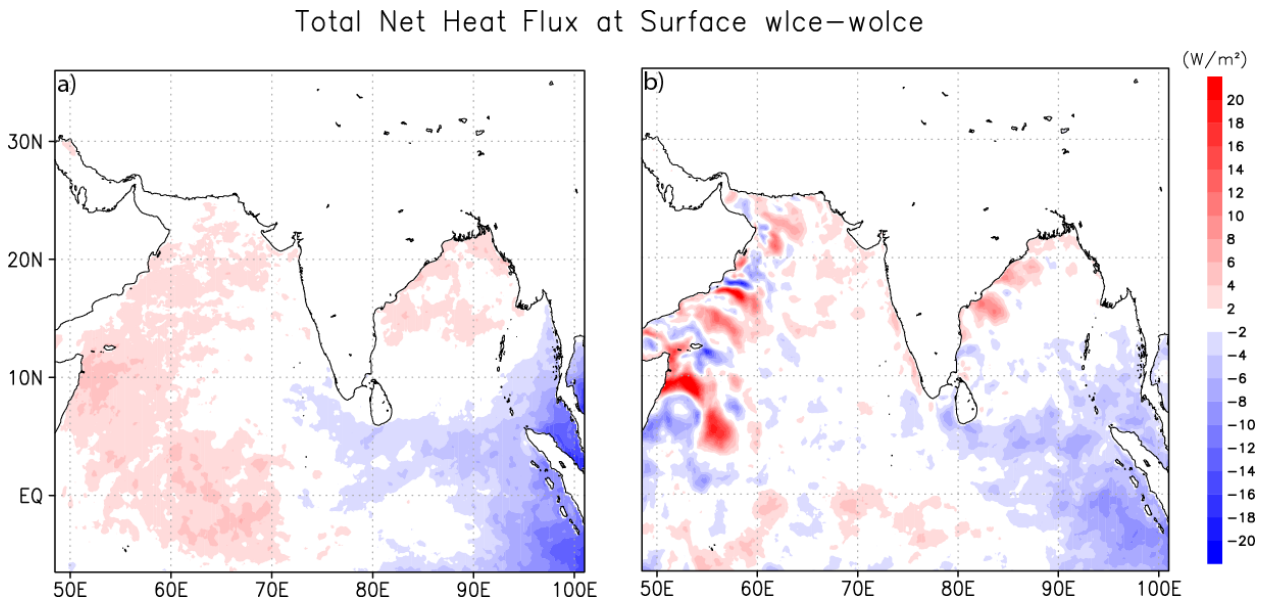

Figure 20. Seasonal mean JJAS total net heat flux change between wIce and woIce relative to woIce in the uncoupled (a) and coupled multiyear simulations (b). Units are W/m^2.

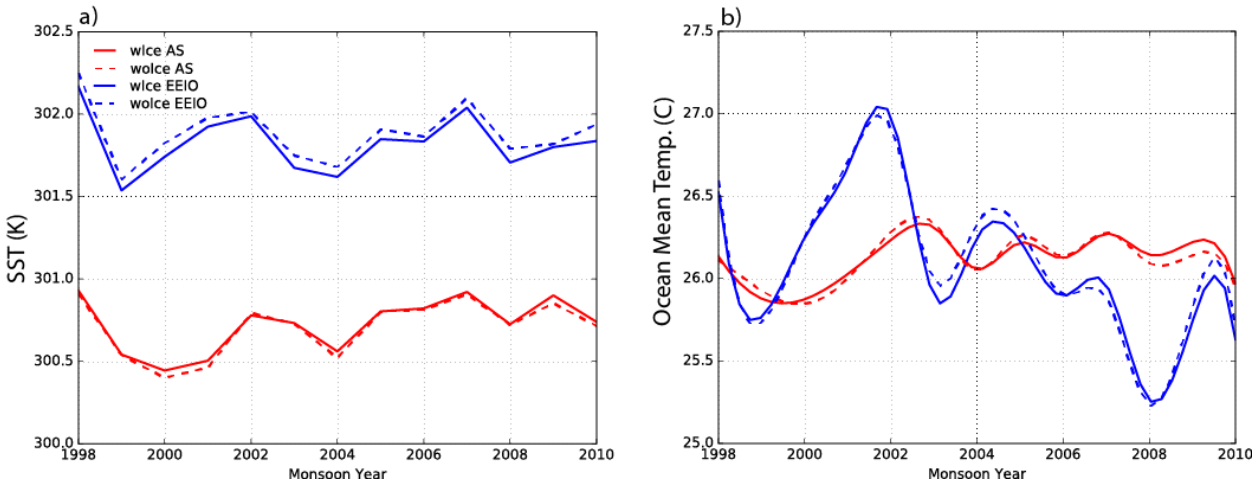

Figure 21. Interannual JJAS mean SST (a) and ocean mean temperature (b) in the AS (red) and EEIO (blue) from the coupled model experiments. Dashed lines indicate the woIce simulation, solid lines indicate the wIce simulation. The ocean mean temperature is the mean of the first five vertical levels below the surface in the ocean and the SST. Units are ^{o}K.

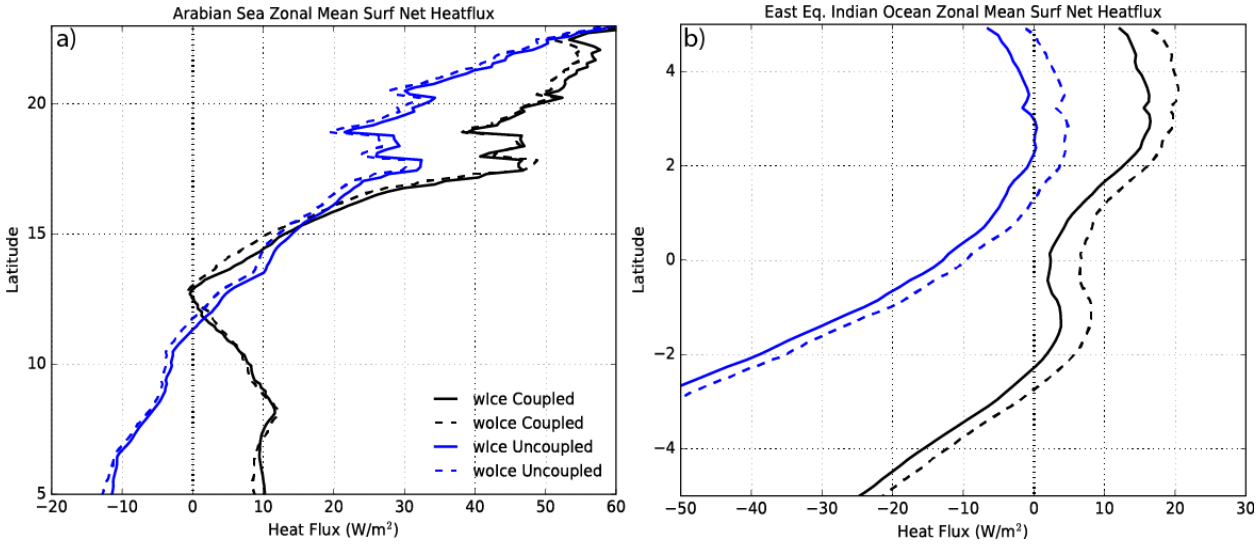

Figure 22. JJAS zonal mean net heat flux in the AS (a) and EEIO (b) from the uncoupled (blue) and coupled (black) multiyear simulations. Dashed lines indicate the woIce simulation and solid lines indicate the wIce simulation. Units are W/m^2.

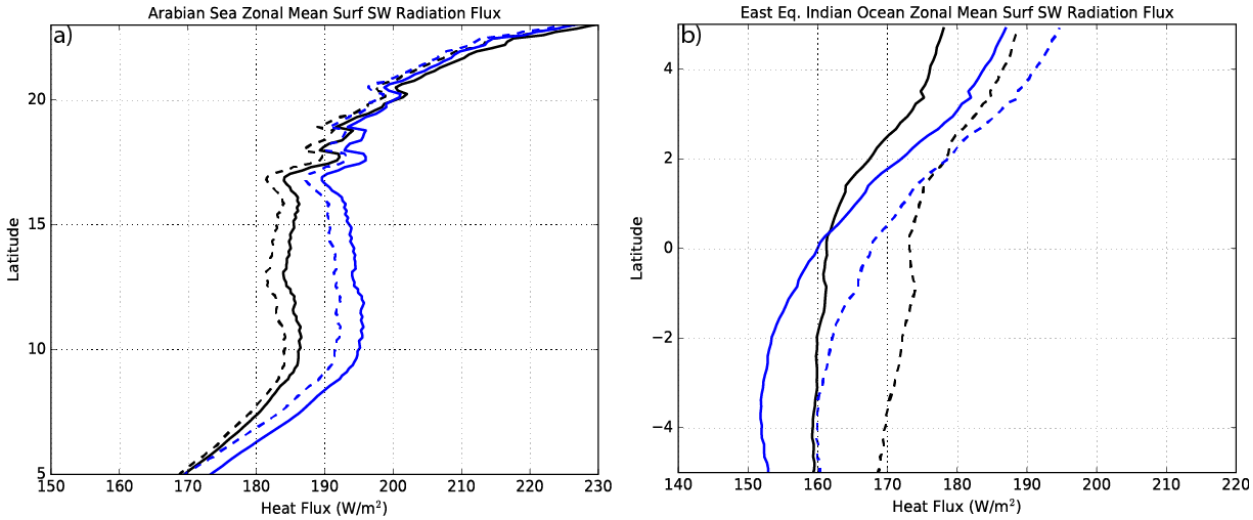

Figure 23. As in Fig. 22 but for the JJAS zonal mean net SW radiation flux at the surface.

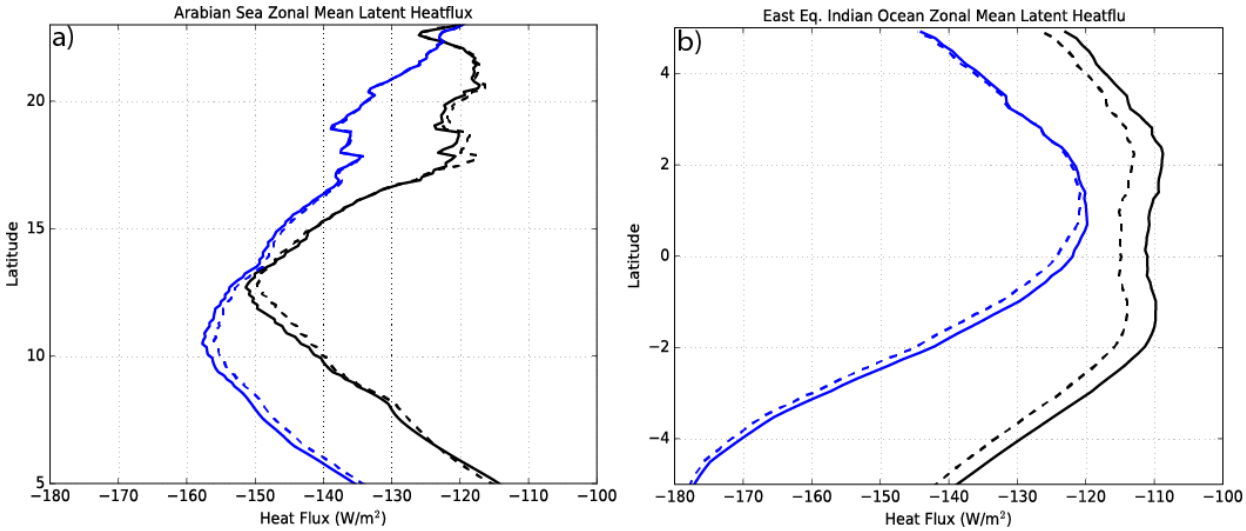

Figure 24. As in Fig. 22 but for the JJAS zonal mean latent heat flux.

CHAPTER 5

THE IMPORTANCE OF AIR-SEA COUPLING FOR INDIAN MONSOON INTRASEASONAL OSCILLATIONS

5.1 The Observed SST-Convective Relationship

Using the coupled and uncoupled simulations conducted with this study we would also like to examine the importance of air-sea interaction for the propagation and maintenance of the ISM intraseasonal oscillation (ISO), which has received a large amount of attention because the majority of the seasonal ISM rainfall is produced during these intraseasonal events (Goswami 1998; Goswami and Ajaya Mohan 2001). Any studies which help improve the understanding of the origin of these intraseasonal events and how they propagate may help improve the forecasting of such events. For this comparison we will use the coupled and uncoupled wIce multiyear simulations. For this analysis the mean evolution of the ISO in each simulation is examined through composites of before and after a peak in the 30-60 day rainfall timeseries. We would like to analyze the extent to which Wind-Evaporation-SST (WES) feedback processes play an important role in the evolution of the ISO in our simulations.

If air-sea interaction and WES feedbacks play an important role in the formation and evolution of the ISO then we should expect that a coupled atmosphere-ocean model would be able to reproduce the observed ISO features better than an atmosphere-only model. Several studies have conducted experiments which test this hypothesis and have found that a coupled model produces a stronger amplitude ISO with a more realistic propagation compared to the same atmosphere-only model (Fu and Wang 2004; Rajendran and Kitoh 2006; Seo et al. 2007). However, several recent studies have also noted that atmosphere-only models have the ability to reproduce the observed ISO features relatively well when the SSTs are prescribed on a short

enough timescale, like for instance a daily timescale (Klingaman et al. 2008; Fu and Wang 2004; Kim et al. 2008).

To establish the observed relationship between convection associated with the ISO and the ocean we will examine ISO rainfall and SST anomalies from two satellite products. Fig. 25 shows the composited zonally averaged (70E-90E) 30-60 day TRMM precipitation anomaly and OI-SST anomaly as a function of lag/lead days relative to the peak in the TRMM rainfall timeseries. At 15 days before the peak date, positive precipitation anomalies are present near the equator and ITCZ in the Indian Ocean, while negative anomalies are present over India at 10N-20N. Forward in time the precipitation anomalies propagate northwards out of the ITCZ and toward the latitudes over India. Also, note that, as described in Lawrence and Webster (2002), a southward propagating component of the ISO in the Southern Hemisphere begins coincident with the northward propagation. Starting about 10 days before the peak, positive SST anomalies begin to appear at the latitudes near India in association with the negative precipitation anomalies located there. These SST anomalies in the Bay of Bengal (BoB) and Arabian Sea (AS) intensify and lead to the onset of several days of heavy rainfall over the India region. Beginning around 5 days after the peak date, negative SST anomalies begin to form in the BoB and AS in association with the increased latent heat flux to the atmosphere and convective cloud suppression of solar radiation to the ocean. Importantly, note that positive SST anomalies lead positive rain anomalies by about 5 days and that negative SST anomalies follow these positive rain anomalies by about 5 days.

5.2 Uncoupled vs. Coupled Comparison

Lag/lead composites of ISO SST and rainfall anomalies are replicated in Fig. 26 but for the coupled (Fig. 26b) and uncoupled (Fig. 26a) simulations. The coupled model ISO rainfall anomalies show greater evidence of northward propagation than the uncoupled simulation, where the rainfall anomalies demonstrate an ISO that is nearly stationary. The coupled model SST and rainfall anomalies show much greater organization and association with one another, with positive SST anomalies leading positive rain anomalies by around 5 days. In the uncoupled model SST anomalies do not seem to have a systematic propagation, and we see different groups of SST anomalies propagating at different speeds. The SST anomalies from the uncoupled simulations do however show northward propagation and in fact the magnitude of the maximum warm SST anomalies prior to the peak is greater in the uncoupled model than the coupled model. One important observation and point of comparison between Fig. 26a and 27b is evolution of the SST and rainfall after the peak. In the uncoupled simulation cold SST anomalies are nearly coincident with the rain anomalies whereas in the coupled simulation the cold anomalies lead the rainfall by around 5 days, consistent with the evolution of the warm anomalies. This is evidence of a lack of interaction between the convection and ocean surface in the uncoupled model, where, according to the WES feedback, the large amount of convection produced by the peak in the ISO suppresses solar radiation while at the same time the monsoon circulation is enhanced in the region, increasing the latent heat fluxes. This should lead to the development of cold SST anomalies in the wake of an ISO peak in the BoB and eastern AS. However, even without this interaction in the wake of the peak, the uncoupled model still is able to simulate a dry spell which follows the peak, indicating some possible internal atmospheric dynamics which drive the ISO.

As in Fig. 26, Fig. 27 shows the composited 30-60 day rainfall anomalies, but they are now plotted with the 850hPa zonal wind anomalies as a function of the lag/lead peak day. These intraseasonal zonal wind anomalies are superimposed upon the mean monsoon westerlies, such that negative zonal wind anomalies indicate a weakening of the mean monsoon circulation and positive zonal wind anomalies indicate a strengthening of the monsoon circulation. In both the coupled (Fig. 27b) and the uncoupled (Fig. 27a) simulations anomalous westerlies are located to the south of enhanced convection, while easterlies follow to the north of the enhanced convection. A couplet of easterlies to the north of westerlies forms a cyclonic circulation which is associated with the location of enhanced convection and rainfall. What distinguishes the coupled simulation from the uncoupled simulation in Fig. 27 is the organization and strength of this anomalous circulation throughout the intraseasonal event. In the coupled model we see greater co-evolution between the anomalous cyclonic circulation and the rainfall anomalies compared to the uncoupled simulation. An important observation lies in the evolution of the rainfall and zonal wind anomalies after the peak date in the uncoupled simulation. Anomalous westerlies are weak after the peak date in the uncoupled model, compared to the strong easterlies present before the peak date. What is illustrated here is that in the uncoupled simulation the forcing to commence a peak is strong as the atmosphere responds to the SST forcing, but after the peak has passed the air-sea interaction that is needed to continue to the next intraseasonal event is weak and therefore after the intraseasonal event or when strong SST forcing is removed, the ISO begins to weaken.

A major part of the WES feedback is the coupling between convective cloudiness and SW radiation to the surface. When convection is at a maximum cloudiness is also at a maximum and SW radiation will be at a minimum at the surface. This acts to cool the SST and create cold

anomalies underneath areas of enhanced convection on a timescale of days. Fig. 28 is showing the composite of the intraseasonal SST and downward shortwave flux (dSWflx) anomalies at the surface in the coupled and uncoupled simulations. Here we clearly see the close association between SST and the dSWflx at the surface in the coupled simulation that is not so clear in the uncoupled simulation. In the coupled model at 15 days before the peak, positive dSWflx anomalies begin to appear in the wake of suppressed convection between 5^{o}N to 15^{o}N. Forward in time these anomalies strengthen and show slow propagation northward such that around 10 days before the peak, warm SST anomalies begin to appear in association with the maximum in dSWflx. As soon as large convective anomalies begin to appear at around 5 days before the peak in Fig. 26b, the dSWflx sign switches in relation to the increase in cloudiness. In the coupled model the SST and dSWflx anomalies have very similar propagation speed and location demonstrating their close relationship while in the uncoupled simulation there is not a robust relationship especially following the peak date. The dSWflx anomalies in the uncoupled model do not show much northward propagation and appear mostly stationary, as reflected in the convective anomalies. Thus, Fig. 28 adds evidence to suggest that anomalies in the ocean and atmosphere propagate together in the coupled simulation while in the uncoupled simulation they only propagate together to the extent that the ocean can force the atmosphere.

The other major component of the NHF at the surface which is modulated by WES feedbacks is the LHF. The effect of the LHF on the atmosphere is to transfer moisture from the ocean to the atmospheric boundary layer, and its effect on the ocean is cool the SST by evaporation. In the coupled simulation both of these effects will be at work while in the uncoupled simulation only the transfer of moisture to the atmosphere will be present. In Fig. 29 we see the close association between the LHF and SST anomalies in the coupled simulation

compared to the uncoupled simulation. Fifteen days before a peak in the coupled model, positive LHF anomalies (indicating energy transfer to the atmosphere) are present just north of the equator at 5^{o}N in association with the northern branch of enhanced convection in the ITCZ, while north of this between 10^{o}N to 15^{o}N, negative LHF anomalies (indicating energy transfer to the ocean) are present in association with the suppressed convection and a weakening of the monsoon westerlies there. At around 5 days before the peak, positive LHF anomalies begin propagating out of the equatorial region in association with the migration of the ISO convection northward. Between 15 and 5 days leading up to the peak the latitudes between 10^{o}N and 20^{o}N are filled with negative LHF anomalies which begin to form SST anomalies in this latitude band around 10 days before the peak. In the coupled simulation, the maximum negative LHF anomaly occurring at around 10 days before the peak coincides 5 days later with the maximum warm SST anomaly at the same latitude. The formation of this maximum in warm SST anomalies also marks the decay of negative LHF anomalies and the beginning of positive LHFs between 15^{o}N and 20^{o}N in association with the peak in convection over India. The uncoupled model generally shows only weak representation of these processes, tending to form stationary dipoles of LHF anomalies that show little evidence of propagation. This is consistent with an atmosphere-only model where the LHF is only modulated by the atmosphere or when a new set of SSTs are prescribed.

If the WES feedback plays an important role in ISO then a coupled model should more closely reflect the observed rainfall and SST patterns associated with ISO compared to an uncoupled model where the WES feedback is very weak. To examine this question, we plot the lag/lead (cross-correlation) correlation between SST and rainfall with SST leading in the uncoupled and coupled simulations and the observed relationship using TRMM and OI-SST data

in Fig. 30. Both the observed and uncoupled simulation have the same peak in correlation at around 6 days because the uncoupled model is using daily OI-SSTs. The coupled model peaks at 5 days with SST leading rainfall but at a correlation much closer to the observed relationship. Therefore, we see that the observed relationship has a robust WES feedback present during ISOs and that a coupled model is able to sufficiently resolve the important WES processes. We conclude that the WES feedback has an important role in modulating and propagating the ISO, however it must also be said that we cannot conclude from this that WES processes are responsible for the origin of ISO signals nor can they be said to be solely responsible for the northward propagation. From our uncoupled simulations, we can see that it is possible to simulate a robust ISO with comparable amplitude to observations without WES processes.

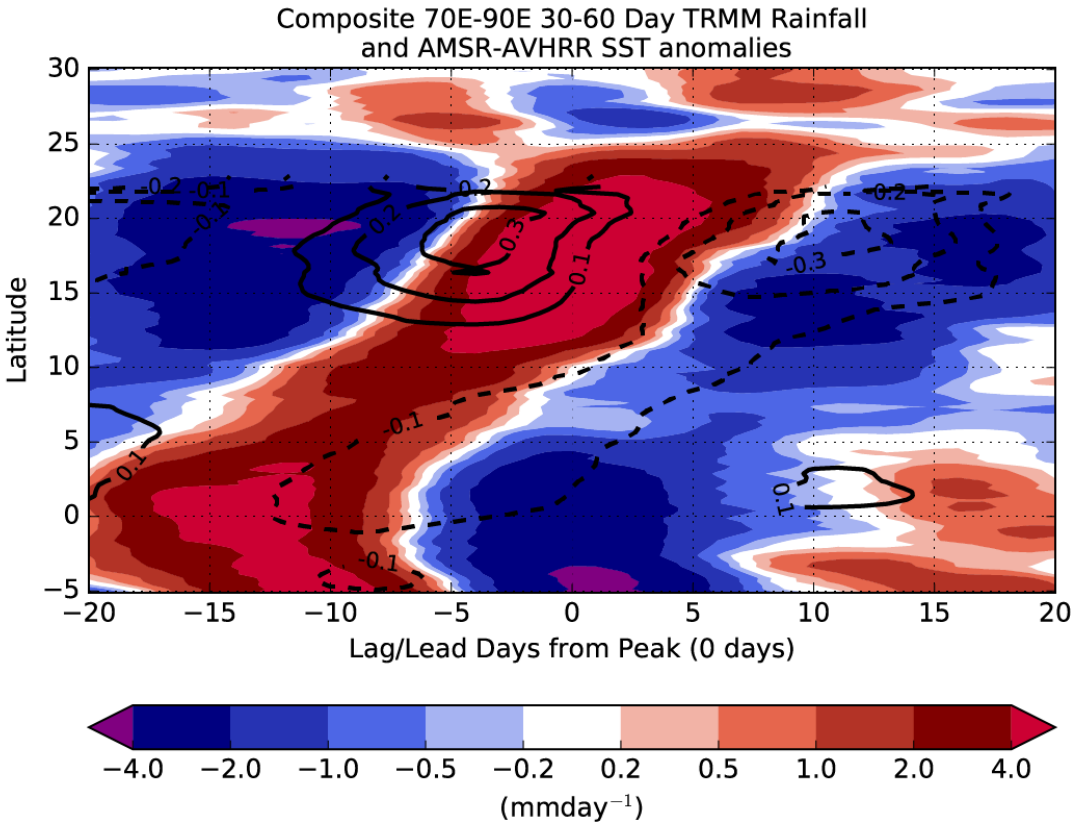

Figure 25. Composited zonal (70E-90E averaged) 30-60 day bandpass filtered TRMM (shaded) and OI-SST (contour) anomalies. The anomalies are plotted as a function of the days before or after a peak date. Negative contours are dashed and indicate cold SST anomalies. The contouring interval of the SST anomalies is 0.1 ^{o}C.

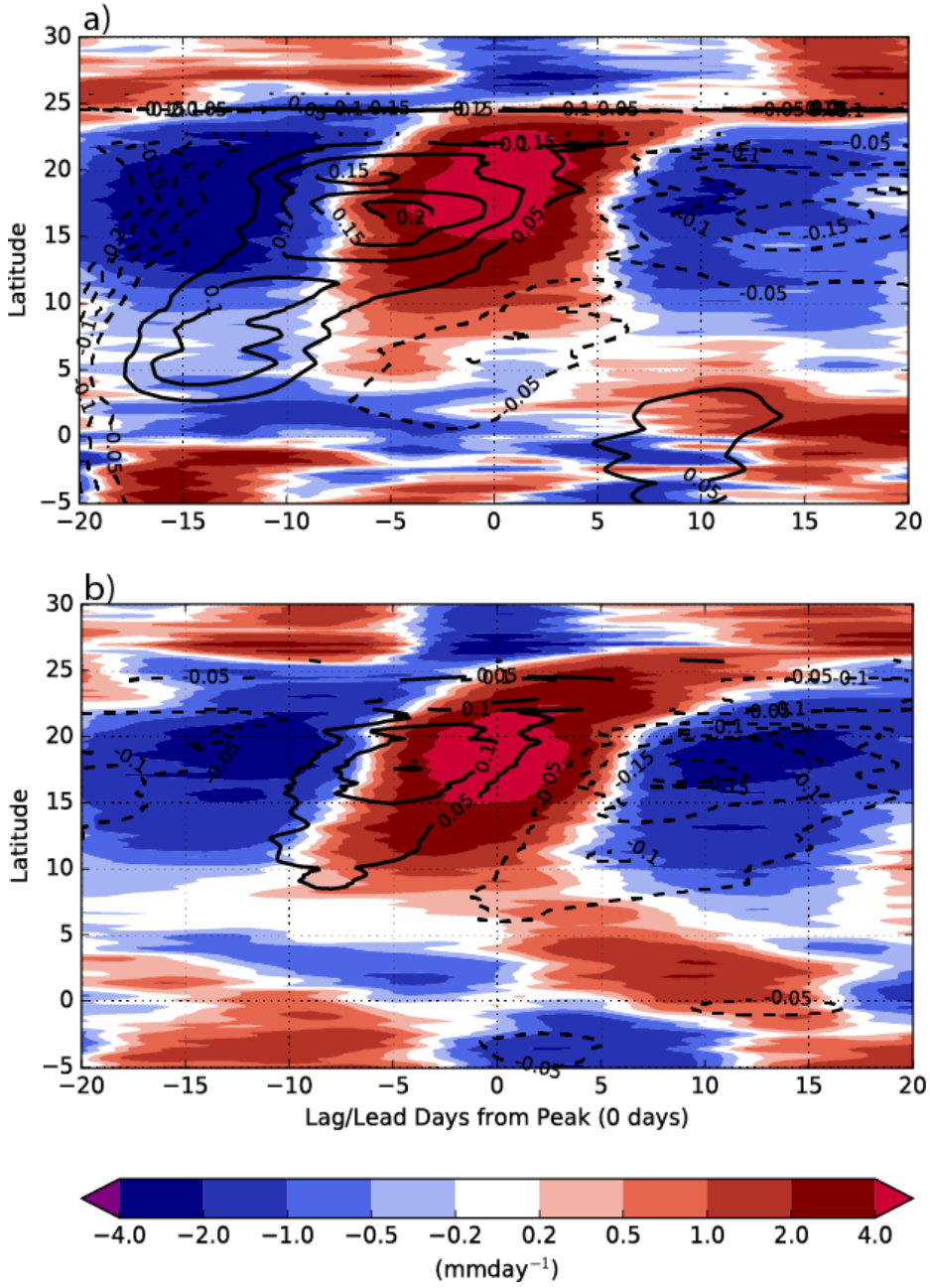

Figure 26. Composited zonal (70E-90E averaged) 30-60 day bandpass filtered rainfall (shaded) and SST (contour) anomalies from the uncoupled (a) and coupled (b) multiyear simulations. The anomalies are plotted as a function of the days before or after a peak date. Negative contours are dashed and indicate cold SST anomalies. The contouring interval of the SST anomalies is 0.05 ^{o}C.

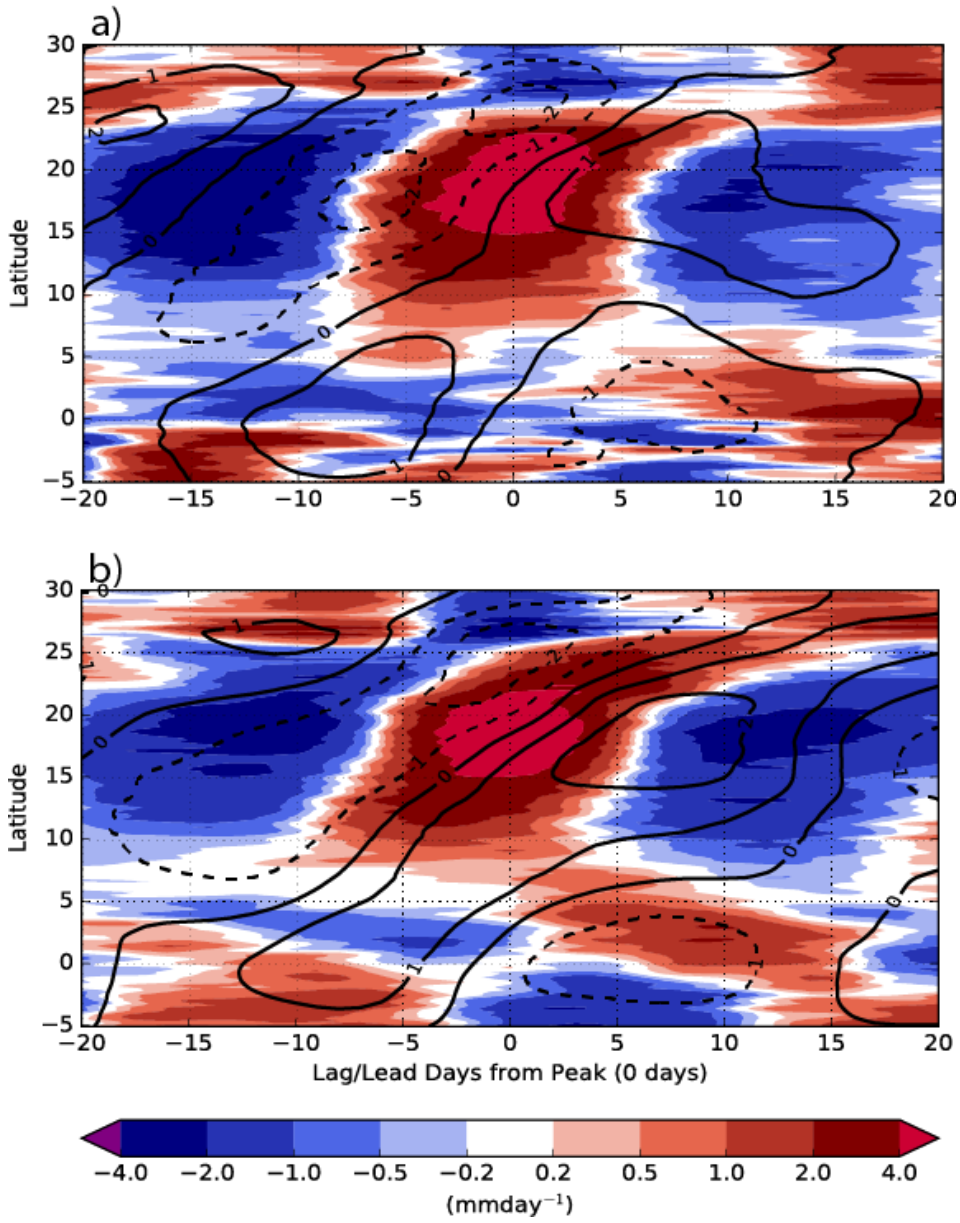

Figure 27. As in Fig. 26 but the contours are now 850hPa U-wind anomalies. The contouring interval of the zonal wind anomalies is 1 m/s. Negative contours are dashed.

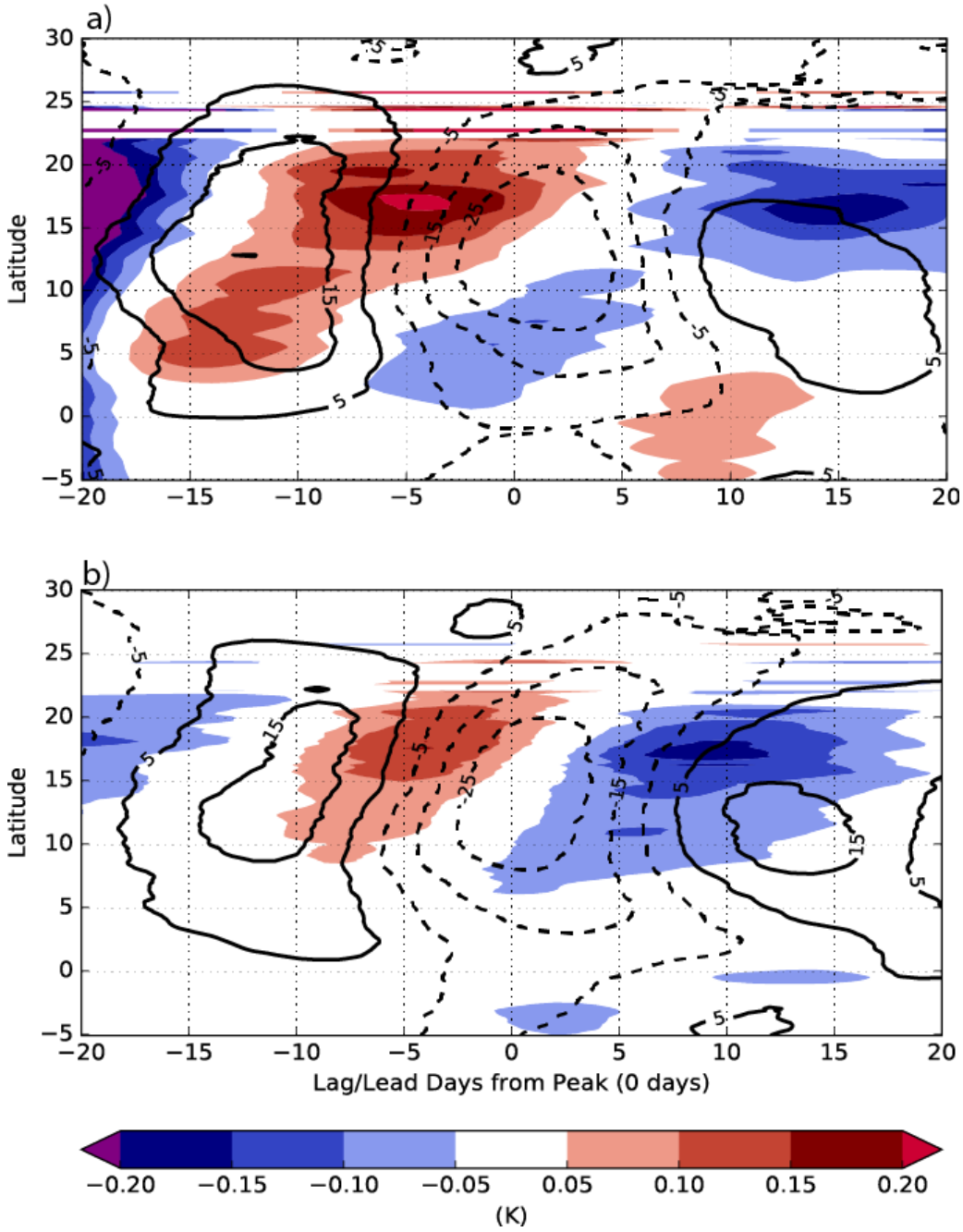

Figure 28. As in Fig. 26 but SST anomalies are now shaded and the contours are downward shortwave flux (dSWflx) anomalies at the surface. Positive dSWflx anomalies indicate more dSWflx going into the ocean and negative anomalies indicate less dSWflx going into the ocean. The contouring interval of the dSWflx anomalies is 5 W/m^2. Negative contours are dashed.

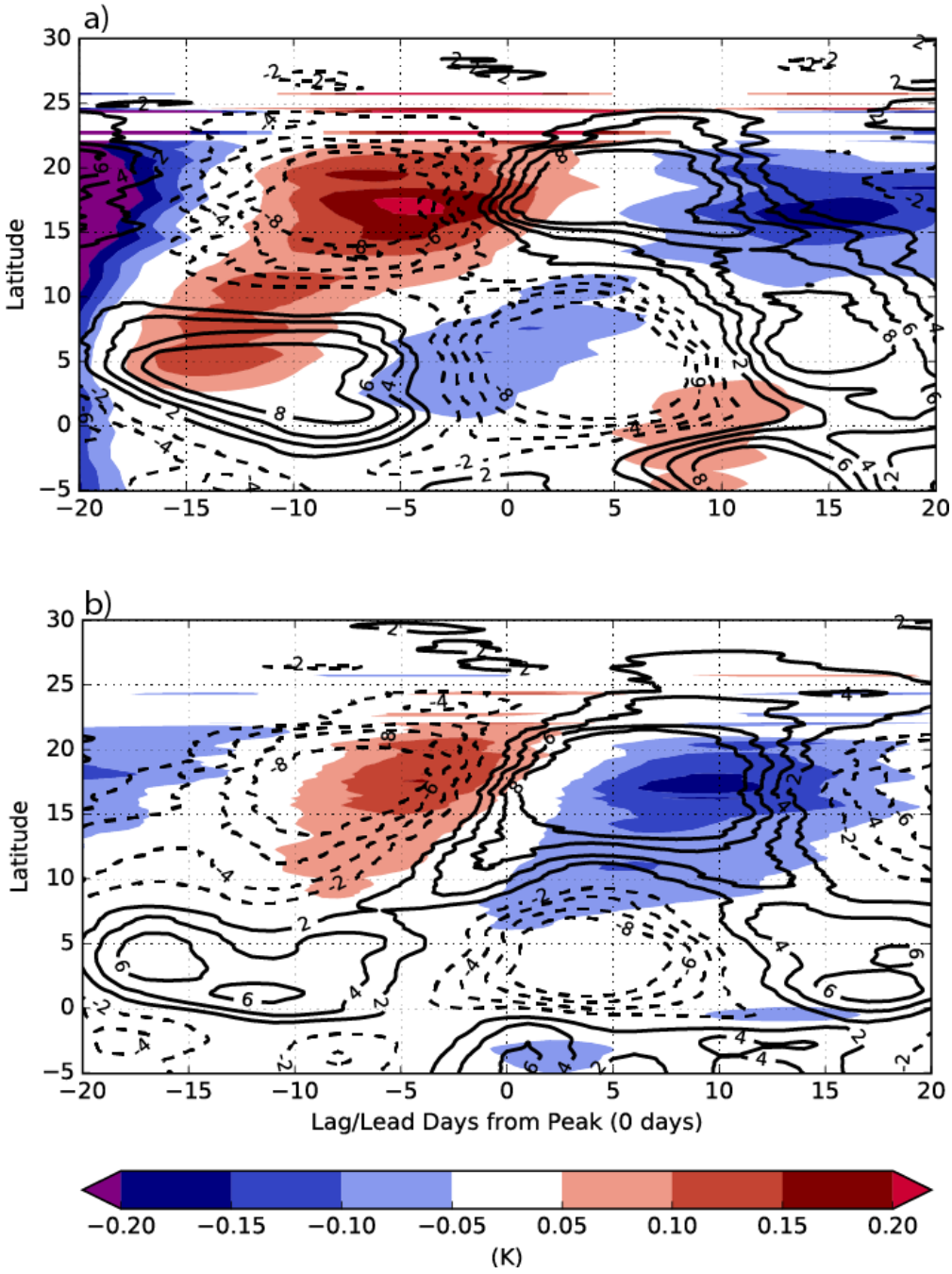

Figure 29. As in Fig. 28 but the contours are now latent heat flux anomalies at the surface. Negative LHF anomalies indicate energy transfer into the ocean from the atmosphere, and positive anomalies indicate energy transfer from the ocean to the atmosphere. The contouring interval of the latent heat flux anomalies is 2 W/m^2. Negative contours are dashed.

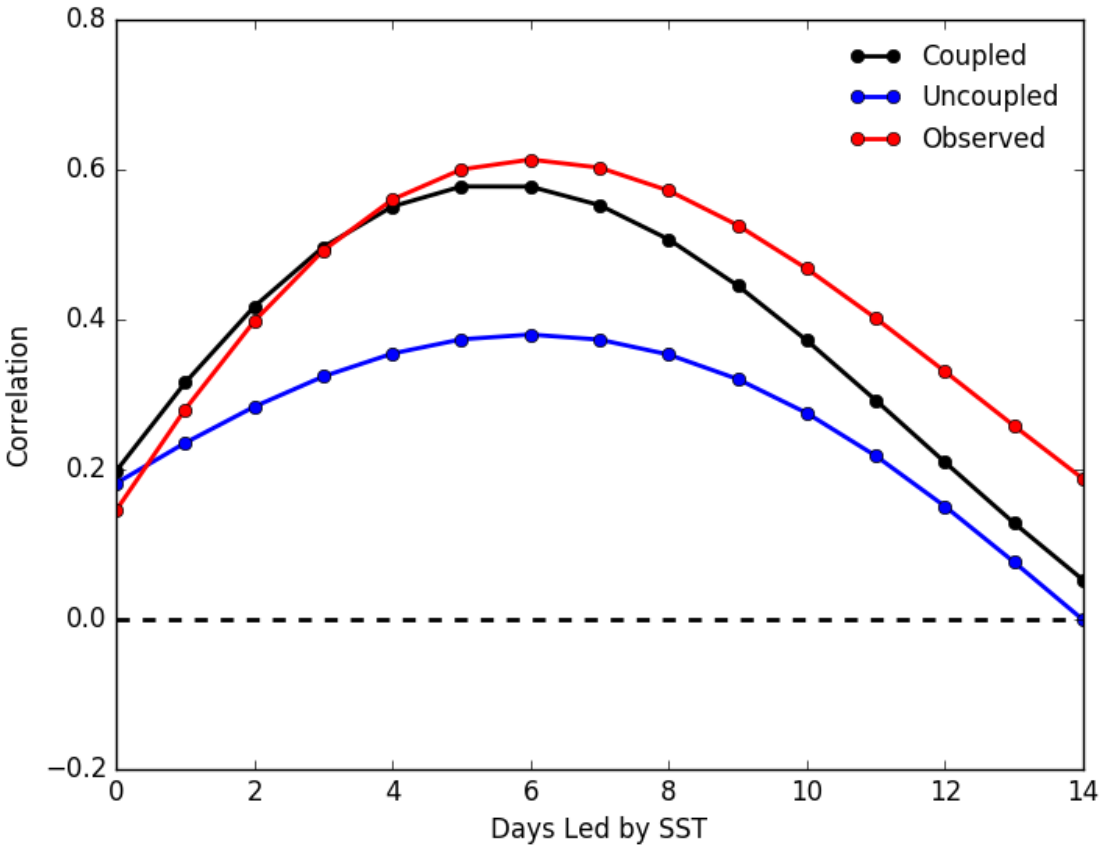

Figure 30. The lag/lead (cross-correlation) correlation between daily 30-60 day filtered SST and rainfall anomalies during JJAS with SST leading rainfall from observations (red line), the coupled simulations (black line), and the uncoupled simulations (blue line).

CHAPTER 6

SUMMARY, CONCLUSIONS, AND FUTURE WORK

6.1 RSM-Only SVP Experiments

In a first set of experiments we examined the potential impact that the treatment of saturation vapor pressure (SVP) has on the Indian summer monsoon (ISM) using seasonal and multiyear simulations of the Regional Spectral Model (RSM). Five monsoon seasons were simulated using the RSM; for each season, one simulation used liquid water saturation throughout (woIce) and one simulation used saturation over ice above the freezing level (wIce). Additionally, a multiyear simulation was conducted for each SVP setup, one wIce and one woIce. This study focused on the sensitivity that SVP has on the seasonal mean field of the ISM.

The seasonal cycle of the cloud layer amounts was examined in the seasonal simulations and compared with MODIS cloud observations. We found that the high-level cloud amount increased by 5-7% in all monsoon months in the wIce runs whereas the middle cloud amount decreased by 3-4% in wIce with respect to woIce. There was an underestimation of 10-15% in the low cloud fraction in both wIce and woIce across all seasons when comparing to MODIS observations.

When the saturation was set to over ice above the freezing level (wIce), a mean seasonal drying of specific humidity (q) occurred in the middle and upper troposphere. The maximum in drying in wIce was coincident with the location of the freezing level and the latitude of the maximum in q at the freezing level, which is over central India and the BoB. At the freezing level in the wIce runs, the saturation is changed to be over ice. This lowers the saturation specific humidity, bringing the air closer to saturation. The model responds by condensing more water out of the column and thereby decreasing q. In the model, when water vapor is condensed, owing

to supersaturation, it falls out of the column in the form of precipitation. We expected then that grid-scale explicit precipitation would increase when SVP over ice was prescribed. We found that this was indeed the case and that this increase in grid-scale precipitation was present across most of the domain but was maximum over central India in the wIce runs. Over the equatorial Indian Ocean, the increase in grid-scale precipitation led to an increase in total mean rainfall. Over India however, the increase in grid-scale precipitation was compensated by a loss of convective precipitation and thus the total precipitation is nearly the same in wIce and woIce. The model responds to the slight decrease in the saturation condition above the freezing level in the wIce simulations by increasing grid-scale condensation of water above the freezing level and in doing so adds to a preexisting moisture sink in the model. Importantly, this added moisture sink, which acts to remove supersaturation, will be located in areas which contain relative humidities near 100%. Areas that are near 100% relative humidity (RH) with respect to water may be supersaturated with respect to ice, which will then result in removal of moisture. This implies that, during the ISM, areas over India that contain high mid-level relative humidities as a result of constant rainfall and convection will be most impacted by the removal of moisture that is triggered by SVP over ice above the freezing level. Indeed, we see in Fig. 6a and 6b that the region in which the most moisture is removed was over India. Mean seasonal mid-level RH in the ISM region was decreased in wIce relative to woIce, while upper-level RH increased in wIce relative to woIce. In mid-levels over most of the model domain this led to less seasonal cloudiness but more upper-level cloud amount relative to woIce. In terms of radiation then, seasonal solar radiation was increased in wIce at the surface due to less mid-level clouds. Terrestrial outgoing longwave radiation (OLR) increased at the top of the atmosphere (TOA) in wIce due to less absorption by the atmosphere and less mid-level cloudiness. The mean seasonal

rainfall difference over India between wIce and woIce is around 10% of the observed interannual variability of seasonal All India rainfall.

In the wIce simulation, middle and upper tropospheric moisture is leaving the column as a result of increased condensation. If mass is leaving the column in the form of condensed water vapor we might speculate that the mean circulations would be slightly altered in wIce compared to woIce. An analysis of the 200 hPa and 850 hPa wind circulations in wIce and woIce during JJAS was conducted (not shown). Little to no change was found between our experiments with respect to the upper-level and lower-level monsoon circulations. This may suggest that vapor which is leaving the column and precipitating out is reentering the column through evaporation at some other time, however we would then expect some moistening at these levels which does not seem to be detected by Fig. 10. This is a point to explore for a future analysis.

A comparison between the seasonal and multiyear experiments showed that, qualitatively the impact of the imposed SVP difference on the mean precipitation and moisture fields is largely the same during the ISM. In the multiyear simulations we found that, consistent with the seasonal runs, the wIce precipitation over India was greater than in woIce. In terms of column moisture, the multiyear simulations corroborated the conclusions made from the seasonal runs by showing that the mean integrated moisture above the freezing level decreases in wIce. The SVP forcing appears to be a function of amount of moisture above the freezing level in the multiyear simulation.

6.2 RSM-ROMS SVP Experiments

The uncoupled simulations revealed significant changes to the Net Heat Flux (NHF), cloud amount, and rainfall forcings as a result of changes to the SVP calculation. However,

without an interactive ocean component it is difficult to understand fully the impact of any changes in the seasonal NHF into the ocean, or for that matter the full extent of the impact from SVP on the ISM climate. Therefore, with a second set of model experiments, the wIce and woIce simulations were repeated with coupling added to ROMS. In addition, a third model experiment was added in which the SVP is linearly interpolated between over liquid water and over ice in the temperature range between 0^{o}C to -20^{o}C (MIX). All three RSM-ROMS simulations were run continuously for 14 years from 1997-2010.

The mean seasonal atmospheric response to SVP changes between wIce-woIce in the uncoupled model seem to be slightly reduced or the same in the coupled simulations. Like the uncoupled simulations, in the wIce simulation grid-scale condensation of water is increased relative to woIce above the freezing level because the saturation condition is easier to meet when it is prescribed to be over ice instead of water. This results in a relative drying of the middle troposphere in the wIce simulation, however we found that the amount of drying is slightly less in the coupled simulation compared to the uncoupled simulation. This leads to similar results with respect to the cloud amount, and radiative fluxes where the spatial patterns of the changes between wIce-woIce are very similar between the uncoupled and coupled simulations but the difference is slightly reduced. Where we had expected the addition of coupling to exaggerate the differences between the wIce and woIce simulations, it seems to have generally done the opposite.

Interestingly, when comparing to woIce, the MIX simulation is not significantly different from the wIce simulation. The same thermodynamic drying above the freezing level occurs in MIX and it is only slightly reduced compared to wIce. The spatial patterns of the changes to the mean seasonal ISM climate are much the same in MIX, and it appears that in these simulations,

it is difficult to distinguish between a model which calculates saturation over ice above the freezing level, and a model which includes a transition region between 0°C and -20°C. This is an important point because as we see in Table 1, several current state-of-the-art CMIP5 models calculate the SVP as we did in MIX. However it should also be noted that we may not expect the same results as we have found here if we used one of the CMIP5 models in Table 1 because the model parameterizations and configuration will be different, but we argue that they should be similar if the same SVP experiment were repeated.

Over the whole AS in the uncoupled wIce simulation the NHF is increasing by 2-3 W/m^2 during the ISM, however in the coupled model it does not have a consistent sign either way. The reason for this seems to be at least partially due to a coastally trapped Kelvin wave along the coast of Arabian Peninsula. This boundary trapped wave causes a large fluctuation in the SST and associated LHF such that it is difficult to see any large-scale change in the NHF. It is possible that there is a positive seasonal change in the NHF, like the uncoupled simulations indicate, but that is hidden by this disturbance over the AS. Because the NHF is nearly unchanged in the AS we found very little change in the seasonal SST or OMT. Over the EEIO, the changes in the NHF are much the same between the coupled and uncoupled simulations and a resulting 2-3 W/m^2 of radiation leaving the ocean leads to a slight but consistent cooling of the seasonal SST by about 0.06 °C. The impact on the ocean from changes to the SVP calculation in the coupled model simulations seemed underwhelming. It is possible that this underwhelming finding is the result of insufficient vertical grid spacing in the upper ocean or a diffusion of heat which is too strong. Alternatively, this lower sensitivity in the coupled simulations could be interpreted as the damping effect of air-sea coupling. In other words, the air-sea coupling dampens the atmospheric and oceanic response to changes in the SVP calculation relative to the

uncoupled simulations. In the coupled model, over the whole domain, the SW flux and LHF are both reduced (in both wIce and woIce) compared to the uncoupled simulations. The reduction in SW radiation is attributed to an increase in overall cloudiness in the coupled simulation, and the decrease in the LHF is a result of LHF being allowed to cool the SST.

6.3 The Importance of Air-Sea Interaction for ISOs

Utilizing both coupled and uncoupled wIce model simulations, the evolution of ISO events was analyzed in the context of air-sea interaction and the WES feedback. For this analysis we constructed composites of the phases of the 30-60 day intraseasonal oscillation leading up to and in the wake of a peak in the intraseasonal rainfall over India. For comparison, we constructed an observed composite of peaks in the ISO from daily TRMM rainfall and OI-SST data.

The observed composite shows a clear relationship between intraseasonal SST and convective anomalies. Enhanced convection begins to propagate northwards from the equatorial latitudes at around 15 days before a peak with warm SST anomalies leading to the north. SST anomalies strengthen upon reaching the BoB and eastern AS and with a lag of about 5 days the rainfall anomalies also strengthen over India to initiate an ISO peak. Cool SST anomalies follow in the wake of enhanced convection. The rainfall and SST anomalies illustrate the presence of strong air-sea interactions during an ISO where, north of the center of convection, SSTs warm as a result of increased NHF there, and SSTs cool under the convection center as a result of increased cloudiness and decreased NHF. Maximum intraseasonal heating and cooling of the SSTs from these observations is on the order of 0.3 ^{o}C.

In the coupled model the relationship between SST and convection in agreement with the observed relationship, whereas in the uncoupled model the SST anomalies only generally lead

the convective anomalies and the cooling in the wake of a peak is very weak. The coupled model ISO events show much more convective organization with strong easterly zonal wind anomalies to the north of convection and westerly anomalies to the south. These zonal wind anomalies are weaker in the uncoupled model. Intraseasonal downward SW flux and LHF anomalies in the coupled model clearly interact with the ocean to form SST anomalies that then help propagate the convective anomalies, while this relationship is only present in the uncoupled model to the extent that the ocean is forcing atmospheric anomalies. In the uncoupled model, intraseasonal SST anomalies are strong during ISO events and there is evidence of northward propagation of the SST anomalies, but the convective anomalies show little evidence of northward propagation and the rainfall anomalies illustrate a stationary wave pattern in the ISO. Lag/lead correlations between SST and rain anomalies during the ISO reveal that the coupled model is in close agreement with the observed SST-Convective relationship, whereas the correlation is much reduced in the uncoupled model. This shows that WES feedback processes have a significant role in modulating and propagating the ISO. However, we cannot conclude that air-sea interaction is solely responsible for the origin or propagation of ISOs as the uncoupled model shows an ability to simulate a robust ISO signal with comparable amplitude to observations without coupling. The capability of the uncoupled model to simulate an ISO peak and then produce the opposite sign in convection, without robust SST anomalies, shows that internal atmospheric dynamics must play some role in the evolution of ISOs.

6.4 Future Work

At the conclusion of this work there are still several important questions which we haven't addressed here or aspects of this work that we believed could be improved in the future. We will detail these here.

First, this study is regionally and temporally focused on the ISM which is one of the largest tropical circulations on earth involving a large amount of convection, rainfall and associated water vapor. As described earlier, the cloud characteristics of the ISM are complex involving numerous cloud types which have important interactions with the radiative fluxes and seasonal rainfall. We would argue that this would make the ISM an ideal first experiment to test whether or what sensitivities and impact exist with respect to SVP. On the other hand a better numerical and quantitative assessment of the global impact of SVP and saturation is lacking as a result of this choice. because of the choice in conducting this experiment in a region with such a unique seasonal climate the results found here with respect to the impact of SVP might be limited in some ways to this region and season. For example, the vast amount of convection that occurs during the ISM also involves enormous amounts of latent heating from condensation. It is possible that some of the impact that we found here in terms of increased condensation are magnified because of the large amount of condensation that is already an integral part of the seasonal mean. Considering these points then we would recommend a future study consider the impact of SVP and saturation through a global model experiment.

One future extension of this current work would be to test the impact of SVP calculations in a version of the RSM with a more complex microphysics which explicitly solves for the amount of hydrometeors within clouds in a grid cell. This in combination with a radiation scheme that explicitly handles the changes to the distribution of the water species in a given cloud would be ideal. In the current setup of the model, the radiative scheme assumes a given

distribution of cloud water and cloud ice and attributes a size distribution based on its classification as high, middle and low clouds. However, a cloud microphysics scheme where all of the water species have separate prognostic equations for the amount of ice or liquid in a cloud would provide for a more complete analysis of the impact of changes to the SVP calculation to the monsoon simulation. It is possible that there are sensitivities or insensitivities that would be exposed by a more detailed calculation of the cloud microphysics. Allowing the explicit calculation of cloud phase hydrometeors would also provide an opportunity to test an SVP parameterization where the relative amount of cloud water to cloud ice calculated in the microphysics is used in the calculation of SVP in regions of mixed phase clouds. These experiments could then be repeated for the coupled simulations using the modified RSM-ROMS model. It may however be noted, that the computational time for such a model with explicit microphysics is considerable and the proposed simulations may have to be significantly shortened.

With our uncoupled simulations we obtained an important result with respect to how the changing of SVP may affect the ISM climate through the NHF into the ocean. We proposed to address this with a coupled simulation where the ocean can respond to any NHF changes on seasonal or interannual timescales. Based on the modification of the mean seasonal NHF by 2-3 W/m^2 in the AS and EEIO of opposite signs we expected there to be a significant ocean heating or cooling during the monsoon season. In the EEIO we found some evidence of cooling of the SST but it is difficult to say whether this is having a significant impact in our simulations. There is no detectible evidence of heating or cooling in the upper ocean in either region on an interannual timescale. If ocean processes played an insignificant role in modulating the heat content in the upper ocean the NHF would be the most important component in determining

upper ocean heating. It is possible that in our simulations there is a large amount of heating which is being dissipated or advected leading to little realized heating or cooling in the upper ocean. To better understand what the relationship the SST has with the NHF on seasonal or interannual timescales a correlation between the change in the NHF over some period (dSST) and the mean NHF over that period could be computed. For a seasonal analysis dSST is the difference between the mean of the last 5 days and the mean of the first 5 days of the month. This type of analysis has been conducted in Yu et al. (2007) to measure the role the NHF plays in regulating the SST in the IO. If we find that the relationship of NHF and dSST is minimal in the AS, we might conclude that ocean dynamics must be playing a larger role here.

We also attempted to get a better understanding of the physical processes which are leading to the changes in the seasonal NHF by comparing between wIce and woIce simulations in both the uncoupled and coupled model experiments. We decomposed the NHF into the two most important components for NHF variability, the solar radiation and LHF, and found that both fluxes seem to be decreased in the coupled model. This raises the question of exactly what processes are modifying the NHF in the coupled model. A study by Du et al. (2008) decomposed the LHF further into the atmospheric response and the oceanic response to help explain why the long-term NHF trend in the IO is near zero but the IO SST is indicating warming over the same period. The study then separates the atmospheric response further into that arising from changes to the wind speed, temperature difference (ΔT) and relative humidity. An analysis such as this may help elucidate what processes are exactly responsible for modifications to the seasonal NHF in the coupled simulations. This may also help explain some of the problems in explaining the relationship between the NHF and SST as explained earlier.

Additionally, regarding Chapter 5, we noticed that in terms of intraseaonal SST anomalies, the uncoupled simulation in fact showed the warmest SST anomalies. It has been pointed out in some similar studies to this one (Woolnough et al. 2007; Wang et al. 2009) that SST variability associated with ISO events was stronger if the vertical resolution in the upper ocean was increased. Thus we recommend that in a future coupled simulation we increase the vertical resolution to see if this improves the simulation of ISO events by increasing the variability in SST. The variability in SST on intraseasonal timescales with respect to ISO events in most coupled models is still weaker than is observed.

APPENDIX A

RSM CALLTREE

Below is a call-tree for the Regional Spectral Model (RSM), made for the purposes of understanding the structure of the major programs within the model. The call-tree is made by using the ftnchek program which, when run on a set of fortran programs will interpret the call commands made within a program to trace the workflow of the model. This is useful for understanding the structure of the RSM. The ftnchek program also creates html links for each subroutine as shown below in the programs which are underlined in blue. Clicking on the link gives information about the input and output variables for the subroutine and what calls are made in the program. Indentations indicate a subroutine call. The call-tree can be accessed at file:///C:/Users/Russel%20Glazer/Desktop/RSM/RSM_calltree/CallTree.html. Repeated calls to a subroutine from different programs include the words "(see above)" to indicate that the link to the subroutine information can be found by finding the first mention of the subroutine.

```
ALBAER
CNVAER
    GLATS
        POLY
CNVALB
    GLATS (see above)
CO2O3
    CO2IN1
    CO2INS
    CO2INT
        COEINT
            PATH
        QUADSR
            SINTR2
                PATH
                QINTRP
        RCTRNS
            COEINT (see above)
            SINTR2 (see above)
```

```
        SINTR2 (see above)
    CO2PTZ
        ANTEMP
        MIXRAT
        OZONE
        SIGP
            NEWSIG
MTN
    TERSUB
        GAUSSLAT
        MAKEMT
        MAKEOA
        NNTPRT
        SPHERT
            EQUALLAT
            FAX
            FFT99M
            FFTRIG
            GAUSSLAT
            LEGENDRE
P2SIG
    CMPIND
    EPSLON
    FFTIDIM
        FAX
        FFT99M
        FFTRIG
    FL22A
    FPVS0
    GLATS (see above)
    GOZRMT
    GPVS
        FPVSX
        FPVSX0
    MSUM2A
    NEWPS2
    NEWPS3
    NEWSIG2
    PLN2T
    PRSGRBRD
        FIXRD2
            GETAREA
            GETGBSS
            NAINIT
            NAOPEN
            NGETGIR
            NRDGB
            NUMCHAR
            RGETAREA
            RMAXMIN
            SUBST
            VDAY
                RMPABORT
                    MPI_ABORT
        LA2GA
            GAULAT
            RMAXMIN
    PSUM2A
    RMSGTO
        HBARTR
    ROW1NS2
    SG2SG
        TRISPL
```

```
        VALTS
    SG2SGRH
        TRISPL
        VALTS
    SYMASA
REGINP
    G2RINP
        CMPIND
        DZUVLE
        EPSILO
        FL2I
        FPLFML
        FTILONF
            FFT99M
        G2RINI
        GFTLONF
            FAX
            FFTRIG
        GGOZRM
            TRANSO
        GLATS (see above)
        GPLN2I
        GTORINI
        PLN2I
        RCHGR
            EXTRAP
                NEWPS
                SG2SG (see above)
            NEWSIG
            RSETSIG
        REGOROG
            CCTOGD
                FFSCOS
                    FFT99M
                SUMFFC
            GDTOCC
                FFACOS
                    FFT99M
                SUMGGC
            MAXMIN
            PLNINI
            RFTINI
                FAX
                FFTRIG
            SHALFI
        RWRITE
            SHALFI
            SHALFO
        SETGRD
        SHALFO
        SPHQK1
            FTILONF (see above)
            GGTOBG
            GGTORG
            PLN2I
            SUMS2I
        SPHQK2
            DELLNP
            FTILONF (see above)
            GGTOBG
            GGTORG
            PLN2I
            SUMS2I
```

```
            SUMTOP
        SUMS2I
        SUMTOP
    S2RINP
        G2RINI
        GG2RG
        GLATS (see above)
        RMAXMIN
        SETGRD
        SFCFLD
        SHALFO
RMTN
    RTERSUB
        DEFG2R
            RMAXMIN
        FFACOS (see above)
        FFSCOS (see above)
        LNCZS
        PLNINI
        RFTINI (see above)
        RMAKEMT
        SETGRD
        SHALFO
        SUMFFC
        SUMGGC
RPGB
    CTLINI
    GPVS (see above)
    GTDP
        FTDPXG
    GTHE
        FTHEX
    GTMA
        FTMAXG
    IDSDEF
    RMPBCASTI
        MPI_BCAST
    RMPBCASTR
        MPI_BCAST
    RMPDIMSET
        RDIMSET
            EQUDIV
        RMPABORT (see above)
    RMPFINE
        MPI_FINALIZE
        MPI_WTIME
        RMPABORT (see above)
    RMPINIT
        MPI_COMM_RANK
        MPI_COMM_SIZE
        MPI_COMM_SPLIT
        MPI_INIT
        MPI_WTIME
        RMPABORT (see above)
    RPGB1
    RRDSGH
        FNAM
        RMPBCASTI (see above)
        RMPBCASTR (see above)
RSMONLY
    BASEFNAM
        VDAY (see above)
    GETCON
```

```
    CMPIND
    EPSILO
    GFTLONF (see above)
    GGOZRM (see above)
    GPLN2I
    GPVS (see above)
    GRDDF
    GRDKT
    GTDP (see above)
    GTHE (see above)
    GTMA (see above)
    RMPBCASTC
        MPI_BCAST
    RMPBCASTI (see above)
    RMPBCASTR (see above)
RMPBCASTI (see above)
RMPBCASTR (see above)
RMPDIMSET (see above)
RMPFINE (see above)
RMPINIT (see above)
RSMINI
    EPSLXY
    FIXIO
        FIXRECIO
            SHALFI
            SHALFO
        NUMCHAR
        SFCFLD
    GETWT
        BSPLINE
            TAY
        GETWL
        ILAGW
    PINT3
    PLNINI
    RAMTM
        RPRNTA
    RFTINI (see above)
    RLTBINI
        NUDGECOEF
        RMPGF2P
            MPI_SCATTERV
            TMPRCV
        RMPSYNALL
            MPI_BARRIER
            RMPABORT (see above)
        SHALFI
    RMAXMIN
    RMPABORT (see above)
    RMPBCASTI (see above)
    RMPBCASTR (see above)
    RMPGF2P (see above)
    RMPSF2P
        MPI_SCATTERV
        TMPRCV
    RMPSYNALL (see above)
    RSETMAP
        RMPBCASTR (see above)
        RMPGP2F
            MPI_GATHERV
            TMPRCV
        RMPSYNALL (see above)
    RSETSFC
```

```
    FFSNCS
        FFT99M
    RMPNL2NY
        MPI_ALLTOALLV
        TMPRCV
    RMPNN2N
        MPI_ALLTOALLV
        TMPRCV
    RMPSYNALL (see above)
    RMPX2NX
    SUMFCS
RSETSIG
RSMINP
    GSM2BGD
        DZUVLE
        FL2I
        FPLFML
        FTILONF (see above)
        PLN2I
        SPHQK1 (see above)
        SUMS2I
        SUMTOP
    RMPBCASTC (see above)
    RMPBCASTI (see above)
    RMPBCASTR (see above)
    SREAD
        GDTOCC (see above)
        GDTOCS
            FFACOS (see above)
            SUMGGS
        GDTOSC
            FFASIN
                FFT99M
            SUMGGC
        GETPTB
            PINT1
        RMPBCASTC (see above)
        RMPBCASTI (see above)
        RMPBCASTR (see above)
        RMPGF2P (see above)
        RMPGP2F (see above)
        RMPSP2F
            MPI_GATHERV
            TMPRCV
        RMPSYNALL (see above)
        SHALFI
SETBGD
SETG2R
    CMPIND
    EPSILO
    FL2I
    FPLFML
    FTILONF (see above)
    G2BINI
    G2RINI
    GFTLONF (see above)
    GGOZRM (see above)
    GLATS (see above)
    GPLN2I
    GTOBINI
    PLN2I
    SPHQK1 (see above)
SETGRD
```

```
    SHALFI
    SHALFO
    ZERFLX
RSMSMF
    DZ2UV
    MPI_BARRIER
    RBMCM
    RDAMPUX
    RDELDIF
    RDFINI
        FIXIO (see above)
    RFILT1
    RFILT2
    RLATBND
    RLOOPA
        DELLCC
        DELLCS
        DELLSC
        FFACOS (see above)
        FFANCS
            FFT99M
        FFSCOS (see above)
        FFSNCS (see above)
        GBPHYS
            CNVCLDN
            DCYC2
            GWDPS
                GWDRAG
            LRGSCL
            MONINP
                TRIDI2
                TRIDIN
            OMEGAS
            RASCNP_1D
                RASV
                    CLOUD
                        ACRITN
                        RNCL
            SETRASV1_1D
            SFCDIAG
                FPVS0
            SFCDIF
                FPVS0
                RMPABORT (see above)
            SFCDRV
                SFC_NOAH
                    FPVS0
                    SFLX
                        ALCALC
                        CANRES
                        CSNOW
                        NOPAC
                            SHFLX
                                HRT
                                    SNKSRC
                                        FRH2O
                                    TBND
                                    TDFCND
                                    TMPAVG
                                HRTICE
                                HSTEP
                                    ROSR12
                            SMFLX
```

```
                        DEVAP
                        SRT
                            WDFCND
                        SSTEP
                            ROSR12
                        TRANSP
                    TDFCND
                PENMAN
                REDPRM
                    RMPABORT (see above)
                SFCDIF (see above)
                SNFRAC
                SNOPAC
                    SHFLX (see above)
                    SMFLX (see above)
                    SNOWPACK
                SNOWZ0
                SNOW_NEW
                TDFCND
        SFC_OCEAN
            FPVS0
        SFC_SEAICE
            SEAICETM
                FPVS0
                KTSOIL
    SHALCV
        MSTADB
            FPKAP
            FTDP
            FTHE
            FTLCL
        TRIDIN
PINT1
PINT3
RFIDI
RMPABORT (see above)
RMPGETSPD
    MPI_ALLREDUCE
    SPDRCV
RMPN2NN
RMPNK2NN
    MPI_ALLTOALLV
    TMPRCV
RMPNK2NX
    MPI_ALLTOALLV
    TMPRCV
RMPNL2NY (see above)
RMPNN2N (see above)
RMPNN2NK
    MPI_ALLTOALLV
    TMPRCV
RMPNX2NK
    MPI_ALLTOALLV
    TMPRCV
RMPNX2X
    MPI_ALLTOALLV
    TMPRCV
RMPNY2NL
    MPI_ALLTOALLV
    TMPRCV
RMPSYNALL (see above)
RMPX2NX
SETRAS
```

```
        RMPABORT (see above)
        SETES
            ESATX
    SUMFCS
    SUMFFC
    SUMGCS
    SUMGGC
RLOOPB
    DELLCC
    FFSCOS (see above)
    FFSNCS (see above)
    GBPHYS (see above)
    PINT1
    PINT3
    RMPNK2NX (see above)
    RMPNL2NY (see above)
    RMPNN2N (see above)
    RMPNN2NK (see above)
    RMPSYNALL (see above)
    RMPX2NX
    SETRAS (see above)
    SUMFCS
    SUMFFC
    UV2DZ
RLOOPR
    DELLCC
    FFSCOS (see above)
    FFSNCS (see above)
    GRADINI
        CRHTAB
        GAEROS
        GCLJMS
        GRLWSW
            CONRAD
                TABLE
            HCONST
            O3INT
            O3INTN
        RINSUR2
            GG2RG
            RMPBCASTR (see above)
    GRADPRE
        ALBAER
        CDATE
        COMPJD
        COSZMN
        FCSTIM
        O3SBUV
        PRTIME
        RINSUR2 (see above)
        SOLAR
    GRPHYS
        GRRAD1
            ALBSNO
            CLDJMSN
            OMEGAS
            OZ2D
            OZON2D
        GRRAD2
            RDLWSW
                CLDPRP
                LWRCHOU
                    IRRAD1
```

```
                        B10EXPS
                        B10KDIS
                        CFCEXPS
                        CFCKDIS
                        CH4EXPS
                        CH4KDIS
                        CO2EXPS
                        CO2KDIS
                        COLUMN
                        COMEXPS
                        COMKDIS
                        CONEXPS
                        H2OEXPS
                        H2OKDIS
                        N2OEXPS
                        N2OKDIS
                        TABLUP
                SWR95
                    FLXCO2
                    SOLIR
                        AEROS
                        SWFLUX
                    SOLUV
                        AEROS
                        SWFLUX
    MPI_BARRIER
    PINT1
    PINT3
    RMPNK2NX (see above)
    RMPNL2NY (see above)
    RMPNN2N (see above)
    RMPNN2NK (see above)
    RMPSYNALL (see above)
    RMPX2NX
    SUMFCS
    SUMFFC
    UV2DZ
RSICDIF
    DZ2UV
    RGETCD
        MATINV
    UV2DZ
RSMLTB
    GSM2BGD (see above)
RSMSAV
    FIXIO (see above)
    FNAM
    SWRITE
        CCTOGD (see above)
        CSTOGD
            FFSCOS (see above)
            SUMFFS
        GETFUL
            PINT1
        MAXMIN
        RMPGP2F (see above)
        SCTOGD
            FFSSIN
                FFT99M
            RMPABORT (see above)
            RMPNK2NX (see above)
            RMPNL2NY (see above)
            RMPNN2N (see above)
```

```
            RMPNN2NK (see above)
            RMPSYNALL (see above)
            RMPX2NX
            SUMFFC
        SHALFO
RUPDATE
SEND_FLX_RECV_SST
    MPI_BARRIER
    MPI_COMM_RANK
    MPI_RECV
    MPI_SSEND
    RMAXMIN
    RMPABORT (see above)
    RMPBCASTI (see above)
    RMPBCASTR (see above)
    RMPGF2P (see above)
    RMPGP2F (see above)
    RMPSYNALL (see above)
    SHALFI
    SHALFO
SFC
    CHECKFN
    INDS2G
    RDGRBSFC
        RDMASK
            NUMCHAR
            RMPABORT (see above)
        RDOROG
            NUMCHAR
            QCMXMN
            RMPABORT (see above)
        SUPEREAD
            FIXRD
                GETGBSS
                NAINIT
                NAOPEN
                NGETGIR
                NRDGB
                NUMCHAR
                RGETAREA
                RMAXMIN
                VDAY (see above)
            FLD2MSK
            LL2MSK
                FIXRD (see above)
                I2O
                    LL2GG
                    LL2XYR
                    XY2LLR
                I2OINI
                    GAULAT
                    LL2XYR
            LL2RSM
                I2O (see above)
                I2OINI (see above)
                NNTPRT
                RMAXMIN
                SETGRD
                SHALFO
            RMPABORT (see above)
    RMPABORT (see above)
    RMPBCASTI (see above)
    RMPBCASTL
```

```
        MPI_BCAST
    RMPBCASTR (see above)
    RMPGF2P (see above)
    RMPSYNALL (see above)
    SFCMRG
        CHECKSNDPH
        LANDTYP
        MRGFLD
        MRGSNOW
        QCMXMN
        QCSICE
        TSFCOR
    SHALFI
    SHALFO
    SUPEREAD (see above)
STDAMP
STDAMP3
    CCTOGD (see above)
    GDTOCC (see above)
    GETFUL (see above)
    MPI_ALLGATHER
SUBPGB
    ADDFLX
        FWINDX
            FPVS
    FNAM
    GETRH
        FPVS0
    GRIBIT
        GTBITS
        PDSENS
        W3FI68
        W3FI72
    HYDRO
    IDSDEF
    ISRCHFLT
    MPGFPK2FK
        MPI_ALLGATHERV
        MPI_GATHERV
    OMEGA
    RCOF2GRD
        CCTOGD (see above)
        CSTOGD (see above)
        DELLCC
        DELLCS
        DELLSC
        GETFUL (see above)
        GETFULDEV
            PINT3
        SCTOGD (see above)
        SSTOGD
            FFSSIN (see above)
            RMPABORT (see above)
            RMPNK2NX (see above)
            RMPNL2NY (see above)
            RMPNN2N (see above)
            RMPNN2NK (see above)
            RMPSYNALL (see above)
            RMPX2NX
            SUMFFS
    RMPABORT (see above)
    RMPBCASTR (see above)
    RMPGP2F (see above)
```

```
            RMPGPFK2FPK
                MPI_ALLTOALLV
                TMPRCV
            RMPSYNALL (see above)
            SHALFO
            SIG2P
                ISRCHFLT
            SIG2PT
            SUNDRY
                LIFTIX
                    FPKAP
                    FTDP
                    FTHE
                    FTLCL
                    FTMA
                SIG2MW
                    SPCOEF
                    SPFMAX
                SIG2TP
            SUNPRM
                ISRCHEQ
            WRYTE
        UV2DZ
        ZERFLX
    RTREAD
        CMPIND
        RMPBCASTC (see above)
        RMPBCASTI (see above)
        RMPBCASTR (see above)
SFC0
    FIXIO (see above)
    SFC (see above)
    SFCFCNV
        NCP1TONOA1
        NCP2TONOA1
        NCP3TONOA1
        OSU1TONOA1
            GETSLC
                FRH2O
        OSU2TONOA1
            GETSLC (see above)
        VIC1TONOA1
        VIC2TONOA1
    SFCFLD
```

APPENDIX B

SVP MODIFCATIONS

Here we will detail the modifications that were made to RSM for the SVP experiments, the location of the changes to model code, and what the original setup of the model was for calculation of the SVP and RH. First, the original setup of the RSM is such that it calculates saturation over liquid water regardless of the temperature. In detail here are the programs which originally contribute to calculating SVP and moisture variables. The program gpvs is a callable function which creates a table of saturation vapor pressure values using the fpvsx and fpvsx0 functions. Programs tbpvs and tbpvs0 are the two arrays forming the table of saturation vapor pressure values (fpvsx and fpvsx0 are used to calculate these). The programs fpvs and fpvs0 are the functions called throughout the original RSM code. They linearly interpolate the tbpvs and tbpvs0 values to speed up calculation of SVP. Programs fpvsx and fpvsx0 are the programs that actually calculate the SVP values which are used for the table. A few important points about fpvsx and fpvsx0 are that in fpvsx there is a statement to identify if the temperature is below 0 degrees. If it is below 0 it will use saturation over ice instead of water. This statement only gets used if the #ICE flag is set to be true. The fpvsx0 program does not have the ice option for below 0 so when fpvs0 is used SVP over ice will never be used in the original model.

One of the goals of making modification to the SVP calculation in RSM was also to simplify this part of the model. We can see that the calculation of SVP originally in RSM is not streamlined and there are multiple programs which contribute to SVP. Considering this we implemented a new set of programs in RSM to calculate SVP which simplifies the code and unifies the method for calculating SVP. This method was originally detailed in Marx (2002) for implementation into the Center for Ocean-Land-Atmosphere Studies (COLA) atmospheric

general circulation model. In this program the calculation of SVP is done using a call to only one single program within RSM. To make this change calls to old subroutines had to be eliminated and the new program implemented in its place. The following programs were modified in this way: cldjmsn, cloud, fwindx, gbphys, getrh, gscond, lrgscl, osutm, seaicetm, sfcdiag, sfcdif, sfc_noah, sfc_ocean. A call to the new program is also required in rsmonly to initiate the creation of the SVP table used later in the model.

REFERENCES

Abhik S, Krishna RPM, Mahakur M, Ganai M, Mukhopadhyay P, Dudhia J (2017) Revised cloud processes to improve the mean and intraseasonal variability of the Indian summer monsoon in climate forecast system: Part 1. J Adv Model Earth Syst 9: 1002-1029.

Abhik S, Halder M, Mukhopadhyay P, Jiang X, Goswami BN (2013) A possible new mechanism for northward propagation of boreal summer intraseasonal oscillations based on TRMM and MERRA reanalysis. Clim Dyn 40: 1611-1624.

Alory G, Wijffels S, Meyers G (2007) Observed temperature trends in the Indian Ocean over 1960– 1999 and associated mechanisms, Geophys. Res. Lett., 34: L02606, doi:10.1029/2006GL028044.

Ashok K, Guan Z, Yamagata T (2001) Impact of the Indian Ocean dipole on the relationship between Indian monsoon rainfall and ENSO. Geophys Res Lett 28: 4499-4502. doi: 10.1029/2001GLO13294

Bony S, Stevens B, Frierson DMW, Jakob C, Kageyama M, Pincus R, Shepherd TG, Sherwood SC, Siebesma AP, Sobel AH, Watanabe M, Webb MJ(2015) Clouds, circulation and climate sensitivity. Nat Geosci 8: 261-268. doi: 10.1038/ngeo2398

Carton JA, Chepurin G, Cao X, Giese B (2000) A simple ocean data assimilation analysis of the global upper ocean 1950-95. Part I: Methodology. J. Phys. Oceanogr., 30:294-309.

Carton JA, Giese B (2008) A reanalsyis of ocean climate using simple ocean data assimilation (SODA). Mon. Wea. Rev., 136:2999-3017.

Chang FL, Li Z (2005) A near -global climatology of single-layer and overlapped clouds and their optical properties retrieved from Terra/MODIS data using a new algorithm. J. Clim 18:4752-4771

Chou M-D (1992) A solar radiation model for use in climate studies. J Atmos Sci 49: 762-772

Chou M-D, Suarez MJ (1994) An efficient thermal infrared radiation parameterization for use in general circulation model. Technical report series on global modeling and data assimilation, NASA/TM-1994-104606, 3, 85 pp

da Silva AM, Young CC, Levitus S (1994) Anomalies of Directly Observed Quantities. Vol. 2, Atlas of Surface Marine Data 1994, NOAA Atlas NESDIS 7: 416 pp.

de Boyer CM, Vialard J, Shenoi SSC, Shankar D, Durand F, Ethe C, Madec G (2007) Simulated seasonal and interannual variability of them ix layer heat budget in the Northern Indian Ocean. J. Clim. 20: 3249-3268.

Dessler AE (2010) A determination of the cloud feedback from climate variations over the past decade. Science 330, 6020: 1523-1527. doi: 10.1126/science.1192546

Donner LJ, Wyman BL, Hemler RS, Horowitz LW, Ming Y, Zhao M, Golaz J, Ginoux P, Lin S, Schwarzkopf MD, Austin J, Alaka G, Cooke WF, Delworth TL, Freidenreich SM, Gordon CT, Griffies SM, Held IM, Hurlin WJ, Klein SA, Knutson TR, Langenhorst AR, Lee H, Lin Y, Magi BI, Malyshev SL, Milly PC, Naik V, Nath MJ, Pincus R, Ploshay JJ, Ramaswamy V, Seman CJ, Shevliakova E, Sirutis JJ, Stern WF, Stouffer RJ, Wilson RJ, Winton M, Wittenberg AT, Zeng F (2011) The Dynamical Core, Physical Parameterizations, and Basic Simulation Characteristics of the Atmospheric Component AM3 of the GFDL Global Coupled Model CM3. J. Climate, 24: 3484–3519, https://doi.org/10.1175/2011JCLI3955.1

Du Y, Xie S-P (2008) Role of atmospheric adjustments in the tropical Indian Ocean warming during the 20th century in climate models, Geophys. Res. Lett., 35: L08712, doi:10.1029/2008GL033631.

Fowler LD, Randall DA, Rutledge SA (1996) Liquid and ice cloud microphysics in the CSU general circulation model. Part I: model description and simulated microphysical processes. J Clim 9:489-529

Fu X, Wang B, Li T, McCreary JP (2003) Coupling between northward-propagating, intraseasonal oscillations and sea surface temperature in the Indian Ocean. J. Atmos. Sci., 60: 1733–1753.

Fu X, Wang B (2004) The boreal-summer intraseasonal oscillations simulated in a hybrid coupled atmosphere–ocean model. Mon. Wea. Rev., 132: 2628–2649.

Garternicht U, Schott F (1997) Heat fluxes of the Indian Ocean from a global eddy-resolving model. J. Geophys. Res., 102: 21 147–21 159.

Gettelman A, Collins WD, Fetzer EJ, Eldering A, Irion FW, Duffy PB, Bala G (2006) Climatology of upper-tropospheric relative humidity from the atmospheric infrared sounder and implication for climate. J Clim 19: 6104-6120.

Girishkumar MS, Joseph J, Thangaprakash VP, Pottapinjara, V, McPhaden, MJ (2017). Mixed layer temperature budget for the northward propagating Summer Monsoon Intraseasonal Oscillation (MISO) in the Central Bay of Bengal. Journal of Geophysical Research: Oceans 122: 8841–8854. https://doi.org/10.1002/2017JC013073

Giorgetta MA, Jungclaus J, Reick CH, Legutke S, Bader J, Böttinger, Brovkin V, Crueger T, Esch M, Fieg K, Glushak K, Gayler V, Haak H, Hollweg H-D, Ilyina T, Kinne S, Kornblueh L, Matei D, Mauritsen T, Mikolajewicz U, Mueller W, Notz D, Pithan F, Raddatz T, Rast S, Redler R, Roeckner E, Schmidt H, Schnur R, Segschneider J, Six KD, Stockhause M, Timmreck C, Wegner J, Widmann H, Wieners K-H, Claussen M, Marotzke J, Stevens B (2013) Climate and carbon cycle changes from 1850 to 2100 in MPI-ESM simulations for the Coupled Model Intercomparison Project phase 5, J. Adv. Model. Earth Syst., 5: 572–597, doi:10.1002/jame.20038.

Godfrey JS, and Coauthors (1995) The role of the Indian Ocean in the global climate system: Recommendations regarding the global ocean observing system. Ocean Observing System Development Panel Rep. 6. Texas A&M University, College Station, TX, 89 pp.

Godfrey JS, Hu R-J, Schiller A, Fiedler R (2007) Explorations of the annual mean heat budget of the tropical Indian Ocean. Part I: Studies with an idealized model, J. Clim. 20: 3210–3228.

Goswami BB, Krishna RPM, Mukhopadhyay P, Khairoutdinov M, Goswarmi BN (2015) Simulation of the Indian summer monsoon in the superparameterized climate forecast system version 2: Preliminary results. J Clim 28: 8988-9012.

Goswami BN (1998) Interannual variation of Indian summer monsoon in a GCM: external condition versus internal feedbacks. J Clim 11:501-522

Goswami BN, Ajaa Mohan RS (2001) Intra-seasonal oscillations and inter-annual variability of the Indian summer monsoon. J Clim 14:1180-1198

Goswarmi BN, Wu G, Yasunari T (2006) Annual cycle, intraseasonal oscillations and roadblock to seasonal predictability of the Asian summer monsoon. J Clim 19:5078-5099

Guillemin EA (1957) Synthesis of Passive Networks. Wiley, 671 pp (see pp. 599-607).

Hahn DG, J Shukla (1976) An apparent relationship between Eurasian snow cover and Indian monsoon rainfall. J Atmos Sci 33: 2461-2462

Haidvogel DB, Arango HG, Hedstrom K, Beckmann A, Malanotte-Rizzoli P, Shchepetkin AF (2000) Model evaluation experiments in the North Atlantic Basin: simulations in nonlinear terrain-following coordinates. Dyn Atmos Oceans 32:239-281

Halkides DJ, Waliser DE, Lee T, Menemenlis D, Guan B (2015) Quantifying the processes controlling intraseasonal mixed-layer temperature variability in the tropical Indian Ocean, J. Geophys. Res. Oceans 120: 692–715, doi:10.1002/2014JC010139.

Han W, Liu WT, Lin J (2006) Impact of atmospheric submonthly oscillations on sea surface temperature of the tropical Indian Ocean, Geophys. Res. Lett., 33, L03609, doi:10.1029/2005GL025082.

Hazra A, Chaudhari HS, Saha SK, Pokhrel S (2017) Effect of cloud microphysics on Indian summer monsoon precipitating clouds: A coupled climate modeling study.

Huffman et al, 2007: The TRMM Multisatellite Precipitation Analysis (TMPA): Quasi-Global, Multiyear, Combined-Sensor Precipitation Estimates at Fine Scales. J. Hydrometeor., 8, 38–55.

Huffman GJ, Bolvin DT, Adler RF (2012) GPCP version 1.2 1-degree daily (1DD) precipitation data set. World Data Center A, National climatic Data Center, Asheville, NC.

Juang H-M H, Kanamitsu M (1994) The NMC nested regional spectral model. Mon Wea Rev 122.1: 3-26

Jiang, X, Li T, Wang B (2004) Structure and mechanisms of the northward propagating boreal summer intraseasonal oscillation. J. Clim., 17, 1022–1039.

Jiang X, Waliser DE, Li JL, Woods C (2011) Vertical cloud structures of the boreal summer intraseasonal variability based on CloudSat observations and ERA-interim reanalysis. Clim Dyn 36: 2219-2232. doi: 10.1007/s00382-010-0853-8

Josey JA, Kent EC, Taylor PK (1999) New insights into the ocean heat budget closure problem from analysis of the SOC air–sea flux climatology. J. Climate, 12: 2856–2880.

Kanamaru H, Kanamitsu M (2007) Scale-selective bias correction in a downscaling of global reanalysis using a regional model. Mon Wea Rev 135: 334-350

Kanamitsu M, Ebisuzaki W, Woollen J, Yang S-K, Hnilo JJ, Fiorino M, Potter GL(2002) NCEP-DOE AMIP-II reanalysis. Bull Am Meteorol Soc 83: 1631-1643

Kanamitsu M, Yoshimura K, Yhang Y, Hong S (2010) Errors of interannual variability and multi-decadal trend in dynamical regional climate downscaling and its corrections. J Geophys Res 115:D17115

Kemball-Cook, S, and Wang B (2001) Equatorial waves and air-sea interaction in the boreal summer intraseasonal oscillation. Journal of Climate, 14, 2923-2942.

Kim H-M, Hoyos CD, Webster PJ, Kang I-S (2008) Sensitivity of MJO simulation and predictability to sea surface temperature variability. J. Climate, 21: 5304–5317.

Klingaman NP, Inness PM, Weller H, Sling JM (2008) The importance of high-frequency sea surface temperature variability to the intraseasonal oscillation of Indian monsoon rainfall. J. Climate, 21: 6119–6140.

Knutson TR, et al. (2006) Assessment of twentieth-century regional surface temperature trends using the GFDL CM2 coupled models, J. Clim., 19: 1624– 1651.

Korolev A, Isaac GA (2006) Relative Humidity in Liquid, Mixed-Phase, and Ice Clouds. J Atmos Sci 63: 2865–2880. doi: 10.1175/JAS3784.1

Korolev A, Mazin IP (2003) Supersaturation of water vapor in clouds. J Atmos Sci 60: 2957-2974.

Krishnamurti, TN and Subrahmanyam, D (1982) The 30-50-day mode at 850 mb during MONEX. J. Atmos Sci 39, 2088-2095.

Krishnamurthy V, Shukla J (2000) Intraseaonal and interannual variability of rainfall over India. J Clim 13: 4366-4377

Krishnamurthy V, Shukla J (2007) Intraseasonal and seasonally persisting patterns of Indian monsoon rainfall. J Clim 20: 3-20. doi: 10.1175/JCLI3981.1

Kumar S, Hazra A, Goswami BN (2014) Role of interaction between dynamics, thermodynamics and cloud microphysics on the summer monsoon precipitating cloud over the Myanmar Coast and the Western Ghats. Clim Dyn 43: 911-924. doi: 10.1007/s00382-013-1909-3

Lawrence, DM and Webster, PJ (2002) The boreal summer intraseasonal oscillation: Relationship between northward and eastward movement of convection. J. Atmos Sci, 59, 1593-1606.

Li H, Kanamitsu M, Hong S-Y, Yoshimura K, Cayan DR, Misra V (2013a) A high-resolution ocean-atmosphere coupled downscaling of a present climate over California. Clim Dyn doi: 10.1007/s00382-013-1670-7

Li H, Kanamitsu M, Hong S-Y, Yoshimura K, Cayan DR, Misra V, Sun L (2013b) Projected climate change scenario over California by a regional ocean-atmosphere coupled model system. Clim Change. doi: 10.1007/s10584-013-1025-8

Li H, Misra V (2014) Thirty-two-year ocean-atmosphere coupled downscaling of global reanalysis over the Intra-American Seas. Clim Dyn 43:2471-2489. doi: 10.1007/s00382-014-2069-9

Li Y, Han W, Wang W, Ravichandran M, Lee T, Shinoda T (2017) Bay of Bengal salinity stratification and Indian summer monsoon intraseasonal oscillation: 2. Impact on SST and convection, J. Geophys. Res. Oceans, 122: 4312–4328, doi:10.1002/2017JC012692.

Liebmann B, Smith CA (1996) Description of a complete (interpolated) outgoing longwave radiation dataset. Bull Am Metorol Soc 77: 1275-1277\

Lohmann U, Roeckner E (1996) Design and performance of a new cloud microphysics scheme developed for the ECHAM general circulation model. Clim Dyn 12:557-572.

Marx L (2002) New calculation of saturation specific humidity and saturation vapor pressure in the COLA atmospheric general circulation model. COLA Tech. Rep. 130: 1-23. [Available from the Center for Ocean–Land–Atmosphere Studies, 4041 Powder Mill Rd., Suite 302, Calverton, MD 20705.].

Matus AV, L'Ecuyer TS (2017) The role of cloud phase in Earth's radiation budget. J Geophys Res Atmos 122:2559-2578

Meehl, GA, Washington WM, Arblaster JM, Hu A, Teng H, Tebaldi C, Sanderson BN, Lamarque J, Conley A, Strand WG, White JB (2012) Climate System Response to External Forcings and Climate Change Projections in CCSM4. J. Climate, 25: 3661–3683, https://doi.org/10.1175/JCLI-D-11-00240.1

Misra, V, Mishra A, Bhardwaj A (2018) Simulation of the Intraseasonal Variations of the Indian Summer Monsoon in a Regional Coupled Ocean-Atmosphere Model. J. Climate, 0, https://doi.org/10.1175/JCLI-D-17-0434.1

Moorthi S, Suarez MJ (1992) Relaxed Arakawa-Schubert. A parameterization of moist convection for general circulation models. Mon Wea Rev 120: 978-1002

Moorthi S, Pan HL, Caplan P (2001) Changes to the 2001 NCEP operational MRF/AVN global analysis/forecast system. NWS Technical Procedures Bulletin 484: 14.

Murphy DM, Koop T (2005) Review of the vapor pressures of ice and supercooled water for atmospheric applications. Q J R Meteorol Soc 131: 1539-1565. doi: 10.1256/qj.04.94

Murtugudde R, Busalacchi AJ (1999) Interannual variability of the dynamics and thermodynamics, and mixed layer processes in the Indian Ocean, J. Clim. 12: 2300–2326.

Murray BJ, O'Sullivan D, Atkinson JD, Webb ME (2012) Ice nucleation by particles immersed in supercooled cloud droplets. Chem Soc Rev 41:6519-6554

Oberhuber JM (1988) An atlas based on the COADS data set: The budget of heat, buoyancy and turbulent kinetic energy at the surface of the Global Ocean. MPI Rep. 15: 198 pp.

Raj Parampil S, Bharathraj GN, Harrison M, Sengupta D (2016) Observed subseasonal variability of heat flux and the SST response of the tropical Indian Ocean, J. Geophys. Res. Oceans, 121, 7290–7307, doi:10.1002/2016JC011948.

Parthasarathy B, Munot AA, Kothawale DR (1994) All India monthly and seasonal rainfall series: 1871-1993. Theor Appl Climtol 49: 217-224

Pierce DW, Barnett TP, Achuta Rao KM, Glecker PJ, Gregory JM, Washington WM (2006) Anthropogenic warming of the oceans: Observations and model results, J. Clim., 19: 1873–1900.

Platnick S, King MD, Ackerman SA, Menzel WP, Baum BA, Riedi JC, Frey RA (2003) The MODIS cloud products: Algorithms and examples from Terra. IEEE Trans Geosci Remote Sens 41:459-473

Platnick S et al. (2015) MODIS atmosphere L3 daily product. NASA MODIS Adaptive Processing System, Goddard Space Flight Center, USA: dx.doi.org/10.5067/MODIS/MOD08_D3.006

Premkumar, K, Ravichandran M, Kalsi SR, Sengupta D, Gadgil S (2000) First results from a new observational system over the Indian seas. Curr. Sci., 78, 323-330.

Pruppacher HR, Klett JD (1978) Microphysics of clouds and precipitation. 1980 (Reidel, Dordrecht, Netherlands, 1978).

Rajeevan M, Rohini P, Kumar KN, Srinivasan J, Unnikrishnan CK (2013) A study of vertical cloud structure of the Indian summer monsoon using CloudSat data. Clim Dyn 40: 637-650. doi: 10.1007/s00382-012-1374-4

Rajendran K, Kitoh A (2006) Modulation of tropical intraseasonal oscillations by atmosphere–ocean coupling. J. Climate 19: 366–391.

Rahman SH, Sengupta D, Ravichandran M (2009) Variability of Indian summer monsoon rainfall in daily data from gauge and satellite. J Geophys Res 114: D17113

Ramanathan V (1987) The role of earth radiation budget studies in climate and general circulation research. J Geophys Res 92: 4075-4095. doi: 10.1029/JD092iD04p04075

Ramanathan V, Cess RD, Harrison EF, Minnis P, Barkstrom BR, Ahmad E, Hartmann D (1989) Cloud-radiative forcing and climate: results from the earth radiation budget experiment. Science, 243, 4887: 57-63. doi: 10.1126/science.243.4887.57

Ramu DA, Sabeerali CT, Chattopadhyay R, Rao DN, George G, Dhakate AR, Salunke K, Srivastava A, Rao SA (2016) Indian summer monsoon rainfall simulation and prediction skill in the CFSv2 coupled model: Impact of atmospheric horizontal resolution. J Geophys Res 121: 2205-2221.

Rasmusson EM, Carpenter TH (1983) The relationship between the eastern Pacific seas surface temperature and rainfall over India and Sri Lanka, Mon Wea Rev 111: 354-384

Randall DA et al. (2007) Climate change 2007: the physical science basis. In: Solomon S et al. (ed) Contributions of working group I to the fourth assessment report of the intergovernmental panel on climate change. Cambridge Univ. Press, Cambridge, 2007.

Reynolds RW, Smith TM, Liu C, Chelton DB, Casey KS, Schlax MG (2007) Daily high-resolution blended analyses for sea surface temperature. J Clim 20:5473-5496

Romatschke U, Houze RA, Jr (2011) Characteristics of precipitating convective system in the South Asian Monsoon. J. Hydrometeor. 12: 3-26.

Rossow WB, Schiffer RA (1991) ISCCP cloud data products. Bull Amer Meteor Soc 72:2-20

Rossow WB, Schiffer RA (1999) Advances in understanding clouds from ISCCP. Bull Amer Meteor Soc 80:2261-2287

Rotstayn LD, Ryan BF, Katzfey JJ (2000) A scheme for the calculation of the liquid fraction of mixed-phase stratiform clouds in large scale models. Mon Wea Rev 128: 1070-1088. doi: 10.1175/1520-0493(2000)128<1070:ASFCOT>2.0.CO;2

Rodwell MJ, (1997) Breaks in the Asian monsoon: The influence of Southern Hemisphere weather systems. J. Atmos. Sci. 54: 2597–2611.

Rui H, Wang B (1990) Development characteristics and dynamic structure of tropical intraseasonal convection anomalies, J. Atmos. Sci. 47: 357–379.

Sabeerali CT, Rao SA, Dhakate AR, Salunke K, Goswami BN (2014) Why ensemble mean projection of south Asian monsoon rainfall by CMIP5 models is not reliable? Clim Dyn 45: 161-174. doi: 10.1007/s00382-014-2269-3

Saha S, Moorthi S, Wu X, Wang J, Nadiga S, Tripp P , Behringer D, Hou Y, Chuang H, Iredell M, Ek M, Meng J, Yang R, Mendez MP , van den Dool H, Zhang Q, Wang W, Chen M, Becker E. (2014) The NCEP Climate Forecast System Version 2. J. Climate, 27: 2185–2208, https://doi.org/10.1175/JCLI-D-12-00823.1

Saji NH, Goswami BN, Vinayachandran PN, Yamagata T (1999) A dipole mode in the tropical Indian Ocean. Nature 401: 360-363

Schiller A, Godfrey JS (2003) Indian Ocean intraseasonal variability in an ocean general circulation model, J. Clim. 16: 21–39.

Schmidt GA, Kelley M, Nazarenko L, Ruedy R, Russell GL, Aleinov I, Bauer M, Bauer SE, Bhat MK, Bleck R, Canuto V, Chen Y-H, Cheng Y, Clune TL, Del Genio A, de Fainchtein R, Faluvegi G, Hansen JE, Healy RJ, Kiang NY, Koch D, Lacis AA, LeGrande AN, Lerner J, Lo KK, Matthews EE, Menon S, Miller RL, Oinas V, Oloso AO, Perlwitz JP, Puma MJ, Putman WM, Rind D, Romanou A, Sato M, Shindell DT, Sun S, Syed RA, Tausnev N, Tsigaridis K, Unger N, Voulgarakis A, Yao M-S, Zhang J (2014) Configuration and assessment of the GISS ModelE2 contributions to the CMIP5 archive. J. Adv. Model. Earth Syst., 6, no. 1: 141-184, doi:10.1002/2013MS000265.

Schott FA, Xie S-P, McCreary JP (2009) Indian Ocean circulation and climate variability. Rev Geophys 47: RG1002, doi:10.1029/2007RG000245.

Seo K-H, Schemm J-KE, Wang W, Kumar A (2007) The boreal summer intraseasonal oscillation simulated in the NCEP Climate Forecast System: The effect of sea surface temperature. Mon. Wea. Rev. 135: 1807–1827.

Sengupta, D, Ravichandran M (2001) Oscillations of the Bay of Bengal sea surface temperature during the 1998 summer monsoon. Geophys. Res. Lett. 28: 2033–2036.

Sengupta, D, Senan R, Goswami BN (2001) Origin of intraseasonal variability of circulation in the tropical central Indian Ocean. Geophys. Res. Lett. 28: 1267–1270.

Shimpo A, Kanamitsu M, Iacobellis S, Hong S-Y (2008) Comparison of four cloud schemes in simulating the seasonal mean field forced by the observed sea surface temperature. Mon Wea Rev 136: 2557-2575

Slingo JM (1980) A cloud parameterization scheme derived from GATE data for use with a numerical model. Q J R Meteorol Soc 106: 747-770.

Slingo JM (1987) The development and verification of a cloud predicition scheme for the ECMWF model. Q J R Meteorol Soc 113: 899-927

Slingo A, Slingo JM (1991) Response of the National Center for Atmospheric Research Community Climate Model to improvements in the representation of clouds. J Geophy Res 96:341-357

Sperber KR, Annamalai H, Kang IS, Kitoh A, Moise A, Turner A, Wang B, Zhou T (2012) The Asian summer monsoon: an intercomparison of CMIP5 vs. CMIP3 simulations of the late 20th century. Clim Dyn 41:2711-2744. doi: 10.1007/s00382-012-1607-6

Srinivasan J, Gadgil S, Webster PJ (1993) Meridional propagation of large-scale monsoon convective zones. Meteor. Atmos. Phys., 52: 15–35.

Stefanova L, Misra V, Chan S, Griffin M, O'Brien JJ, Smith III TJ (2012) A proxy for high-resolution regional analysis for the Southeast United States: assessment of precipitation variability in dynamically downscaled reanalyses. Clim Dyn 38: 2449-2466. doi: 10.1007/s00382-011-1230-y

Stephens GL (2005) Cloud feebacks in the climate system: a critical review. J Clim 18: 237-273. doi: 10.1175/JCLI-3243.1

Su H, Jiang JH, Teixeira J, Gettelman A, Huang X, Stephens G, Vane D, Perun VS (2011) Comparison of regime-sorted tropical cloud profiles observed by CloudSat with GEOS5 analyses and two general circulation model simulations. J Geophy Res 116:D09104. doi:10.1029/2010JD014971

Tan I, Storelvmo T, Zelinka MD (2016) Observational constraints on mixed-phase clouds imply higher climate sensivity. Science 353: 224-227.

Tremblay A, Glazer A (2000) An improved modeling scheme for freezing precipitation forecasts. Mon Wea Rev 128: 1289-1308. doi: 10.1175/1520-0493(2000)128<1289:AIMSFF>2.0.CO;2

Vecchi, GA, Harrison DE (2002) Monsoon breaks and subseasonal sea surface temperature variability in the Bay of Bengal. J. Climate 15: 1485–1493.

Waliser DE, Stern W, Schubert S, Lau KM (2003) Dynamic predictability of intraseasonal variability associated with the Asian summer monsoon. Quart. J. Roy. Meteor. Soc. 129: 2897–2925.

Waliser DE, Jin K, Kang IS, Stern WF, Schubert SD, Wu MLC, Lau KM, Lee MI, Krishnamurthy V, Kitoh A, Meehl GA, Galin VY, Satyan V, Mandke SK, Wu G, Liu Y, Park CK (2003) AGCM simulation of intraseasonal variability associated with the Asian summer monsoon. Clim Dyn doi: 10.1007/s00382-003-0337-1

Waliser DE, Li JLF, Woods CP, Austin RT, Bacmeister J, Chern J, Del Genio A, Jiang JH, Kuang Z, Meng H, Minnis P, Platnick S, Rossow WB, Stephens GL, Sun-Mack S, Tao WK, Tompkins AM, Vane DG, Walker C, Wu D (2009) Cloud ice: A climate model challenge with signs and expectations of progress, J Geophys Res, 114, D00A21, doi: 10.1029/2008JD010015

Waliser DE, Li J-L F L'Ecuyer TS, Chen WT (2011) The impact of precipitating ice and snow on the ration balance of global climate models, Geopys Res Lett, 38, L06802, doi:10.1029/2010GL046478

Wang B, Xie X (1997) A model for the boreal summer instraseasonal oscillation. J Atmos Sci 54,72-86.

Wang W, Chen M, Kumar A (2009) Impacts of ocean surface on the northwar propagation of the Boreal Summer Intrasesaonal Oscillation in the NCEP Climate Forecast System. J. Clim. 22: 6561-6576.

Wang T, Wong S, Fetzer EJ (2015) Cloud regime evolution in the Indian monsoon intraseasonal oscillation: Connection to large-scale dynamical conditions and the atmospheric water budget. Geophys Res Lett 42: 9465-9472. doi: 10.1002/2015GL066353

Weare BC (2004) A comparison of AMIP II model cloud layer properties with ISCCP D2 estimates. Clim Dyn 22: 281-292

Webster PJ (1983) Mechanisms of low-frequency variability: Surface hydrological effects. J. Atmos. Sci., 40, 2110–2124.

Webster PJ, Magaña VO, Palmer TN, Shukla J, Tomas RA, Yanai M, Yasunari T (1998) Monsoons: processes, predictability, and the prospects for prediction. J Geophys Res 103: 14451-14510

WMO (2015b) Recommended algorithms for the computation of marine metrological variables, I.6. JCOMM Technical Report No. 63. World Meteorological Organization, Geneva, Switzerland.

WMO (2015a) Measurement of upper-air pressure, temperature and humidity (J. Nash). Instruments and Observing Methods Report No. 121. Geneva.

WMO (1988) General meteorological standards and recommended practices, appendix A. Technical Regulations, WMO-No. 49. World Meteorological Organization, Geneva, Switzerland.

Woolnough SJ, Vitart F, Balmaseda MA (2007) The role of the ocean in the Madden–Julian oscillation: Implications for MJO prediction. Quart. J. Roy. Meteor. Soc., 133, 117–128.

Wood R, Field PR (2000) Relationships between total water, condensed water, and cloud fraction in stratiform clouds examined using aircraft data. J Atmos Sci 57: 1888-1905.

Xu K-M, Randall DA (1996) A semi-empirical cloudiness parameterization for use in climate models. J Atmos Sci 53: 3084-3102.

Yau MK, Rogers RR (1989) A short course in cloud physics. In: Yau MK, Rogers RR (ed) Formation of cloud droplets, Ch. 6. Elsevier, 1996

Yasunari, T. (1979) cloudiness fluction associated with the northern Hemisphere summer monsoon. J. Meteor. Soc. Japan, 57, 227-242.

---------- (1980) A quasi-stationary appearance of 30- to 40-day period in the cloudiness fluctuations during the summer monsoon over India. J. Meteor. Soc. Japan, 58, 225-229.

Yu L, Jin X, Weller RA (2007) Annual, seasonal, and interannual variability of air-sea heat fluxes in the Indian Ocean, J. Clim., 20: 3190–3209.

Yu L, Weller RA (2007) Objectively Analyzed Air–Sea Heat Fluxes for the global ice-free oceans (1981–2005). Bull. Amer. Meteor. Soc., 88, 527–539.

BIOGRAPHICAL SKETCH

I was born April 13, 1989, in Concord, New Hampshire. My family moved to McLean, Virginia outside of Washington, D.C. when I was two years old and have lived there ever since. I have an older brother who lives and works now in Alexandria, Virginia, also outside of Washington. Living just outside of the DC Beltway I grew up in an area very typically suburban, although over the last few decades the area has become increasingly urbanized as the city expands outward. My interest in meteorology came at a young age, around 7 or 8 year old. I remember being very captivated by tornadoes, although I had never actually seen one, through science programs about weather on the discovery channel and TLC (back when these channels actually had educational programming). But it wasn't until college and being confronted with the choice of picking a major that I decided to commit to meteorology not just as a hobby. I attended Virginia Tech, which at that time had no Meteorology program, for my undergraduate and majored in Geography. In the summer of 2010 at Virginia Tech I took part in a two week summer course that involved storm chasing and severe storms forecasting in the Great Plains. I credit this experience as beginning the thought of pursuing a graduate degree in Meteorology, which eventually lead me to Florida State.

I have lived in Tallahassee for the past seven years and over these seven years I have learned a great deal more than I ever expected. I have grown to really appreciate and love this city and its people as it has given me so much in the way of knowledge, experiences and friendships. I then feel some sadness as my graduate education comes to a close and with it this chapter of my life. But there is also a great amount of excitement as I have in a way fulfilled one of my wishes that I expressed almost 4 years ago when I completed my master's. This summer 2018 I will be moving to Trieste, Italy to begin a postdoctoral position at the Abdul Salam

International Center for Theoretical Physics. This international center is a well renowned institution for international collaboration and research in developing countries.

In the future, however, I would like to visit Tallahassee often and perhaps see old friends. I have grown to love the country around Tallahassee and would hold out some desire to return here to live someday. As my post-graduate career begins my hope is to stay in some capacity near academia where I can keep abreast of new developments in the scientific community. I also have a desire to work in the public sphere at some point as my grandfather did at NASA for many years.